Constructing Pseudocapacitive Electrodes for Supercapacitors based on Rationally Designed Nanoarchitectured Current Collectors

Dissertation

zur Erlangung des Doktorgrades

Dr. rer. nat.

vorgelegt der
Fakultät für Mathematik und Naturwissenschaften der
Technischen Universität Ilmenau

von
M. Sc. Long Liu
Ilmenau

TECHNISCHE UNIVERSITÄT
ILMENAU

Doktorvater und 1. Gutachter: Prof. Dr. Yong Lei
2. Gutachter: Prof. Dr. Heiko O. Jacobs
3. Gutachter: Prof. Dr. Dongjiang Yang

Tag der Einreichung: 17.06.2020

Tag der wissenschaftlichen Aussprache: 30.09.2020

urn:nbn:de:gbv:ilm1-2020000427

Abstract

Supercapacitors are of high importance as electrochemical energy storage devices attributing to their outstanding power performance, excellent reversibility and long cycle life. However, compared with batteries, supercapacitors suffer from low energy density, which hinders their wide application. Pseudocapacitive materials with a high theoretical capacitance hold a great promise in boosting the energy storage capability for supercapacitors. Research on nanoarchitectured current collectors aims to reach their full potential in the field of charge storage by addressing challenging problems such as the inherently low electrical conductivity and the sluggish charge and discharge behavior of most pseudo-capacitive materials. In this regard, three kinds of nanoarchitectured current collectors, *i.e.*, Ni nanorod arrays (NN), etched porous alumina membrane (EPAM) coated with SnO_2 layer (EPAM@SnO_2), and Ni nanowires confined into EPAM (NiNWs-EPAM), were designed to construct pseudocapacitive electrodes and they were investigated in different aspects:

Firstly, the role of NN nanoarchitectured current collectors in supercapacitor electrodes with the pseudocapacitive materials in the case of high mass loading and thick layer is firstly evaluated. Through electrochemical performance and impedance analysis of the electrodes with and without the NN nanoarchitectured current collectors, the validation of thick-layer electrodes design based on nanoarchitectured current collectors is demonstrated.

Secondly, EPAM@SnO_2 scaffolds are designed and employed as nanoarchitectured current collectors for nanoelectrodes in order to improve the device energy density of the micro-supercapacitor (MSC). Owing to the oriented and robust nanochannels in EPAM@SnO_2, the resultant nanoelectrodes can synergize both effective ion migration and abundant electroactive surface area within the limited footprint. A MSC is finally constructed and exhibits record high performance, suggesting the feasibility of the current design for energy storage devices.

Thirdly, the NiNWs-EPAM nanoarchitectured current collector is fabricated to construct non-aggregative and robust one-dimensional (1D) nanoelectrode arrays. The EPAM prevents 1D nanoelectrode arrays from self-aggregating and meanwhile endows them with high structural integrity and electrochemical stability during device assembly and operation process. MSCs assembled with these non-aggregative and robust 1D nanoelectrodes attain remarkable energy storage performance.

The achieved results within this work on nanoarchitectured current collectors for supercapacitors shed light on the design of future energy storage and conversion devices.

Zusammenfassung

Superkondensatoren sind als elektrochemische Energiespeicher von großer Bedeutung, was auf ihre hervorragende elektrische Leistung, ihre ausgezeichnete Reversibilität und ihre lange Lebensdauer zurückzuführen ist. Im Vergleich zu Batterien haben Superkondensatoren jedoch eine geringe Energiedichte, was ihre breite Anwendung einschränkt. Pseudokapazitive Materialien mit einer hohen theoretischen Kapazität sind sehr vielversprechend, um die Energiespeicherfähigkeit von Superkondensatoren zu erhöhen. Die Forschung an nanoarchitektonischen Stromspeichern zielt darauf ab, ihr volles Potenzial im Bereich der Ladungsspeicherung auszuschöpfen, indem man sich mit den herausfordernden Aspekten wie der inhärent niedrigen elektrischen Leitfähigkeit und dem trägen Lade- und Entladeverhalten der meisten pseudokapazitiven Materialien befasst. In diesem Zusammenhang wurden drei Arten von nanoarchitektonischen Stromkollektoren entworfen, um pseudokapazitive Elektroden zu konstruieren, die unter verschiedenen Aspekten untersucht werden sollten. Es handelt sich dabei um Nickel-Nanorod-Arrays (NN), geätzte poröse Aluminiumoxidmembranen (EPAM), die mit einer SnO_2-Schicht beschichtet sind (EPAM@SnO_2), und in EPAM eingeschlossene Nickel-Nanodrähte (NiNWs-EPAM):

Zunächst wird die Rolle von NN-Nanoarchitekten-Stromkollektoren in Superkondensator-Elektroden mit den pseudokapazitiven Materialien bei hoher Massenbelastung und dicker Schicht bewertet. Durch die elektrochemische Leistungs- und Impedanzanalyse der Elektroden mit und ohne die NN-nanoarchitektierten Stromkollektoren wird die Validierung des Designs von Dickschichtelektroden auf der Basis von nanoarchitektierten Stromkollektoren demonstriert.

Zweitens werden EPAM@SnO_2-Gerüste als nanoarchitektonische Stromkollektoren für Nanoelektroden entworfen und eingesetzt, um die Energiedichte des Mikro-Superkondensators (MSC) zu verbessern. Dank der orientierten und robusten Nanokanäle in EPAM@SnO_2 können

die daraus resultierenden Nanoelektroden sowohl die effektive Ionenmigration als auch die sehr große elektroaktive Oberfläche innerhalb des begrenzten Footprints synergetisch nutzen. Ein MSC wird schließlich konstruiert und weist eine rekordverdächtig hohe Leistung auf, was auf die Umsetzbarkeit des derzeitigen Designs für Energiespeichervorrichtungen hindeutet.

Drittens wird der NiNWs-EPAM nanoarchitektierte Stromkollektor hergestellt, um nicht aggregierende und robuste eindimensionale (1D) Nanoelektroden-Arrays zu konstruieren. Das EPAM verhindert die Selbstaggregation von 1D-Nanoelektroden-Arrays und verleiht ihnen gleichzeitig eine hohe strukturelle Integrität und elektrochemische Stabilität während der Montage und des Betriebsprozesses der Geräte. MSCs, die mit diesen nicht aggregierenden und robusten 1D-Nanoelektroden bestückt sind, erreichen eine bemerkenswerte Energiespeicherleistung.

Die im Rahmen dieser Arbeit zu nanoarchitektonischen Stromkollektoren für Superkondensatoren erzielten Ergebnisse geben einen Ausblick auf den Entwurf zukünftiger Energiespeicher und -wandler.

Acknowledgement

First and foremost, I would like to express my sincere gratitude to my advisor Prof. Dr. Yong Lei for his continuous support of my Ph.D. study in his research group at Technische Universität Ilmenau campus. His patience, motivation, and immense knowledge deeply affected me. It is truly an honor to be his student. I appreciate all his contributions of time, encouragement, support, and guidance to make my Ph.D. experience enjoyable and productive.

Besides my supervisor, I would like to specially thank Dr. Huaping Zhao for his insightful guidance and suggestions, which inspired me to widen my research from various perspectives. Moreover, I would like to thank all the group members for the academic issues. Many thanks go to Dr. Yang Xu for his discussions and helps in electrochemical storage field. Also, I thank my fellow labmates: Dr. Yaoguo Fang, Dr. Jiale Xie, Dr. Junhua Zhao, Dr. Ahmed Shukur Hameed Al-Haddad, Mr. Mo Sha, Mr. Chenglin Zhang, Mr. Yuhan Wu, Mr. Chengzhan Yan, Ms. Yulian Dong, Ms. Jiajia Qiu and Ms. Melanie Waltinger for their kind help in my work.

I am also grateful to the following university staffs: Dr. Arne Albrecht, Mr. Dominik Flock, Dr. Henry Romanus, Dr. Alexander Groß, Prof. Uwe Ritter, Dr. Eric Täuscher, Mr. Joachim Döll, and Dr. Anna Dimitrova for their support and assistance in the aspect of materials characterization.

A very special gratitude goes to the China Scholarship Council (CSC) for providing me with the living allowance during the period of doctoral study. Last but not least, I would like to appreciate my family for supporting me spiritually through the most difficult time.

Table of Content

List of Figures

List of Abbreviations

1D	One-dimensional
2D	Two-dimensional
3D	Three-dimensional
A	Footprint area of device
ACN	Acetonitrile
ALD	Atomic layer deposition
AZO	Al-doped ZnO
BSE	Backscattered electrons
C	Capacitance value
CCT	Colloidal crystal template
CDC	Carbide-derived-carbons
C_{dl}	Double-layer capacitance
CE	Chemical etching
CV	Cyclic voltammogram
CVD	Chemical vapor deposition
DHBT	Dynamic hydrogen bubble template
E	Energy density
EA	Electrochemical anodization
EC	Electronic current
ECSA	Electrochemically active surface area
ED	Electrodeposition
EDLC	Electric double-layer capacitor
EIS	Electrochemical impedance spectroscopy
$EMIMBF_4$	1-ethyl-3-methylimidazoliumtetrafluoroborate
EMIM-TFSI	1-ethyl-3-methylimidazolium bis(trifluoromethylsulfonyl)imide
EPAM	Etched porous alumina membrane
EPAM@SnO_2	SnO_2 deposited on the EPAM
PPy	Polypyrrole
EPAM@SnO_2@PPy	PPy deposited on EPAM@SnO_2
MnO_2	Manganese oxide

EPAM@SnO_2@MnO_2	MnO_2 deposited on EPAM@SnO_2
EPAM@SnO_2//EPAM@SnO_2	EPAM@SnO_2 symmetric configuration
ESR	Equivalent series resistance
F	Faraday constant
f_0	Frequency at phase angle of −45°
GCD	Galvanostatic charge–discharge
HT	Hydrothermal
I	Current
IC	Ionic current
IR	Voltage drop
ITO	Tin-doped indium oxide
M	Molar mass
m	Active electrode mass
$Mn(Ac)_2$	Manganese acetate
MSC	Micro-supercapacitor
MXenes	Two dimensional transition metal carbides and nitrides
$Na(Ac)_2$	Sodium acetate
Nb_2O_5	Niobium pentoxide
NF	Ni planar foil
NF@MnO_2	MnO_2 deposited on Ni planar foil
Ni	Nickel
NiNWs	Nickel nanowires
NiNWs-EPAM	Nickel nanowires confined into EPAM
NiNWs@MnO_2-EPAM	MnO_2 deposited on NiNWs-EPAM
NiNWs@PPy-EPAM	PPy deposited on NiNWs-EPAM
NN	Ni nanorod arrays
NN@MnO_2	MnO_2 deposited on Ni nanorod arrays
P	Power density
PAM	Porous alumina membrane
PANi	Polyaniline
PC	Pseudocapacitor
PECVD	Plasma enhanced chemical vapor deposition

PEDOT	Poly(3,4-ethylenedioxythiophene)
PMMA	Polymethyl methacrylate
PS	Polystyrene
PTFE	Polytetrafluoroethylene
PVD	Physical vapor deposition
PVDF	Polyvinylidene fluoride
Py	Pyrrole
Q	Capacity in Coulomb
R_{ct}	Charge transfer resistance
R_s	Resistance of the electrochemical system
RuO_2	Ruthenium oxide
SC	Supercapacitor
SE	Secondary electrons
SEM	Scanning electron microscopy
SnO_2	Tin oxide
SNTAs	Sandwich-structured nanotube arrays
TEM	Transmission electron microscope
V	Voltage
WC	Wood carbon
z	Number of electrons
ZTO	Zn_2SnO_4
Δt	Discharge time
τ_0	Relaxation time constant
ν	Potential scan rate
//	Two electrodes configuration

1 Introduction

With the potential depletion of fossil fuels and rapid deterioration of the environment in connection with greenhouse gas emissions, there is a massive global effort to develop clean and sustainable energy supplies as well as advanced energy conversion/storage systems. The renewable sources in the environment, such as light, wind, wave motion, or temperature variations, are believed to be the most promising means for addressing these concerns. However, renewable energy sources from nature usually have certain intermittency or randomicity, which need to be supplemented by the energy storage components. For this reason, it is an ever-rising demand for designing electrochemical energy storage (EES) units as the energy buffer. Among them, rechargeable batteries and supercapacitors represent two leading EES systems that cater to energy storage needs. At present, owing to their large energy density (up to 180 Wh kg^{-1}), lithium-ion batteries are broadly applied in consumer electronics. However, they always suffer from the limited power delivery, which is largely caused by the sluggish electron and ion transportation within the batteries. In addition, there are huge heat congregation and internal dendrites formation during the battery operation, which gives rise to serious safety issues. Apart from that, they need to take hours to recharge when batteries are drained. By contrast, supercapacitor as one of the complementary or alternative technologies for batteries can securely deliver high power with superior long cycle life (>100,000 cycles). Therefore, they have opened up the field of research where high power delivery, fast electrochemical response, and high cyclic stability are needed. To date, supercapacitors (SCs) are already widely used in aircraft, automobiles, buses, trains, cranes, and elevators for intermittent renewable energy sources and regenerative braking of electric vehicles and light rail. Though SCs have a relatively high energy output of ~5 Wh kg^{-1} compared to those of traditional solid-state electrolytic capacitors, it is still far below those of batteries (~200 Wh kg^{-1}).[1] Thus, current

extensive research efforts are focused on optimizing the energy-storage capability of SCs without compromising their superior power density as well as cycling stability.

As known, the energy density (*E*) of SCs is directly proportional to the device capacitance (*C*) and the square of voltage window (*V*), according to the equation of $E = 1/2 \times C \times V^2$. Accordingly, the main strategies to boost the energy density include improving the device capacitance and/or enlarging the operational voltage. For enlarging the operational voltage, the adoption of asymmetric device configuration and the optimization of appropriate electrolytes (*e.g.*, organic electrolytes, gel polymer electrolytes, and ionic liquid electrolytes) are highly advocated ways. With respect to improving the device capacitance, the adopted approaches are determined by the charge storage mechanism of SCs. Generally, there are two major kinds of SCs, electric double-layer capacitors (EDLCs) and pseudocapacitors. EDLCs utilize reversible and purely electrostatic ion adsorption at the interface of electroactive materials and electrolytes to store charge, and thus the key to improving the energy density of EDLCs is to largely increase the specific surface area of the electrode. In comparison, the charge storage in pseudocapacitors involves the rapid and reversible redox reactions occurring at the surface of pseudocapacitive materials, which have high theoretical specific capacitance. Thus, pseudocapacitors hold great promise for improving the energy densities of SCs, however, most pseudocapacitive materials show practical capacitances far below their theoretical ones, which the main reasons include the poor electrical conductivity and sluggish charging-discharging behavior of most pseudocapacitive materials. To this end, pseudocapacitive electrode design based on nanoarchitectured current collectors is emerged as one of the efficient solutions to address the poor electrical conductivity issue toward realizing the full potentials of pseudocapacitive materials for SCs with high energy densities.

In this dissertation, perfectly-ordered porous aluminum oxide membrane (PAM) is utilized as the nanostructuring template to design and fabricate nanoarchitectured current collectors, and

thereafter to construct pseudocapacitive electrodes for finally realizing high-performance SCs. The major achievements of this dissertation include the following three aspects:

(1) *Evaluating the role of nanoarchitectured current collectors in energy storage capability of SCs electrodes with thick pseudocapacitive materials layers.* Pseudocapacitive materials are generally in the form of ultrathin conformal coating in SCs electrodes based on nanoarchitectured current collectors, thus the resultant low mass loading of pseudocapacitive materials largely limits the applications of nanoarchitectured current collectors. Here, SCs electrodes with nickel (Ni) nanorod arrays as nanoarchitectured current collectors and manganese dioxide (MnO_2) as pseudocapacitive materials are fabricated to study the role of nanoarchitectured current collectors in determining the energy storage capability when pseudocapacitive materials are in thick layer rather than ultrathin conformal coating. Electrochemical analysis revealed that Ni nanorods could create numerous electrical conductive tunnels in the thick-layer electrodes to dramatically alleviate the contact resistance at the pseudocapacitive-materials/current-collectors interface. With 1-μm thick MnO_2 layer, the Ni nanorods based electrodes have much higher areal capacitance than those with Ni foils as current collectors, which is more than 6 times of that with the same MnO_2 mass loading or more than 18 times of that with the same 1-μm thick MnO_2 layer. Moreover, better rate capability and higher structural stability was maintained in Ni nanorods based electrodes even with 3-μm thick MnO_2 layer. These results open up new opportunities for nanoarchitectured current collectors to construct SCs with superior energy storage capability.

(2) *Construction of pseudocapacitive nanoelectrodes based on rationally designed nanoarchitectured current collectors for achieving micro-supercapacitors (MSCs) with high energy and power densities.* MSCs are of great significance as miniaturized power source for microelectronics but still face challenge of limited energy. Nanoelectrodes are acknowledged as an efficient approach to address this challenge for MSCs. Herein, we demonstrate

pseudocapacitive nanoelectrode design strategy based on highly-etched porous alumina membranes (EPAMs). The insulating EPAMs with high specific surface area is transformed to be conductive by coating an ultrathin layer of tin oxide (SnO_2) and thereafter functions as nanoarchitectured current collectors, upon which pseudocapacitive materials are deposited to produce nanoelectrodes through depositing pseudocapacitive materials (*i.e.*, MnO_2 and polypyrrole (PPy)). Such nanoelectrodes allow synergize the effects of both effective ion migration and ample electroactive surface area within limited footprint. The as-assembled asymmetric, stacked MSCs can work with a cell voltage up to 3.0 V in ionic liquid electrolyte and deliver a peak energy of 160 μWh cm^{-2} and the peak power reaches 40 mW cm^{-2}, in combination with good rate capability and cycling stability. The comprehensive device areal performance metrics of our MSCs are among the best values achieved for reported MSCs. Our research provides a new paradigm about designing high-performance pseudocapacitive nanoelectrodes for MSCs.

(3) *Design and fabrication of non-aggregative and robust one-dimensional (1D) pseudocapacitive nanoelectrode arrays with a high aspect ratio toward achieving high-performance MSCs.* The construction of ideally erect 1D nanoelectrode arrays with a high aspect ratio will be one of the competent approaches to address the insufficient energy issue faced by MSCs, but is hindered by the generally known unreliable structural properties of high-aspect-ratio 1D nanostructure arrays. Here, we demonstrate an efficient route to design non-aggregative and robust 1D nanoelectrode arrays, in which individual 1D nanoelectrode with a high aspect ratio of 50 is confined in a single nanopore of EPAMs with ultrathin pore wall. The EPAMs prevent the 1D nanoelectrode arrays from self-aggregating and meanwhile endows them with excellent mechanical and electrochemical stability during device assembly and operation process. Furthermore, the EPAMs with an ultrathin pore wall offers ample void along each nanoelectrode within every cell unit of nanoelectrode to allow electrolyte infiltration.

Finally, MSCs are assembled with these non-aggregative and robust 1D nanoelectrodes and exhibit considerable enhancement in energy storage capabilities, including large device capacitance (75 mF cm^{-2}), extraordinary long cyclic stability for 50,000 cycles (82% capacitance retention) and high energy density (84 μWh cm^{-2}). Beyond, MSCs, our strategy provides a promising approach to design ideally erect and robustly stable 1D nanostructure arrays with a high aspect ratio for constructing functional devices with high performance.

2 Pseudocapacitors for energy storage

2.1 The charge storage mechanism of pseudocapacitors

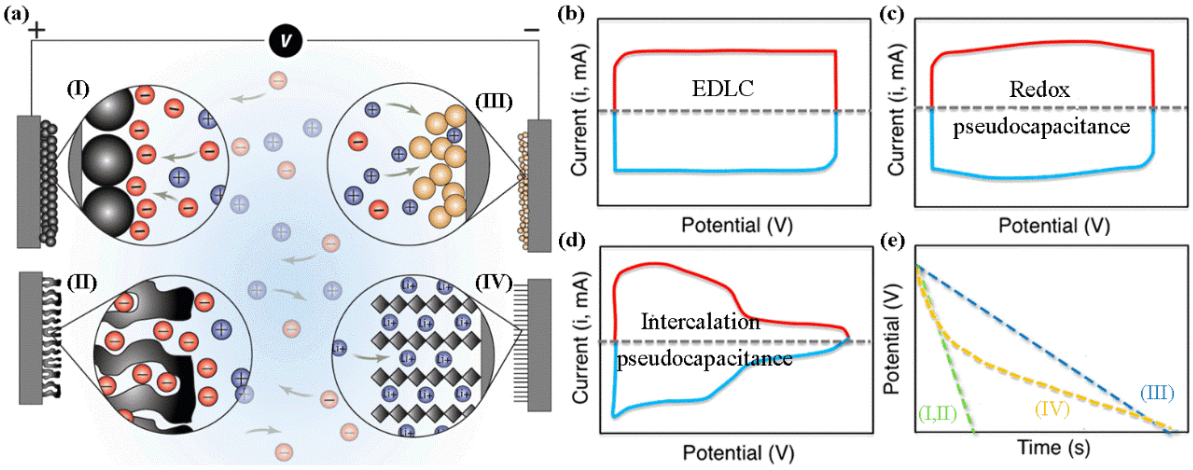

Figure 2-1 (a) The different energy storage mechanisms in SCs, including electric double-layer capacitor (EDLC) at electrodes comprising (I) carbon particles and (II) porous carbon; (III) redox pseudocapacitance; and (IV) intercalation pseudocapacitance.[2] Schematic cyclic voltammograms of (b) EDLC; (c) redox pseudocapacitance; and (d) intercalation pseudocapacitance. (e) Schematic comparison of galvanostatic discharge curves for different energy storage mechanisms in SCs as illustrated in (a).[3]

A full understanding of the energy storage mechanisms in pseudocapacitive materials has great avail to rationally design electrodes for pseudocapacitors (PCs). As depicted in Figure 2-1a, compared with EDLCs storing charge through the formation of double layer that arises from adsorption of negative ions from the electrolyte on the positively charged electrode (carbon particles or porous carbon), redox and intercalation pseudocapacitance are mainly involved in the charge storage mechanisms of pseudocapacitive materials for PCs.[4] With respect to redox pseudocapacitance, charge storage by means of redox reactions occurs in the near-surface region that electrolyte ions are adsorbed onto the surface or near-surface of pseudocapacitive materials, accompanying with Faradaic process.[2] Typical examples include transition metal oxides (*e.g.*, ruthenium oxide (RuO_2) and MnO_2) and conductive polymers (*e.g.*, polypyrrole

(PPy), polyaniline (PANi), and poly(3,4-ethylenedioxythiophene) (PEDOT)).[5] The pseudocapacitance of transition metal oxides arises from fast redox reactions caused by the intercalation of protons or alkali metal cations, while the pseudocapacitance of conductive polymers comes from the redox processes involving the π-conjugated polymer chains during electrochemical doping-undoping.[6] Regarding intercalation pseudocapacitance, the pseudocapacitive materials show pseudocapacitance dependence on the crystalline phase and crystallinity but with independence of capacitance, rates and cyclability on the surface area of the material, resulting in the capacitance to become a volumetric phenomenon.[7] Niobium pentoxide (Nb_2O_5) is one of the typical examples of intercalation pseudocapacitance, and it undergoes fast Faradaic reactions through an intercalation pseudocapacitance mechanism in which reversible lithiation/delithiation occurs in the bulk of the material.[8-9] The principal benefit realized from intercalation pseudocapacitance is that high levels of charge storage could be achieved within short periods of time because there are no limitations from solid-state diffusion. A recently discovered new class of 2D transition metal carbides (MXenes) with a general chemical formula of $M_{n+1}X_nT_x$ (here M stands for a transition metal, X is C and/or N and T_x indicates surface terminations) are also intercalation pseudocapacitance.[10] Besides, there are also some pseudocapacitive materials that store charge via intercalation with partial redox pseudocapacitance.[11-16] The difference of charge storage mechanisms in SCs can also be reflected in cyclic voltammograms and galvanostatic discharge curves.[3] EDLCs show rectangular cyclic voltammograms (Figure 2-1b) and linear voltage responses during galvanostatic discharging (Figure 2-1e), while redox pseudocapacitance has similar cyclic voltammograms and galvanostatic discharge curves as those of EDLCs but with much higher specific capacitance. In contrast, the cyclic voltammograms of intercalation pseudocapacitance show broad but electrochemically reversible redox peaks (Figure 2-1d) and meanwhile the corresponding galvanostatic discharge profile is nonlinear (Figure 2-1e).

2.2 Pseudocapacitive materials

Table 2-1 Summary of some pseudocapacitive oxide materials and polymers in terms of the charge storage behaviors, the theoretical capacitance and the conductivity.

Materials	Electrolyte	Potential window (V)	Pseudocapacitive behavior	Theoretical capacitance (F/g)	Conductivity (S/cm)	Ref.
MnO_2	Na_2SO_4	0.8	redox	1380	10^{-5}–10^{-6}	17
RuO_2	H_2SO_4, Na_2SO_4	1.23	redox	1200–2200	1 (amorphous)	18
NiO	KOH, NaOH	0.5	redox	3750	0.01–0.32	19
Co_3O_4	KOH, NaOH	0.45	redox	3560	10^{-4}–10^{-2}	20
V_2O_5	NaCl, Na_2SO_4	1.0	intercalation	2120	10^{-4}–10^{-2}	21
Nb_2O_5	$LiClO_4$	1.0	intercalation	720	3×10^{-6}	22
Fe_2O_3	Na_2SO_3	1.0	intercalation	~750	10^{-14}	23
α-MoO_3	$LiClO_4$	2.0	intercalation	-	~1.5×10^{-4}	7
Polyaniline	H_2SO_4	1.0	redox	750	0.1–5	24
Polypyrrole	Na_2SO_4	0.8	redox	620	10–50	6
Polythiophene	$LiPF_6$	1.0	redox	485	300-400	25
PEDOT[a]	LiCl	0.8	redox	210	300–500	6

[a]PEDOT: poly(3,4-ethylenedioxythiophene).

The proper choice of pseudocapacitive material is of great importance to the construction of high-performance PC devices. Table 2-1 summarizes the physicochemical properties and the pseudocapacitive behaviors of some typical transition metal oxides and conductive polymers as pseudocapacitive materials. Apparently, these transition metal oxides and conductive polymers have higher specific capacitance in theory than that of EDLCs materials because of the pseudocapacitive behavior taking place during the charge storage process.[26] Besides, the transition metal oxides have relatively superior theoretical capacitances comparing to those of the conductive polymers. On the other hand, different from the conductive polymers, most of

transition metal oxides have the poor electrical conductivity and low cycling stability, which has been considered as the major obstacles toward increasing the energy density while maintaining the high power density of PCs. For this reason, various strategies have to be developed in the past decades in order to afford trade-offs between power and energy density of PCs.

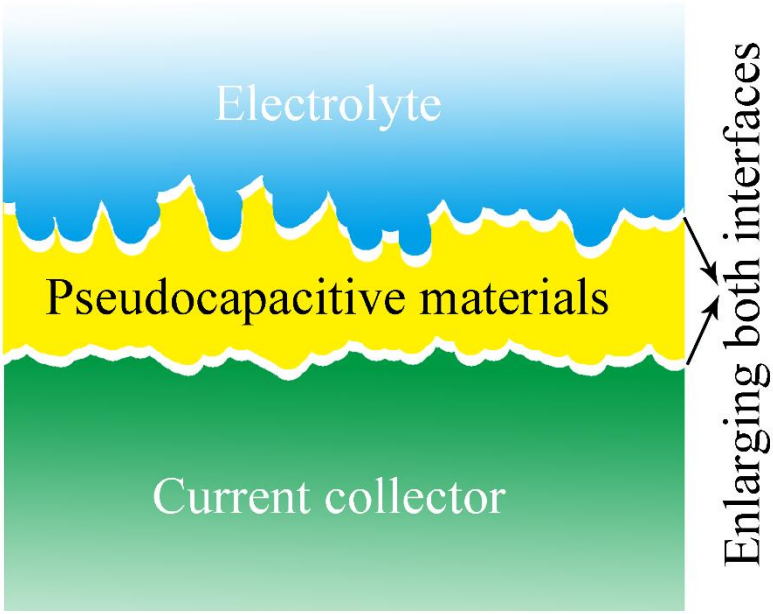

Figure 2-2 Two crucial interfaces in the electrodes determining the energy storage performance of PCs that need to be enlarged.

In the view of the above discussions about the charge storage mechanisms in pseudocapacitive materials and the intrinsic weakness of pseudocapacitive materials themselves, a rationally designed electrode based on pseudocapacitive materials should not only provide larger pseudocapacitive-materials/electrolyte interfaces allowing more pseudocapacitive materials accessible to the electrolyte for reversible Faradaic reactions, but meanwhile offer larger pseudocapacitive-materials/current-collectors interfaces to reduce the charge transport resistance during charge-discharge process (Figure 2-2). As a result, the improved transport characteristics of both charge carriers and ions would enable to reach the full potentials of pseudocapacitive materials for electrochemical energy storage. Therefore, so far the majority

of the developed electrode design strategies revolves around the enlargement of these two interfaces.

2.3 Designing and development of pseudocapacitive electrodes

With different nanostructuring strategies, the pseudocapacitive materials can be synthesized into different nanostructures in the form of either powder or freestanding nanoarrays (generally grown on the surface of a current collector), which both can efficiently increase the specific surface area thus potentially lead to the larger pseudocapacitive-materials/electrolyte interfaces.[27] For powdery ones, they are firstly mixed together with polymeric binder (*e.g.*, polytetrafluoroethylene (PTFE), polyvinylidene fluoride (PVDF)) and conductive additives (*e.g.*, carbon black), and then are pasted on a bulk current collector, such as metal foils (like aluminum, copper, titanium), metal foam, and carbon substrates (such as carbon paper and carbon cloth), etc., to finally construct an electrode (Figure 2-3a). Here, the insulated polymeric binders make up the "dead volume" in the electrode, which will finally lead to the inferior performance. With respect to the free-standing nanoarrays grown on a current collector, they will be directly used as electrodes without the necessities of polymeric binders and conductive additives. Especially, the absence of polymeric binders will help to release more room for electrolyte ions infiltration in and create large pseudocapacitive-materials/electrolyte interfaces, which are considered to promote fast and reversible surface redox reaction (Figure 2-3b). Yet in both cases, the longitudinal charge transfer is seriously impeded due to the limited contact area between pseudocapacitive materials and current collectors, and finally results in a low charge transfer efficiency as well as a low rate capability. On the other hand, the configuration of these electrodes still suffers from the low utilization efficiency of the pseudocapacitive materials since the reversible redox reaction only occurs on the surface or in the first few tens or hundreds nanometers from the surface of pseudocapacitive materials.[28] Accordingly, the above mentioned nanostructuration of pseudocapacitive materials is apparently not good

enough to meet the critical challenges (*e.g.*, low utilization of pseudocapacitive materials, as well as the inferior longitudinal charge transfer) for the construction of high-energy-power PCs.

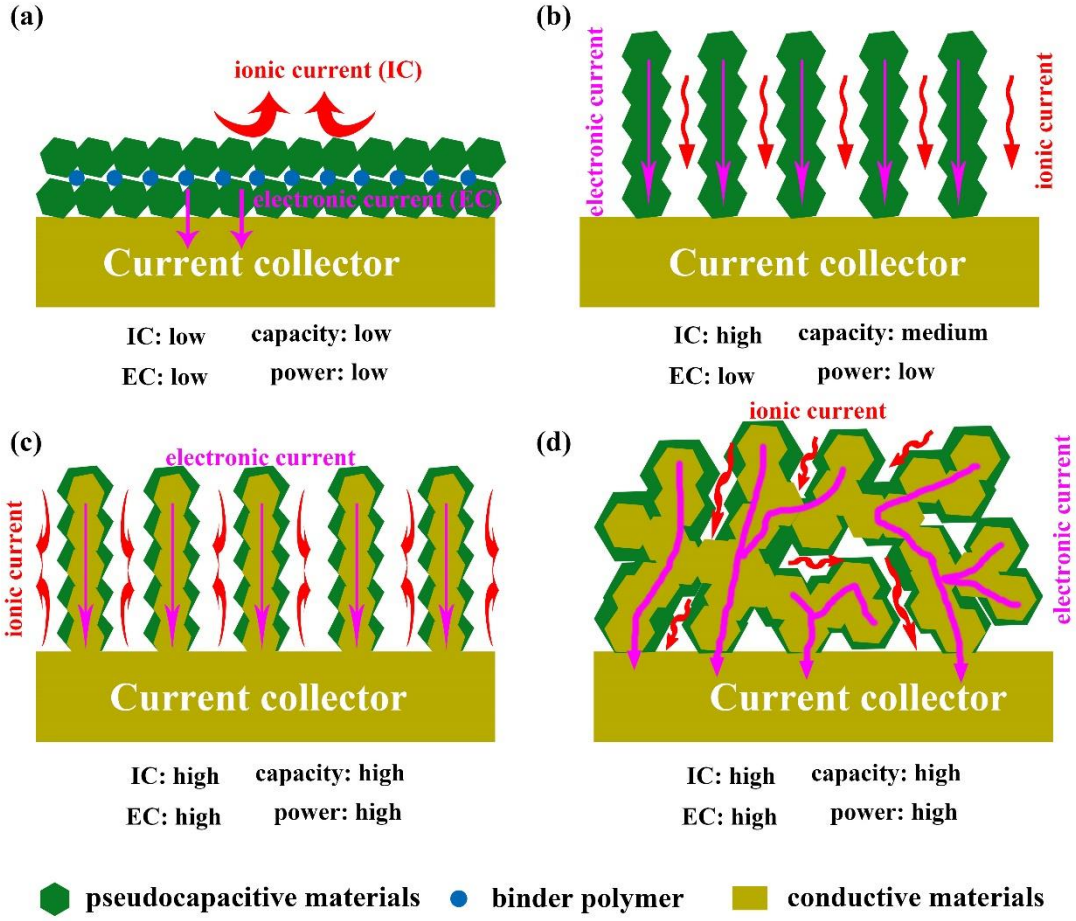

Figure 2-3 Rational design of pseudocapacitive electrodes for PCs. Pseudocapacitive electrodes with pseudocapacitive materials in the form of (a) powder and (b) freestanding nanoarrays. Pseudocapacitive electrodes with the help of (c) nano-arrayed and (d) nano-porous current collectors. The red and pink arrows signify the ionic (IC) and electronic current (EC), respectively.

Additionally, there is an indirect but efficient way to achieve this goal by means of nanoarchitectured current collectors. Briefly, the conventional bulk current collectors are firstly fabricated into nanostructured ones, and then a thin layer of pseudocapacitive materials is conformally coated onto the nanoarchitectured current collectors to produce heterogeneous electrodes for PCs. The application of nanoarchitectured current collectors would not only

provide larger interfaces between pseudocapacitive materials and current collectors, but also act as an excellent nanostructuring platform enabling the nanostructuration of pseudocapacitive materials (Figure 2-3c-d). And similar to the free-standing nanoarrays of pseudocapacitive materials grown on a bulk current collector, these heterogeneous electrodes with nanoarchitectured current collectors are also free of polymeric binders and conductive additives. The key of electrodes nanostructuring in PCs is therefore laying in the fact of nanoarchitectured current collectors development and fabrication. Nevertheless, the aspect of pseudocapacitive electrodes based on nanoarchitectured current collectors is still lack of enough concern.

3 Design concept and advantages of nanoarchitectured current collectors for pseudocapacitors

As aforementioned, nanoarchitectured current collectors provide large conductive surface area to improve the charge transport efficiency in pseudocapacitive electrodes. Therefore, to fabricate the PC devices with remarkable energy densities while maintaining high power densities, the design core lies in the nanostructure of the conductive substrate in the electrodes.

3.1 Design philosophy of nanoarchitectured current collectors

To be an ideal nanoarchitectured current collectors for PCs, there are principally involved three basic design considerations as illustrated in Figure 3-1:

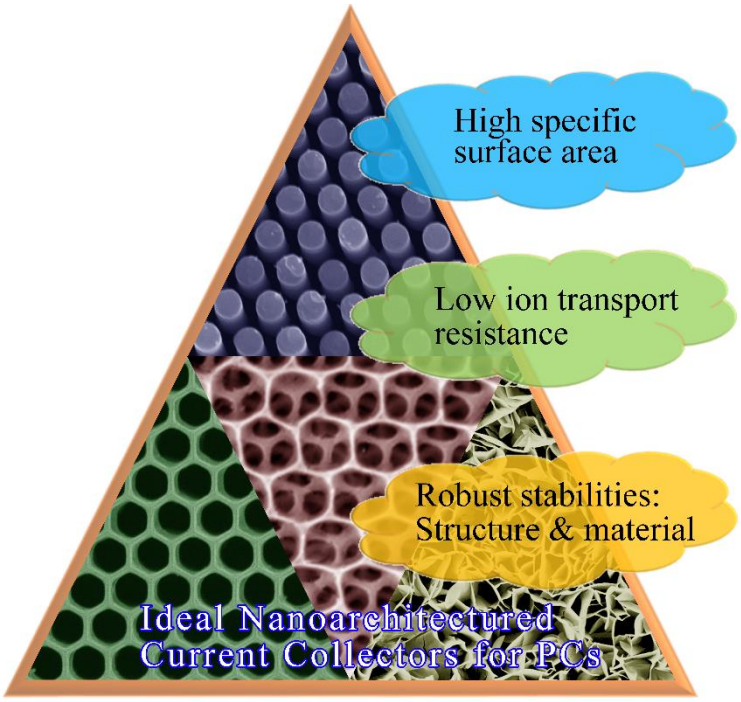

Figure 3-1 Basic design considerations about the construction of nanoarchitectured current collectors for PCs.

First, high specific surface area for the deposition of pseudocapacitive materials. An increased surface area of current collectors will dramatically enlarge the contact areas between pseudocapacitive materials and current collectors, and hence significantly reduce interfacial

resistance. Rapid electron transport can be achieved with a low resistance across the entire electrode due to the long-range electrically conductive backbones of the nanoarchitectured current collectors. In addition, nanoarchitectured current collectors with large specific surface area will also serve as nanostructuring platform to produce much larger pseudocapacitive materials/electrolyte interfaces allowing more pseudocapacitive materials accessible to the electrolyte for reversible Faradaic reactions (Figure 2-2). Since high specific capacitance even nearly reaching the theoretical value can be only achieved when pseudocapacitive materials are conformally coated on nanoarchitectured current collectors in the form of an ultrathin layer, high specific surface area of nanoarchitectured current collectors allows to deposit more pseudocapacitive materials still by means of ultrathin conformal coating to realize the increased mass loading of pseudocapacitive materials but without distorting high specific capacitance. As a result, the energy density of PCs will be significantly improved.

Second, low ion transport resistance for facilitating redox kinetics. Besides to provide large contact area between pseudocapacitive materials and current collectors, a rationally designed nanoarchitectured current collector should comprise of the interconnected and unimpeded channels for electrolyte permeation and ion transportation throughout the whole electrode, allowing the easy and rapid access of the electrolyte ions to the all surface area of pseudocapacitive materials in the finally fabricated heterogeneous electrodes. The improved ionic behavior will facilitate the redox kinetics occurring at the surface of the pseudocapacitive materials during fast charging and discharging process, thus improving the utilization efficiency of the pseudocapacitive materials and enhancing the rate performance of PCs.

Third, robust stabilities of the nanoarchitectured current collectors regarding both structure and materials. Ideal nanoarchitectured current collectors should be an integrated structure with robust structural stability to maintain the continuous ion channels in electrodes both after the device assembly and during the long-termed cycling to provide the pseudocapacitive materials

with sufficient accessibility to the electrolyte. Additionally, the materials of nanoarchitectured current collectors should have enough chemical resistance to both the pseudocapacitive materials and the electrolytes in order to suppress the side reactions during charging and discharging process.[42]

In short, these basic design considerations of nanoarchitectured current collectors are aiming to tackle the specific issues that PCs have faced, including low electrical conductivity, limited electrochemical active sites, and long diffusion length for mass and charge transport as well as cycling stability. Hence, many strategies have been proposed to fabricate nanoarchitectured current collectors to fulfill these basic requirements and so far significant progress has been achieved.[31, 43-44] With the help of nanoarchitectured current collectors, the as-prepared heterogeneous electrodes have exhibited the boosted energy storage capacity, without suffering from sluggish charging-discharging behavior and a limited lifetime. In the following section, we provide some typical examples to illustrate the rational design of nanoarchitectured current collectors with different geometries for PCs by different fabrication strategies.

3.2 Fabrication strategies for nanoarchitectured current collectors

As a conductive scaffold and one of the crucial components in electrode, the fabrication of nanoarchitectured current collector for the construction of high-performance PCs is of key importance. Particularly, nanoarchitectured current collectors with 1D/2D arrays and 3D porous morphology are of wide general appeal. Many preparation technologies have been adopted in accordance with the design philosophy that the previous section has been proposed. In brief, the fabrication of nanoarchitectured current collectors is the process of nanoengineering of conductive materials, and thus most of the existing strategies for the synthesis can be classified into two major categories – template-free and template-assisted strategies – depending on whether a sacrificial template is required.

3.2.1 Template-free methods for nanoarrayed current collectors

As their name suggest, the template-free approaches are not only free from the template removal issues, but also from the rigid morphology provided by hard templates.[45] Their working principle lays in the fact that the precursors participate in a series of facile chemical changes to finally obtain desired product through a self-assemble process.[46-51] This includes liquid phase strategies (precipitation method, hydrolysis method, solvothermal reaction, spraying method, emulsion method, and sol-gel method, etc.), vapor phase solutions (chemical vapor deposition (CVD), physical vapor deposition (PVD), etc.) and etching method, etc.

Hydrothermal methods. As a niche in the field of template-free synthesis, hydrothermal methods based on liquid-solid growth mechanism are used to build 1D/2D nanoarrayed structures with features of high versatility and generality.[52] The procedures involve the formation of an architecture from a liquid medium without imposing high vacuum or current or voltage, so the complexity and cost of fabrication process are largely reduced. Vertical aligned nanowires or nanowalls of metal oxides (ZnO, SnO_2, Co_3O_4, and Fe_3O_4, etc.), nitrides and sulfides can be well prepared and immobilized to the conductive substrate.[53] The single-crystalline nature of the product endowed by the oriented growth of hydrothermal condition, considerably improves the electron mobility. Numerous studies have witnessed the desired functions they offered when combined with pseudocapacitive materials.[53-60] Generally, the shell layer of pseudocapacitive materials conformally grows on the core nanoarrays by another facile hydrothermal way.[53, 55, 58, 61] In addition to the high conductive oxides, nitrides, and sulfides nanoarrays to serve as cores, they also participate in redox reactions to contribute to the electrochemical charge storage.[62] Finally, a strong synergistic effect can be achieved for these heterogeneous electrodes.

Etching and anodization. Metal assisted chemical etching is a technique primarily for the fabrication of silicon (Si) nanoarrays with the ability to control various structural parameters,[63-

[64] since Si nanoarrays are well-documented as promising current collectors in the field of energy storage devices.[65] The working principle of etching process can be simply summarized: the Si substrate covered with isolated noble metal particles is etched by HF and H_2O_2 mixed liquid, employing a top-down approach to finally obtain vertically aligned Si nanowires. Likewise, anodic oxidation of Ti substrate is also a conventional top-down strategy for fabrication of TiO_2 nanotube arrays.[67-69] Due to the highly oriented structure with large surface area, TiO_2 nanotube arrays serve as an attractive scaffold for pseudocapacitive materials. Especially in the case when TiO_2 nanotube arrays are conducted through hydrogenation, polarization, nitridation or sulfidation process to improve their conductive ability.[70-72]

CVD methods. The recent popularity of vertically aligned carbon nanotube and graphene nanosheet arrays once again put the plasma enhanced chemical vapor deposition (PECVD) approach in the spotlight.[73-74] Because it holds large universality and is applicable toward not only majority of carbonaceous materials, but also other desirable conductive oxide materials (SnO_2, tin-doped indium oxide (ITO), Al-doped ZnO (AZO), and Zn_2SnO_4 (ZTO), etc.).[75-80] In a typical PECVD method, for instance, CNTs are fabricated with Ni seeded carbon cloth as a substrate at a reaction chamber, where the chemical reactions occur between the vapor of target materials and other indispensable gases at high temperature and high vacuum.[73-74] As known, CVD method is not limited to nanoarrayed structure construction, it also takes place in the field of 3D nanofoam or nanosponge architecture fabrication, which will be elaborated in the "*CVD-template method"* in section of 3.2.4.

3.2.2 Template-free methods for nanoporous current collectors

Template-free methods for the nanoporous current collectors are not limited to a single strategy. Some promising fabrication routes, such as dealloying approach, dynamic hydrogen bubble template, reduction technique and combustion synthesis, are highlighted below.

Dealloying approach. 3D bicontinuous metallic nanoporous network can be prepared through a simple dealloying process.[81] Briefly, the active metallic elements in the binary alloy are dissolved by an etching liquid, leaving a crosslinked porous skeleton. One typical example is nanoporous gold substrate,[82] which is fabricated from chemically dealloying of silver-gold alloy. Besides, many other metallic nanoporous structures prepared from this method have been reported, *e.g.*, Pt, Ag, Pd, Fe, Cu, Co, Ni, Ti, Mn, Cr and alloy nanoporous networks.[83-87] These nanoporous metallic networks possess a high bicontinuous porosity with large surface-to-volume ratio, tough mechanical integrity, and are steadily gaining wide popularity for building heterogeneous electrodes.

Dynamic hydrogen bubble template (DHBT) method. One-pot dynamic hydrogen bubble template (DHBT) method is also an efficient way for the fabrication of metallic porous structure.[88] Specifically, vigorous hydrogen bubbles firstly evolve on the substrate at a large over-potential and thus disturb the deposition of metallic materials in those regions. During this period, the metal ions quickly grow between the gas bubbles.[89] Once removing the applied voltage, gas bubbles disappear and the nanoporous structure is formed. Here, the hydrogen bubbles behave more like a template and shape the internal void to finally lead to the foam-like metallic structure. The DHBT method is widely applicable for large range of single metals (*e.g.*, Au, Pt, Ag, Pd, Ni, Cu, Sn, etc.) and binary alloy (*e.g.*, CuZn, CuAu, PtAu, CuPd, CuAg, AuPd, etc.) systems.[90-95]

Reduction technique and combustion synthesis. Chemical reduction technique is conducted through chemical-/electro-reduction of metallic compounds at a low but constant temperature.[96-98] One representative model reported in the literature is the Ag nanoporous structure, which is obtained from the one-step electroreduction of silver halides.[96] The well-made Ag nanoporous structure by this method has the ability to subtly control the ligaments and pore sizes (50-300 nm), which is primarily because of the diverse size of the halide ions

(Cl^-, Br^-, and I^-) in the precursors. The combustion synthesis also termed self-propagating high-temperature synthesis is an efficient way via decomposition of energetic substances to obtain metallic foam-like structure.[99] This combustion synthesis approach offers a versatile and scalable technique for construction of metal foams, which are tailored for the construction of free-standing nanoporous current collectors.

3.2.3 Template-assisted methods for nanoarrayed current collectors

Template-assisted methods have been extensively utilized in the nanoengineering regulation and nanoarchitecture design.[31, 34, 100-103] With template well attached to the bulk conductive substrate, one can easily achieve in-situ free-standing nanoarchitectured current collectors.

PAM template-assisted methods. Due to the versatile and particularly simple approaches, PAM template methods hold the great potentials for the construction of nanoarrayed structures. So far, the PAM template-assisted methods combine with other techniques like electrochemical deposition, atomic layer deposition (ALD) and CVD, have been utilized to fabricate 1D nanoarrays of metals, conductive oxides, silicon and carbonaceous materials.[34, 104-105] Generally, the current practice for producing 1D nanoarrayed current collectors is following two critical steps, as shown in Figure 3-2: (1) deposited the conductive materials into the pores of PAM, and then (2) the product obtained after removing PAM template. The final arrays either in the form of nanowires or nanotubes strictly inherit the structural features from PAM templates. As known, for PAMs, their pore size and membrane thickness can be well tuned through wet chemical pore-widening process and anodization time, respectively.[106-111] Therefore, one can easily obtain nanoarrays with the ability to control the structural parameters by tuning of the applied PAM template as required. Particularly, the pre-patterned Al foils before preparation has been developed recently that can make highly ordered nanoarrays.[112-114] Similar to PAM template approach, the polycarbonate-membranes template has also been utilized to prepare nanoarrayed current collectors based the same procedures.[115]

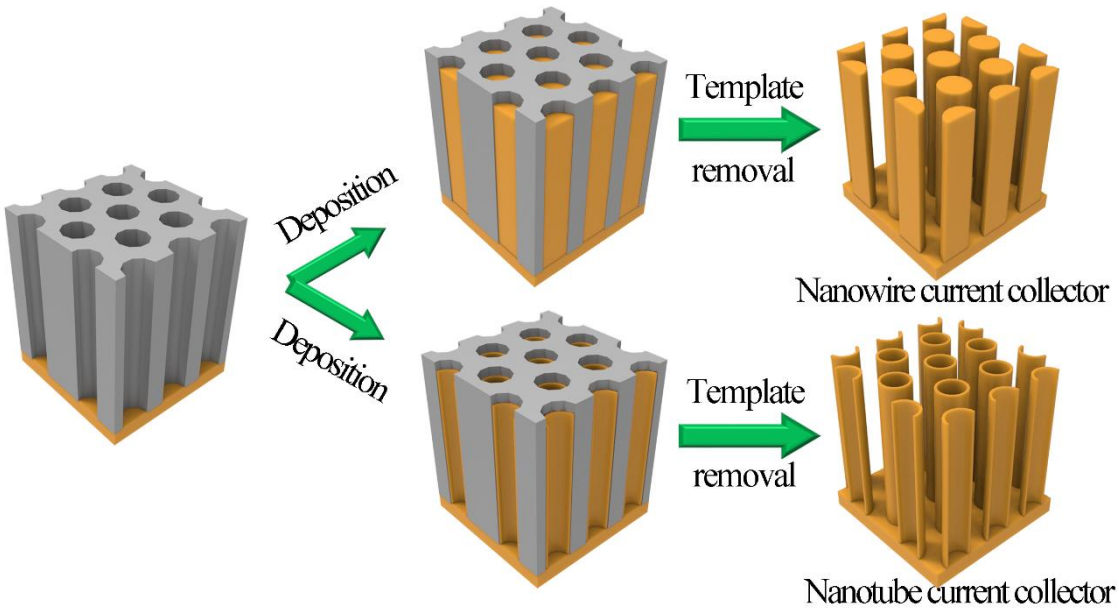

Figure 3-2 Schematic of the preparation process of the typical nanowire/nanotube current collector from the PAM template.

ZnO template-assisted method. Besides, ZnO nanowire arrays are also employed as the sacrificial template to preferentially realize nanotube arrays.[116] Briefly, the ZnO template method can be depicted as follows: (1) conformally wrapping the well-prepared ZnO nanowire arrays with conductive materials, and then (2) removing the ZnO template via etching to obtain nanotube arrays. Notably, the inner diameter of tubes can be well controlled by tuning the size of the ZnO nanowires template and their wall thickness depends on the amount of deposited conductive materials. However, comparing to the PAM template method, the final nanotubular arrays favorably share a random orientation morphology caused by the natural disordered growth of ZnO nanowire arrays.

3.2.4 Template-assisted methods for nanoporous current collectors

3D freestanding interconnected nanoporous current collector possesses conductive network with various pore size, pore size distribution and porosity channels in its internal space. For the moment, there are some widely-reported template-assisted methods to prepare 3D nanoporous

conductive network, such as colloidal crystal template method, replicable PAM template method, and CVD-template synthesis, etc.

Colloidal crystal template-assisted method. Colloidal crystal template method is one of the promising strategies to construct interconnected porous materials.[117-119] Firstly, under appropriate conditions, colloidal spheres (usually polystyrene (PS) and silica spheres) self-assemble into a multilayered and ordered unit with a face-centered cubic stacking mode on a conductive substrate. Then, the conductive materials are deposited by virtue of some specific techniques (such as ALD, electrodeposition, thermal evaporation deposition). Finally, the template is removed via facile dissolution or air-annealing process to achieve an inverse opal structure with numerous feasible bicontinuous spherical voids. The precise pore size and morphology can be well controlled for an inverse opal conductive network. For example, a Ni inverse opal architecture is fabricated through colloidal crystal template method.[120-122] Through subsequent acid etching process, the pore size in the Ni inverse opal can be finely tuned, reducing internal dead volume and making more room for the active materials.[120] Similar structures of chemically modified graphene are prepared through a PS templates embossing process.[118]

Two-step replication PAM method. Recently, a two-step replication PAM method is emerged and exhibits a good controllability for designing porous architecture.[123-124] Since Masuda and Fukuda firstly proposed in 1995,[125] this approaches toward unique porous architectures have drawn great interest and gradually been utilized in conductive scaffold for PCs. Different to the conventional one-step PAM template method, the key fabrication steps involve: (I) deposition of an ultrathin Au layer on the top of PAM template, (II) injection and polymerization of methyl methacrylate, (III) removal of PAM template, (IV) electrodeposition of metallic materials inside polymethyl methacrylate (PMMA) negative type, (V) dissolution of PMMA to obtain final product. The well-prepared Ni nanopore arrays possess ordered vertical aligned pores as the pristine PAM template. The nanopores

structure is just inverted to 1D nanowire arrays obtained from one-step PAM template method, yet the former offers major structural advantages over the latter. Because the nanowire arrays suffer from serious agglomeration with increasing aspect-ratio, while the nanopores structure never fear the collapse even in a relatively high aspect-ratio thanks to the self-supported nanopore arrays with robust mechanical stability. The elevated aspect-ratio of nanopore arrays would boost the specific surface area, and have the potential to increase the mass loading of active materials without sacrificing internal channel space, and meanwhile keep excellent electron transport pathways in three dimensions.[123] This approach demonstrated here may also give some clues for studies related to other nanochannel structures.

CVD-template method. This method is more applicable to build the 3D graphite nanofoams.[126-128] The graphite nanofoam structures with the unique merits of lightweight, highly conductive, and stable make them a promising candidate toward nanoarchitectured current collectors. The main fabrication procedure for this structure includes (1) the preparation of 3D Ni porous network simply by an electrodeposition way to serve as a hard template, (2) the conformal growth of the graphite layer on the Ni porous network via CVD technique, (3) the removal of the Ni sacrifice template to obtain 3D graphite nanofoam. The volume density and quality of graphite nanofoams can be easily tuned according to the various CVD operating parameters (*e.g.*, gas flow rate, growth time, or other conditions).

In short, two major categories toward fabrication strategies for nanoarchitectured current collectors are demonstrated: template-free method and template-assisted method. For the design of the nanoarchitectured current collectors, it seems better to employ sacrifice template (*e.g.*, PAM template) to achieve highly-ordered and vertically-aligned nanoarrays, with all structural parameters being well tuned and tailored by your own ideas. After all, a prototype of PCs electrode is largely dependent on the morphology of nanoarchitectured current collector, and

one can achieve it through conformally depositing pseudocapacitive materials on this framework.

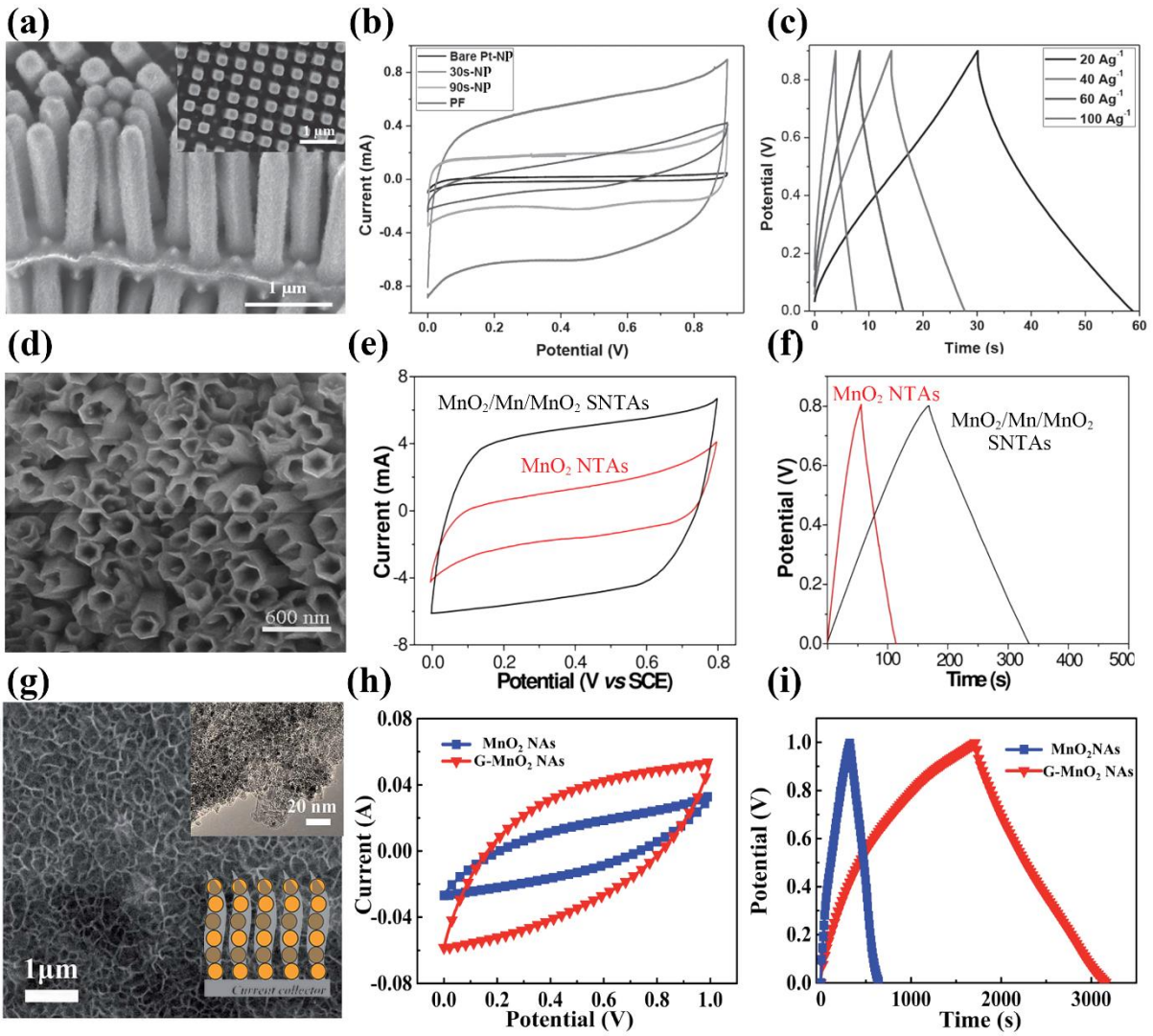

Figure 3-3 Typical examples of heterogeneous electrodes based on nanoarrayed current collectors. (a) Side and top view scanning electron microscopy (SEM) images and (b-c) the electrochemical performances of core@shell Pt@MnO_2 nanopillars.[109] (d) The SEM image and (e-f) the electrochemical performances of MnO_2/Mn/MnO_2 sandwich-structured nanotube arrays (SNTAs).[131] (g) SEM and transmission electron microscope (TEM, inset) images as well as electrode model (inset) and (h-i) the electrochemical performances of G-MnO_2.[132]

3.3 Progress of pseudocapacitive electrodes based on nanoarchitectured current collectors

Great progress has been achieved in pseudocapacitive electrodes based on various types of nanoarchitectured current collectors in the past years. For the nanoarchitectured current collectors, the ones with nanowires/nanotubes/nanosheets/nanopores are designed with a general appeal. For the pseudocapacitive materials, MnO_2 is usually selected as a representative pseudocapacitive material owing to its high theoretical specific capacitance (1370 F g^{-1}), natural abundance, and low cost. However, due to the poor electrical conductivity and the slow proton and cation diffusivity of the bulk MnO_2, the pseudocapacitive reaction is restricted to take place only in a thin subsurface layer of bulk MnO_2, for instance, ca. 420 nm in thickness.[130] Therefore, MnO_2 has usually been selected as the model of pseudocapacitive materials to evaluate the performance of different nanoarchitectured current collectors. From the perspective of the electrochemical performance, some recently reported examples of MnO_2 electrodes based on nanoarrayed and nanoporous current collectors are analyzed below, respectively.

1D nanoarrays of metals are among the most common nanoarchitectured current collectors for PCs. For example, highly ordered Pt nanopillar arrays have been employed as a current collector (Figure 3-3a).[109] After electrodepositing a thin layer of MnO_2 onto Pt nanopillar arrays, the core@shell Pt@MnO_2 nanoelectrodes are obtained. The Pt@MnO_2 nanoelectrodes inherit the structural features from highly ordered Pt nanopillar arrays. Attributing to the high and accessible surface area for redox reactions and the large interspaces for ion migration and transportation, Pt@MnO_2 nanoelectrodes reveal a high gravimetric capacitance of 810 F g^{-1} at the scan rate of 5 mV s^{-1} and obtain a superior rate capability of 68% retention as the charging-discharging rate increasing from 2 to 100 A g^{-1} (Figure 3-3b-c). In comparison, the electrode based on a Pt planar-foil with similar MnO_2 mass loading exhibits a limited gravimetric capacitance when measuring at the same condition. Likewise, well ordered nanotube arrays

with high conductivity give another clue to buildup high-performance nanoelectrodes. In order to maximize the utilization rate of MnO_2, ordered nanotube arrays with high conductivity must provide reliable electrical connection while keep their tube morphology.[131] For that purpose, a MnO_2/Mn/MnO_2 sandwich-structured nanotube electrode (denoted as SNTAs) with a robust conductive core and bilateral symmetric MnO_2 shells is reported to serve as a promising candidate for heterogeneous electrode (Figure 3-3d). A maximum specific capacitance of 955 F g^{-1} at 1.5 A g^{-1} can be achieved for the MnO_2/Mn/MnO_2 SNTAs electrode. When current density increasing from 1.5 to 24 A g^{-1}, the SNTAs electrode exhibits a better rate capability of ~70 % capacitance retention than that of 47 % for NTAs electrode (Figure 3-3e-f), which is mainly due to the improved electrolytic accessible surface, reduced diffusion length of ions, as well as superior electrical conductivity endowed by the introduction of Mn NTAs skeleton. In addition to metallic current collectors, carbonaceous ones with properties of lightweight, excellent electronic conductivity, and flexible, etc., have also gained increasing concern and attention due to their application potential in electrochemical energy storage and conversion. Among them, graphene is undoubtedly emerging as one of the most promising building blocks for high-performance pseudocapacitive electrodes.[129, 133] Admittedly, it has been demonstrated that graphene nanosheet arrays are regarded as nanobridge for enhancing the electrochemical performance of pseudocapacitive materials.[134-135] For instance, the vertical aligned graphene arrays are fabricated as nanoarchitectured current collectors to address the issue of the low utilization of MnO_2.[132] The free-standing graphene nanosheets act as conductive frameworks to provide integrity and stability to overall nanoelectrodes (Figure 3-3g). Therefore, the graphene-MnO_2 nanoelectrodes show a high specific capacitance of 1176 F g^{-1} at 2 mV s^{-1}, much closer to the theoretical value of MnO_2 (Figure 3-3h-i), which is attributed to the higher conductivity of the graphene-MnO_2 nanoelectrodes. Given the fact that carbonaceous current collectors alone often serves as active materials to boost the charge storage performance in the form of electric

double-layer capacitance, the heterogeneous nanoelectrode combines the capacitive behavior with pseudocapacitive behavior to a certain degree to enhance the overall electrochemical property.

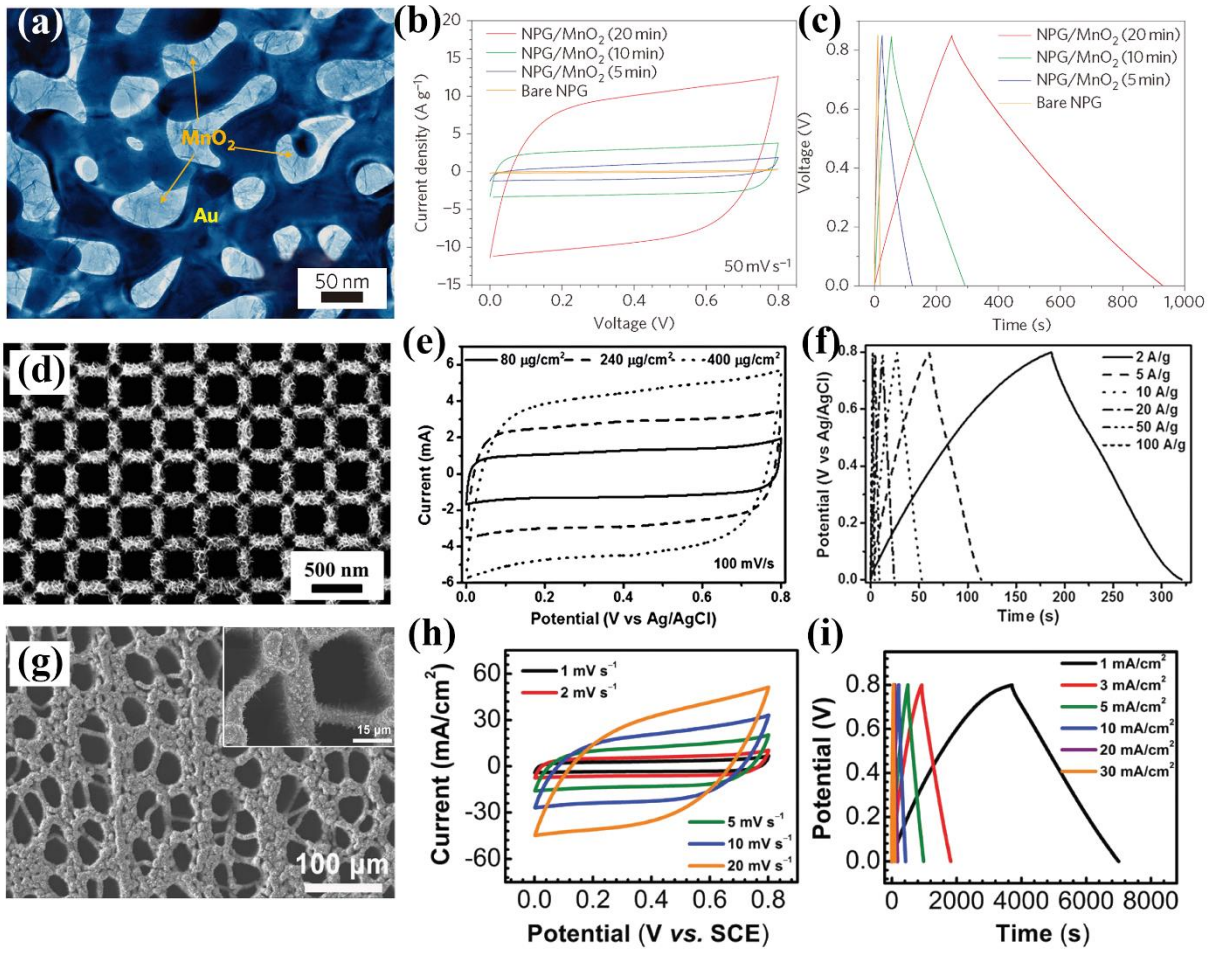

Figure 3-4 Representative examples of heterogeneous electrodes based on nanoporous current collectors. (a) TEM image and (b-c) the electrochemical performances of the nanoporous Au@MnO_2 electrodes.[85] (d) SEM image and (e-f) the electrochemical performances of nanoporous Ni@MnO_2 electrodes.[123] (g) SEM image and (h-i) the electrochemical performances of nanoporous WC@MnO_2 electrodes.[136]

Regarding current collectors based on nanoporous conductive materials, the 3D porous conductive network core provides short ion transport length and large specific surface area for the excellent rate performance of corresponding composite electrodes. A typical example here to prove this trend is the Au@MnO_2 electrode reported by Lang et al., which is fabricated by

electrodepositing MnO_2 layer on Au nanoporous scaffold.[85] The porous architecture of electrode is ascribed to its unique skeleton support, as shown in Figure 3-4a, with interconnected and cross-linked pores and numerous aperiodic Au ligaments. The role of nanoporous gold in this heterogeneous electrodes is highlighted, in which the nanoscale gold skeleton ensures a large gold/MnO_2 interface for boosting the electron transport of MnO_2, while the open pore channel provides sufficient contact between MnO_2 and the electrolyte. Thus the resultant 20 min MnO_2-plated electrode exhibits a maximum specific capacitance of 601 F g^{-1} at 0.3 A g^{-1} and still maintains 170 F g^{-1} at 20 A g^{-1} (Figure 3-4b-c). It is highly accepted that nanoarchitectured current collectors with high aspect ratio are regarded as excellent conductive frameworks for more pseudocapacitive materials conformal loading. However, the arrays with high aspect ratio usually suffer from the serious agglomeration of the nanowires, and finally lead to the reduced effective surface area as well as the reduction of mass loading of pseudocapacitive materials and limited accessibility of electrolyte. In order to tackle this, Ni nanoporous structure with robust structural mechanical stability can feasibly optimize the aspect-ratio without the fear of agglomeration (Figure 3-4d).[123] A high specific capacitance of 672 F g^{-1} at 2 mV s^{-1} can therefore be achieved for nanoporous Ni@MnO_2 electrode (Figure 3-4e). Besides, the negligible voltage *IR* drop in galvanostatic charge–discharge curves indicates the low internal resistance of electrode, largely attributed to the good electrical conductivity of the Ni nanoporous structure (Figure 3-4f). Apart from metallic porous nanocomposites for PCs, another major trend is carbonaceous porous skeleton in which pseudocapacitive materials are incorporated into its backbone. Most carbonaceous porous support have the merits of high conductive, eco-friendly and ease of design, such as the activated wood carbon (WC) scaffold with hierarchical porous structure developed by Hu's group.[136] Figure 3-4g depicts the morphology of WC@MnO_2 hybrid electrode, where the composite has numerous mesoporous and nanoporous structure co-existing straight channels

with the uniformly anchoring of MnO_2 nanosheets. The straight tunnels with low tortuosity are regarded to improve the ion diffusion rate and shorten ion-diffusion path-lengths of the overall bulk electrode. Hence, the WC@MnO_2 achieves a high specific capacitance of 4155 mF cm^{-2} at 1 mA cm^{-2}, and still maintains 1811 mF cm^{-2} when the current density increasing to 30 mA cm^{-2}, inferring a good rate performance (Figure 3-4h-i). This study gives us a new clue to boost the capacitance and energy/power density for PCs, which largely depends on the electrode structure design and engineering, especially for its optimized design of current collector skeleton at the circumstance of high mass loading or thick electrodes.

As can be seen from the above mentioned examples, the utilization of nanoarchitectured current collectors can significantly address the challenge of the poor electronic conductivity of MnO_2, thus access the full theoretical capacitance and achieve high rate capability. Although the capacitance contribution from the nanoarchitectured current collector is quite small comparing to the higher capacitance of the adopted pseudocapacitive materials, a significant improvement of the charge storage ability would be achieved resulting from the constructive synergistic effects between the nanoarchitectured current collectors and the pseudocapacitive materials. Therefore, the benefits of nanoarchitectured current collector toward enhancing electrochemical performance are worthy of concern and systematic summary.

3.4 The merits of nanoarchitectured current collectors in pseudocapacitive electrodes

Table 3-1 Summary of some pseudocapacitive electrodes based on the nanoarchitectured current collectors and their corresponding charge storage performances.

Current collectors (core)	Fabrication method for current collectors	Pseudocapacitive materials (shell)	Capacitance	Rate capability	Electrode impedance (R_s[a] and R_{ct}[b])	Cyclic stability	Ref
1D/2D nanoarrayed current collector based electrodes							
Pt nanotube arrays	PAM template	MnO_2 nanosheet	793 F g^{-1} at 2 A g^{-1}	68% retention from 2 to 100 A g^{-1}	-	~100% retention for 8000 cycles	[109]

Ni nanorod arrays	PAM template	MnO_2 nano-film (0.54 mg cm^{-2})	108 mF cm^{-2} at 2 mA cm^{-2}	61% retention from 2 to 20 mA cm^{-2}	R_{ct} = 3.25 Ω	90% retention for 5000 cycles	106
Ni nanotube arrays	ZnO template	Al-Co-S nanolayer (1.5 mg cm^{-2})	2434 F g^{-1} at 1 A g^{-1}	72% retention from 1 to 100 A g^{-1}	R_s = 0.85 Ω	90.6% retention for 10 000 cycles	137
Ni nanotube arrays	ZnO template	Fe_2O_3 nanoneedles	~350 F g^{-1} at 4 m A g^{-1}	62% retention from 4 to 64 m A g^{-1}	R_s = 2.3 Ω R_{ct} = 2.3 Ω	92.3% retention for 5 000 cycles	138
Carbon tube arrays	ZnO template	MOF-derived N-doped Carbon Bubbles (0.2-1.5 mg cm^{-2})	580 mF cm^{-2} at 1 mA cm^{-2}	57% retention from 1 to 200 mA cm^{-2}	R_s < 1 Ω	98.5% retention for 1 0000 cycles	139
Ni nanotube arrays	ZnO template	perchlorate-doped PPy nanolayer	474.4 F g^{-1} at 5 mV s^{-1}	79% retention from 5 to 100 mV s^{-1}	R_s = 1.36 Ω, R_{ct} = 2.44 Ω	75.3% retention for 1 0000 cycles	140
Ni-Co nanotube arrays	ZnO template	Ni-Co layered double hydroxide (0.87–0.91 mg cm^{-2})	2414 F g^{-1} at 1 A g^{-1}	82% retention from 1 to 20 A g^{-1}	R_s = 1.19 Ω	98.8% retention for 5 000 cycles	141
ZnO nanorod arrays	Seed-assisted HT[c]	α-Fe_2O_3 nanolayer (0.035-0.04 mg cm^{-2})	491.7 F g^{-1} at 10 mV s^{-1}	66% retention from 10 to 400 mV s^{-1}	R_s = ~2.8 Ω	~99% retention for 2 000 cycles	54
ZnO nanowire arrays	Seed-assisted HT	Ni-NiO nanolayer	~2440 F g^{-1} at 10 mV s^{-1}	64% retention from 10 to 100 mV s^{-1}	-	86.7% retention for 750 cycles	55
Ni-Co-S nanosheet arrays	Two-step HT	Ni-W-O nanolayer	1988 F·g^{-1} at 2 A·g^{-1}	75% retention from 2 to 30 A g^{-1}	R_s < 0.5 Ω	91.7% retention for 6000 cycles	57
$CoNi_2S_4$ nanosheet arrays	Two-step HT	Ni_3S_2 nanoparticles (0.8 mg cm^{-2})	2435 F g^{-1} at 2 A g^{-1}	80% retention from 2 to 20 A g^{-1}	R_s < 0.3 Ω R_{ct} = ~0.5 Ω	92.8% retention for 6000 cycles	58
TiO_2 nanotube arrays	EA	$Mo_xW_{1-x}O_3$ oxides nanolayer (0.4 mg cm^{-2})	517.4 F g^{-1} at 1 A g^{-1}	89% retention from 1 to 10 A g^{-1}	R_s = 1.089 Ω, R_{ct} = ~0 Ω	103.0% retention for 5000 cycles	68
H_2-TiO_2 nanotube arrays	EA and hydrogenation	RuO_2 nanoparticle (0.048 mg cm^{-2})	1297 F g^{-1} at 40 mV s^{-1}	92% retention from 40 to 1000 mV s^{-1}	-	97.3% retention for 5000 cycles	142
S-doped TiO_2 nanotube arrays	EA and sulfidation	PANI nanolayer (7.5 μg cm^{-1})	91.9 F cm^{-2} at 0.01 mA cm^{-2}	32% retention from 0.01 to 2 mA cm^{-2}	R_{ct} = 65.7 Ω	93.8% retention for 12000 cycles	143
N-doped TiO_2 nanotubes arrays	EA and nitridation	nanocrystalline Nb_2O_5	37 mF cm^{-2} at 1 mV s^{-1}	24% retention from 1 to 200 mV s^{-1}	R_{ct} = ~0 Ω	-	69

Modified TiO_2 nanotubes arrays	EA and carbon/oxygen vacancies modify	$Co_{0.12}Ni_{1.88}S_2$@Co_8S_9 nanoparticles (0.04-0.11 mg cm^{-2})	680.1 C g^{-1} at 2 A g^{-1}	79% retention from 2 to 20 A g^{-1}	-	85.7% retention for 3000 cycles	72
Ni ultra-long nanowire arrays	Magnetic-field-driven deposition	MnO_2 nanolayer (3.51 mg cm^{-2})	750 mF cm^{-2} at 1 mV s^{-1}	-	R_s = 12.3 Ω, R_{ct} = 3.76 Ω	103.7% retention for 20000 cycles	144
Graphene nanosheet arrays	PECVD	MnO_2 nanoparticle (1.3 mg cm^{-2})	1176 F g^{-1} at 2 mV s^{-1}	42% retention from 2 to 50 mV s^{-1}	R_s = 5 Ω	98.1% retention for 10000 cycles	132
Carbon nanowall arrays	PECVD	RuO_2 microlayer	1094 mF cm^{-2} at 2 mVs^{-1}	-	R_s = 8 Ω cm^{-2}	~90% retention for 2000 cycles	145
Vertically aligned graphene nanosheets	PECVD	Co_3O_4 nanoparticles	3482 F g^{-1} at 1 mV s^{-1}	46% retention from 1 to 200 mV s^{-1}	R_{ct} = 20.66 Ω	86.2% retention for 20 000 cycles	146
ZnO nanoforest arrays	CVD	ZnS naolayer	217 mF cm^{-2} at 1 mA cm^{-2}	-	-	82% retention for 2000 cycles	76
Carbonized porous silicon nanowires	CE[e], CVD	MnO_x nanoparticles (0.42 ± 0.04 mg cm^{-2})	381 mF cm^{-2} at 12.5 mA cm^{-2}	26% retention from 12.5 to 100 mA cm^{-2}	R_s = 58 Ω; R_{ct} = 23 Ω	~80% retention for 10000 cycles	75
Si nanowire arrays	CE	H_2-VO_x nanorod branches (1.12 μg cm^{-2})	950 F g^{-1} at 0.5 A g^{-1}	76% retention from 0.5 to 20 A g^{-1}	R_{ct} = ~6 Ω	~91.1% retention for 10000 cycles	63
3D nanoporous current collector based electrodes							
Aligned inverse-opal Ni structures	CCT and ED	MnO_2 nanolayer (45 μg cm^{-2})	38.2 mF cm^{-2} at 10 mV s^{-1}	72% retention from 10 to 200 mV s^{-1}	R_{ct} < 10 Ω	87.7% retention for 5000 cycles	147
Ordered macroporous Ni inverse opals structure	CCT and ED	Cu_2O nanolayer	502 F g^{-1} at 10 mV s^{-1}	85.4% retention from 10 to 500 mV s^{-1}	R_s = ~2 Ω	92% retention for 500 cycles	121
Macroporous graphene frameworks	CCT and vacuum infiltration	MnO_2 nanolayer	389 F g^{-1} at 1 A g^{-1}	97.7% retention from 1 to 35 A g^{-1}	R_{ct} = 3.4 Ω	95% retention for 4000 cycles	118
Ni nanopore network	Two-step replication PAM	MnO_2 nanolayer (80-400μg cm^{-2})	382 F g^{-1} at 2 mV s^{-1}	-	R_{ct} < 1 Ω	83% retention for 3000 cycles	123
3D FTO nanopore structure	PAM and ultrasonic spray pyrolysis	MnO_2 nanolayer (0.15-0.3 mg cm^{-2})	193.8 mF cm^{-2} at 5 mV s^{-1}	-	-	81.6% retention for 3000 cycles	148
Porous graphite foams	Porous Ni template CVD	Co_3O_4/PEDOT-MnO_2 core/shell nanowire arrays	~400 F g^{-1} at 5 A g^{-1}	88% retention from 5 to 40 A g^{-1}	R_s < 1 Ω R_{ct} < 1 Ω	90% retention for 20000 cycles	149

3D graphene foam	Ni foam template CVD	novel honeycomb-like $CoMoO_4$ nanolayer (0.51 mg cm^{-2})	2741 F g^{-1} at 1.43 A g^{-1}	77% retention from 1.43 to 5 A g^{-1}	R_s < 1 Ω R_{ct} < 1 Ω	96.36% retention for 10000 cycles	128
3D ultrathin-graphite foam	Ni foam template CVD	nanoporous $Ni(OH)_2$ thin film (0.2 mg cm^{-2})	166 F g^{-1} at 0.5 A g^{-1}	67% retention from 0.5 to 10 A g^{-1}	R_s =1.3 Ω	65% retention for 1000 cycles	126
Graphene foam/CNT hybrid substrate	Ni foam template CVD, HT and CVD	MnO_2 nanolayer (0.1-0.8 mg cm^{-2})	215 F g^{-1} at 10 mV s^{-1}	49% retention from 10 to 100 mV s^{-1}	R_s = 7.4 Ω R_{ct} = 5.6 Ω	>90% retention for 5000 cycles	150
Ni foam@rGO	HT	H-Fe_2O_3 nanoparticles (0.49 mg cm^{-2})	37.88 mF cm^{-2} at 1 V s^{-1}	54% retention from 1 to 20 V s^{-1}	R_s = 0.7 Ω	97% retention for 10000 cycles	151
3D graphene aerogels-based mesoporous carbons	HT and silica template	RuO_2 crystalline nanoparticles	560 F g^{-1} at 5 mV s^{-1}	62% retention from 5 to 100 mV s^{-1}	-	-	152
Nanoporous Au substrate	dealloying	MnO_2 nanolayer (0.2 mg cm^{-2})	702 F g^{-1} at 0.25 A g^{-1}	50% retention from 0.25 to 20 A g^{-1}	R_s = 14.57 Ω	~97.1% retention for 3000 cycles	84-85
NiCo-based nanoporous substrate	dealloying	NiCo oxide composites nanolayer	1.22 F cm^{-2} at 6 mA cm^{-2}	-	R_s = 8.4 Ω cm^{-2}	-	153
Nanoporous NiCu alloy substrate	dealloying	vertically aligned $Ni(OH)_2/Cu_2O$ nanosheets	8234 mC cm^{-2} at 20 mA cm^{-2}	40% retention from 20 to 200 mA cm^{-2}	Rs < 1 Ω R_{ct} = ~1.2 Ω	112.8% retention for 10000 cycles	154
Porous gold substrate	HBDT	RuO_2 nanolayer	3250 mF cm^{-2} at 0.1 mV s^{-1}	-	R_s = 1.83 Ω cm^{-2}	95% retention for 2000 cycles	90
Nanoporous Ni layer	HBDT	$MnCo_2O_4$ nanothorns (0.75 mg cm^{-2})	1798 mF cm^{-2} at 2 mA cm^{-2}	58% retention from 2 to 20 mA cm^{-2}	R_s = 1.4 Ω	93.7% retention for 5000 cycles	91
Hierarchical Ni structure	HBDT	$Co(OH)_2$ nanosheets (0.025 - 1 mg cm^{-2})	3.17 F cm^{-2} at 5 mA cm^{-2}	90% retention from 5 to 30 mA cm^{-2}	R_s = 0.88 Ω	~100% retention for 2000 cycles	92
Nanoporous Ni layer	HBDT	$NiCo_2S_4$ nanosheet	~100 mF cm at 0.2 mA cm^{-1}	70% retention from 0.2 to 20 mA cm^{-1}	R_s = 0.55 Ω	92% retention for 1000 cycles	93
Carbon coated 3D-porous Cu structures	HBDT and pyrolyzing glucose	$Ni(OH)_2$ nanolayer (0.35 mg cm^{-2})	1860 F g^{-1} at 1 A g^{-1}	86% retention from 1 to 50 A g^{-1}	R_s = 0.65 Ω R_{ct} < 1 Ω	86.5% retention for 10000 cycles	94
Nanoporous Ni substrate	HBDT	MnO_x nanolayer (1.65 mg cm^{-2})	0.462 F cm^{-2} at 5 mA cm^{-2}	51% retention from 5 to 200 mA cm^{-2}	R_s = 5.72 Ω R_{ct} = 0.44 Ω	98.91% retention for 2000 cycles	95

Nanoporous Ag framework	Electroreduction	Fe_2O_3 nanoparticles (0.45-1.8 mg cm^{-2})	608 F g^{-1} at 10 A g^{-1}	86% retention from 10 to 200 mV s^{-1}	R_s < 3 Ω	84.9% retention for 6000 cycles	96
Ni nanofoams	Refluxing and hydrogen reduction	$NiCo_2O_4$ nanosheets (1.54 mg cm^{-2})	899 F g^{-1} at 1 A g^{-1}	68% retention from 1 to 20 A g^{-1}	-	93.2% retention for 6000 cycles	97
Nanoporous CoNi alloy structure	ED and hydrogen reduction	Au-MnO_x nanolayer	765 F cm^{-3} at 1 A cm^{-3}	70% retention from 1 to 50 A cm^{-3}	R_s = 0.55 Ω R_{ct} = 0.8 Ω	94.1% retention for 20000 cycles	98
3D hierarchical Cu architecture on fiber framework	Magnetron sputtering	Cu_2O nanolayer (0.26 mg cm^{-2})	238 mF cm^{-2} at 1 mA cm^{-2}	54% retention from 1 to 32 mA cm^{-2}	R_s = 4.5 Ω	91.7% retention for 10000 cycles	155
Porous rGO	HT	Ni-Co-S nanosheet (1.5 ± 0.1 mg cm^{-2})	2526 F g^{-1} at 2 A g^{-1}	76% retention from 2 to 10 A g^{-1}	R_s < 1 Ω R_{ct} < 1 Ω	77% retention for 2000 cycles	156
3D porous graphene network	Laser scribing	MnO_2 nanolayer	1136.5 F cm^{-3} at 1 mV s^{-1}	-	R_s = ~1.5 Ω cm^{-2}	96% retention for 10000 cycles	157
Porous wood carbon network	Biomass conversion	MnO_2 nanolayer (~75 mg cm^{-2})	55.4 F g^{-1} at 1 A g^{-1}	44% retention from 1 to 30 A g^{-1}	-	93% retention for 10000 cycles	136

[a]R_s − equivalent series resistance; [b]R_{ct} − charge transfer resistance; [c]HT – hydrothermal; [d]EA − electrochemical anodization; [e]CE − chemical etching; [f]CCT − colloidal crystal template; [g]ED – electrodeposition.

Table 3-1 summarizes the reported pseudocapacitive electrodes consisting of the nanoarchitectured current collectors and pseudocapacitive materials, including the fabrication strategies, the morphologies of nanoarchitectured current collectors, the type of pseudocapacitive materials, as well as the electrochemical performance of these electrodes in terms of capacitance, rate capability, impedance properties, and cycling stability. Accordingly, the strength of nanoarchitectured current collectors in PCs is outlined below:

(i) Supporting pseudocapacitive materials to synergistically boost capacitance with enhanced electrolytic accessible surface. Nanoarchitectured current collectors have a much larger surface area than the planar bulky ones. This will allow to drastically increase the amount of pseudocapacitive materials, thus directly improving the capacitance density per unit area. On the other hand, the pseudocapacitive materials remain separated by nanoarchitectured current

collectors and are free from agglomeration, which will fully expose more surface area of the pseudocapacitive materials for participating in efficient redox reaction. By this point, nanoarchitectured current collectors give full play to pseudocapacitive materials and thus improving the energy storage performance of the PCs. In the most cases, especially for some nanoarchitectured current collectors made from carbonaceous, polymers, and metal oxides, sulfides, or nitrides, they also involve in part of the charge storage process apart from their function of charge transportation, either through Faradaic or non-Faradaic reactions. Thus it will directly facilitate boosting capacitance of PC electrodes, though the proportion of this part contribution is not as large as that of the deposited pseudocapacitive materials. Furthermore, the synergistic effect of nanoarchitectured current collector and pseudocapacitive materials simultaneously achieves both the "capacitor-like" rate capability and "battery-like" performance, finally resulting in a high energy and power density.[44]

(ii) Facilitating the ion diffusion in the electrolyte to achieve a high rate capability. In addition to the redox reactions in the electrode that are mainly dependent on the pseudocapacitive materials, there are three primary resistances existing during the charge and discharge in PCs: ion diffusion in the electrolyte, ion transport in electrolyte and electron migration in both the electrode and current collector. Current collectors fabricated in 1D/2D nanoarrays or 3D nanoporous architectures (Figure 2-3c-d) are superior to conventional metallic foils/foams on these following aspects. The open space inside the heterogeneous electrode based on nanoarchitectured current collectors eases the path for electrolyte diffusion during the electrochemical measurements to shorten diffusion length. Pseudocapacitive materials with thickness of a few tens to hundreds of nanometers inherit the morphologies of nanoarchitectured current collectors that are consisted of nanosized subunits, largely reducing the time constant for ion diffusion. The smaller diffusion length and shorter time constant will ensure a faster charge-discharge rate for PCs.

(iii) Effective ionic and electronic transportation significantly lower the interfacial resistance. Arrayed or porous pseudocapacitive nanoelectrode shared the topography of nanoarchitectured current collector offers the interconnected and unimpeded channels for efficient ion transport. Besides, the electrode configuration avoids the addition of polymeric binders which reduces the internal resistance and eliminates the invalid dead volume in the electrode. As a result, the large surface area of electrode architecture guarantees a highly efficient pathway for electron migration and ion transport during the charge/discharge processes, and therefore simultaneously improves the ionic current and electronic current within the electrode (Figure 2-3c-d). The charge and ion transport efficiencies at both interfaces of current collectors/pseudocapacitive materials and pseudocapacitive materials/electrolyte are improved. Nevertheless, nanoarchitectured current collectors in electrodes also have the following weaknesses that should not be overlooked: (i) Nanoarchitectured current collectors severely suffer from the low mass loading of pseudocapacitive materials. (ii) Nanoarchitectured current collectors in electrodes usually endure unreliable mechanical stability when electrodes were assembled into the devices. (iii) Nanoarchitectured current collectors with the 1D configuration have limited aspect ratio, since they tend to agglomerate to lower the overall surface energy.

4 Experiments and instrumentations

4.1 Fabrication of free-standing Ni nanorod arrays as nanoarchitectured current collector

Free-standing Ni nanorod arrays were fabricated by PAM template-assisted electrochemical deposition. Specifically, the anodization of the nano-imprinted Al foil was conducted at voltage of 160 V in 0.4 M H_3PO_4 solution under 15 °C for 15 min. Afterward, Ti (10 nm) and Au (20 nm) were subsequently evaporated onto the surface of PAM template by PVD technique. Following, a thick Ni layer (~7 μm) was electrochemically deposited with Ti/Au as working electrode in a Ni electroplating solution containing 0.38 M $NiSO_4 \cdot 6H_2O$, 0.12 M $NiCl_2 \cdot 6H_2O$, and 0.5 M H_3BO_3. The backside of Al was removed by using a mixture etchant solution of $CuCl_2$ (85 wt%) and HCl (15 wt%), and then was soaked into H_3PO_4 solution (5 wt%) at 60 °C to remove the barrier layer. Ni nanorod arrays were prepared by electrodepositing into PAM template with a current density of −2 mA cm^{-2} for 4 min. Finally, the PAM template was dissolved by 5 wt% H_3PO_4 solution to obtain free-standing Ni nanorod arrays. For comparison, Ni planar foil was also fabricated without the introduction of PAM template and followed the same procedure and condition as above described.

4.2 Preparation of highly-etched porous alumina membrane@SnO_2 (EPAM@SnO_2) as nanoarchitectured current collector

Preparation of highly-etched porous alumina membrane (EPAM) skeleton. The EPAM on a conductive substrate was fabricated by an anodization process and a subsequent electrodeposition process as well as a precise chemical-etching process. The preparation steps of EPAM skeleton are similar to that of PAM template with Ni substrate as described above. The difference is that the anodization time was set 15-90 min this time, and the wet-etching period was further prolonged in order to widen the pore-size of nanochannels. Through prolonging the etching time, the PAM gradually turned into the honeycomb-like EPAM architecture.

Preparation of EPAM@SnO_2 nanoarchitectured current collector. In order to turn the insulated EPAM scaffold to the conductive nanostructure, a thin layer of well-conductive SnO_2 was conformally deposited on the EPAM. Specifically, the EPAM@SnO_2 electrodes were obtained through conformally depositing SnO_2 on the surface of the as-prepared EPAM, using a SUNALE R-150 ALD system (PicoSun, Finland). $SnCl_4$ and H_2O were chosen as the precursors of Sn and O, respectively, and nitrogen was the carrier gas and purge gas. Specifically, $SnCl_4$ was pulsed for 0.2 s and purged for 4 s, followed by a 1 s pulse and an 8 s purge of H_2O and this procedure was cycled for 1500 times. The precipitation of SnO_2 was realized according to the technical flow process shown in Figure 4-1. The temperature of reaction chamber was kept at 250 °C during the deposition process. The growth rate of SnO_2 is about 0.1 Å per cycle. Here, the electrochemical performance of the resultant EPAM@SnO_2 was firstly evaluated, before serving it as a nanoarchitectured current collector for the pseudocapacitive electrodes in micro-supercapacitors.

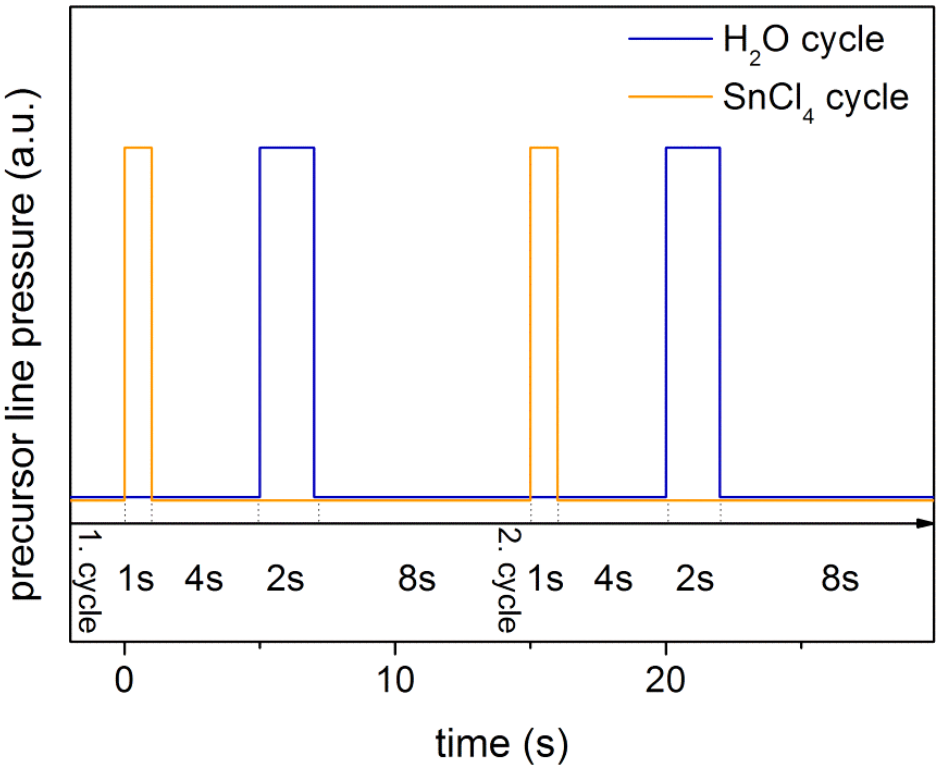

Figure 4-1 ALD process for the fabrication of SnO_2 from the $SnCl_4$ and H_2O precursors, depicting two typical deposition cycles with required pulse and purge time.

4.3 Preparation of Ni nanowires (NiNWs)-EPAM as nanoarchitectured current collector

NiNWs with 10 μm in length were grown inside the nanochannels of PAM template by electrochemical deposition process under the current density of −2 mA cm^{-2} for 1 h. The obtained NiNWs-PAM was converted to NiNWs-EPAM after being etched in H_3PO_4 solution (5 wt%, 60 °C) for 15 min. For comparison, the NiNWs counterpart was prepared at the same conditions except that the PAM template in the scaffold was completely etched away.

4.4 Preparation of pseudocapacitive electrodes

With the as-obtained nanoarchitectured current collectors as the working electrodes, the pseudocapacitive electrodes were fabricated through the electrochemical deposition method. Herein, MnO_2 and PPy were selected as the examples of pseudocapacitive materials to construct pesudocapacitive electrodes based on the as-prepared nanoarchitectured current collectors.

MnO_2 layers were deposited onto the as-prepared Ni planar foil (NF), Ni nanorod arrays (NN), EPAM@SnO_2, NiNWs, and NiNWs-EPAM scaffolds by using galvanostatic electrochemical deposition method with a constant current density of 1 mA cm^{-2}. The MnO_2 plating electrolyte comprised of 50 mM manganese acetate ($Mn(Ac)_2$) and 100 mM sodium acetate ($Na(Ac)_2$). After deposition, the obtained NF@MnO_2, NN@MnO_2, EPAM@SnO_2@MnO_2, NiNWs@MnO_2 and NiNWs@MnO_2-EPAM were cleaned with deionized water and dried.

Likewise, PPy films were coated onto the EPAM@SnO_2, NiNWs, and NiNWs-EPAM scaffolds through the electrochemical polymerization of pyrrole (Py) process. The plating solution consisted of 0.1 M pyrrole monomer (98%) and 0.2 M oxalic acid, and the applied potential was 0.8 V (*vs.* Ag/AgCl). The obtained EPAM@SnO_2@PPy, NiNWs@PPy and NiNWs@PPy-EPAM were rinsed with deionized water and dried.

For the determination of the mass loading of pseudocapacitive materials, a 100 % charge efficiency is assumed. The active mass of the electrodes is determined according to Faraday's law:

$$m = \frac{QM}{zF}$$

where Q is the charge passed during the electrochemical deposition process of pseudocapacitive materials (*i.e.*, MnO_2, PPy). M is the molar mass of the active electrode material (M_{MnO2} = 86.9 g mol^{-1}, M_{py} = 65.09 g mol^{-1}), F is the Faraday constant and z is the number of transferred electrons per active electrode atom (z = 2 for MnO_2 and PPy deposition). Table 4-1 outlines the mass loadings of MnO_2 or PPy in the pseudocapacitive electrodes.

Table 4-1 Mass loadings of the MnO_2 or PPy in the pseudocapacitive electrodes.

Pseudocapacitive electrodes	m_{MnO2} (mg cm^{-2})	m_{PPy} (mg cm^{-2})
NF@MnO_2	0.054-0.54	–
NN@MnO_2	0.054-3.2	–
EPAM@SnO_2@MnO_2	0.11-0.65	–
NiNWs@MnO_2	~0.43	–
NiNWs@MnO_2-EPAM	~0.43	–
EPAM@SnO_2@PPy	–	0.21-1.32
NiNWs@PPy	–	~0.8
NiNWs@PPy-EPAM	–	~0.8

4.5 Analysis instrument

4.5.1 Field emission scanning electron microscopy

Field emission scanning electron microscopy (Auriga Zeiss FIB) is employed to study the morphology and structure of the nanoelectrodes. As a source of electrons, SEM uses electromagnetic gun as a field emission gun that provides extremely focused high and low-energy electron beams, which greatly improves spatial resolution and enables work to be carried out at very low potentials (0.02–5 kV). This helps to minimize the charging effect on non-conductive specimens and to avoid damage to electron beam sensitive samples. It is not possible to have a sharp picture at this low potential using the conventional SEM. Another features of the SEM are the in-lens detectors it used inside. These detectors, which are optimized to work

at high resolution and very low acceleration potential, are crucial for getting the maximum performance. In SEM, two types of electrons are primarily detected: backscattered electrons (BSE) and secondary electrons (SE). Backscattered electrons are reflected back after elastic interactions between the beam and the specimen. Secondary electrons, however, originate from the atoms of the sample when their electrons become excited and have sufficient energy to escape the sample surface. The secondary electron image has good resolution and provides more detail in terms of understanding surface morphology. Therefore, secondary electron imaging, being more surface sensitive, has greater resolution. However, backscattered electrons have the advantage that they are sensitive to the atomic mass of the nuclei they scatter from. As a result, heavier elements backscatter more efficiently appear brighter than lighter elements in a backscattered electron image.

4.5.2 Energy dispersive X-ray Detector

Energy dispersive X-ray (EDX, EDAX) detector is a surface analytical technique used for the elemental analysis or chemical characterization of a sample. The technique detects x-rays emitted from the sample during bombardment by an electron beam to characterize the elemental composition of the as-prepared samples. When the sample is bombarded by the SEM's electron beam, electrons are ejected from the atoms comprising the sample's surface. The resulting electron vacancies are filled by electrons from a higher state, and an x-ray is emitted to balance the energy difference between the two electrons' states. The x-ray energy is characteristic of the element from which it was emitted.

4.6 Assembly of the supercapacitors

Symmetric SCs were assembled based on two identical electrodes, and asymmetric SCs were assembled from two different positive (MnO_2-) and negative (PPy-) electrodes. In order to get the charge balance ($q^+ = q^-$) for the asymmetric device, the mass balancing should follow:

$$\frac{m_+}{m_-} = \frac{C_- \times \Delta V_-}{C_+ \times \Delta V_+}$$

with (m_+/m_-) being the ideal ratio of positive to negative active electrode materials, $C_{-/+}$ being the specific capacitance of the respective electrode material, and $\Delta V_{-/+}$ being the respective operating potential (0.8 V for negative and 0.8 V for positive electrode).

Two kinds of electrolytes were utilized in the electrochemical systems, including aqueous and ionic liquid ones: 1.0 M Na_2SO_4 aqueous electrolyte and ionic liquid electrolyte of 1-ethyl-3-methylimidazolium bis(trifluoromethylsulfonyl)imide (EMIM-TFSI, 1.0 M in acetonitrile solution (ACN)). The positive and negative electrodes (ca. 0.8 cm in diameter) were separated by a porous glass microfiber (Whatman, GF B/55) as separator and assembled into a Swagelok type cell (Figure 4-2), which were investigated in two-electrode configurations. Moreover, the NN@MnO_2 and NF@MnO_2 electrodes were also evaluated in a three-electrode configuration with platinum foil as the counter electrode and Ag/AgCl as the reference electrode in an electrolyte of 1.0 M Na_2SO_4 aqueous solution.

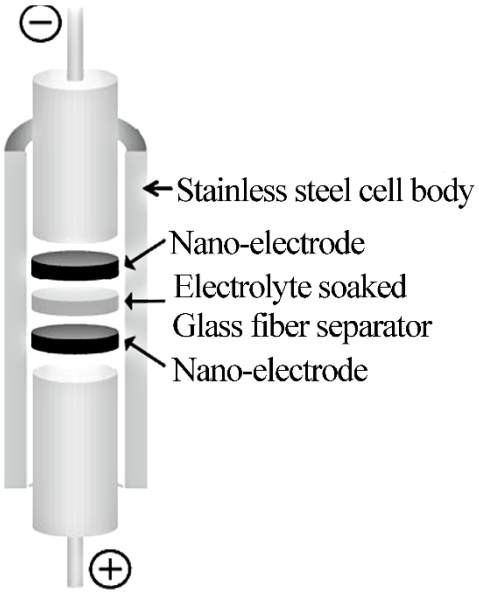

Figure 4-2 Swagelok type two-electrode measurement setup.

4.7 Electrochemical analysis

The electrochemical performance of assembled SC devices were investigated on a Potentiostat (BioLogic, VSP) and focused mainly on these following methods: (1) cyclic voltammogram (CV) method, (2) galvanostatic charge and discharge (GCD) measurement, (3) electrochemical impedance spectroscopy (EIS) measurement (Nyquist and Bode plots), and (4) Ragone plot.

(1) *CV method.* CV method is the most intuitive approach to analyze the electrochemical behavior. In our research system, the CV curves were collected with various scan rates. The device capacitance C_{CV} (mF cm^{-2}) at certain scan rate can be calculated from CV curves based on the equation:

$$C_{cv} = \frac{\int IdV}{\nu \times \Delta V \times A}$$

where I (mA) is the response current, ν (V s^{-1}) is the potential scan rate, A (cm^2) is total footprint area of device and ΔV (V) is the voltage window.

(2) *GCD profile.* A GCD profile can measure the capacitance and voltage *IR* drop of the electrode at a given discharge current. The capacitance of the device C_{GCD} (mF cm^{-2}) is determined from the GCD profiles based on the equation:

$$C_{GCD} = \frac{I \times \Delta t}{A \times \Delta V}$$

where Δt (s) is the discharge time and I (mA) is the discharge current.

At a higher current rate, the total impedance of the cell gives rise to an initial drop of the discharge voltage, which remains until the constant capacitive performance is reached. The low capacity values observed at higher current rates are associated with *IR* drop within the SC devices. The internal resistance of the devices can be calculated for each cell configuration using the *IR* drop.

(3) *EIS measurement.* EIS spectrum is to assess the overall function of electrode from the resistance and reaction kinetics aspects. The EIS measurement was conducted at the open circuit potential with frequency ranging from 100 MHz to 10 mHz at a 5 mV amplitude.

The relaxation time constant (τ_0) can be calculated by

$$\tau_0 = \frac{1}{f_0}$$

here the f_0 is the corresponding frequency (f_0) at the −45° phase angle in Bode plot.

(4) *Ragone plot.* Ragone plot represents the dependence of achieved area energy density versus area power density, the latter being determined by the rates at which discharging of a device are conducted. Specifically, the energy density E and power density P are determined by the following equations:

$$E = \frac{1}{2} C \Delta V^2$$

$$P = \frac{E}{\Delta t}$$

where $\Delta V = V_{max} - V_{drop}$ is the operational potential window (V_{max} is the maximum voltage, V_{drop} is voltage drop at the beginning of discharge).

5 Results and discussion

In this chapter, three kinds of nanoarchitectured current collectors, *i.e.*, Ni nanorod arrays, EPAM@SnO_2 scaffolds, and NiNWs-EPAM platforms, were designed to construct pseudocapacitive electrodes, respectively. Among them, Ni nanorod arrays are evaluated in the conventional thick-layer electrodes, and the rest two are to construct nanoelectrodes, which are investigated in micro-supercapacitors (MSCs).

5.1 Evaluating the role of nanoarchitectured current collectors in energy storage capability of supercapacitors electrodes with thick pseudocapacitive materials layers

With the ever-increasing demand for high amount of area-normalized capacitance and energy for SCs, much efforts have been focused on either developing new pseudocapacitive materials, or optimizing the structure of pseudocapacitive electrodes. In this context, alternative to the pursuit of new pseudocapacitive materials with higher performance, development of pseudocapacitive electrode with much higher mass loading of pseudocapacitive materials will become universal strategy for practical applications.[158] Unfortunately, to the best of our knowledge, there is a lack of research concerning nanoarchitectured current collectors for producing conventional SCs electrodes with a thick layer of pseudocapacitive materials.

5.1.1 The Ni nanorod@MnO_2 (NN@MnO_2) electrode with thick pseudocapacitive materials layer

The fabrication process of NN@MnO_2 electrode with MnO_2 layer in different thickness is schematically illustrated in Figure 5-1. Free-standing Ni nanorod arrays were firstly fabricated by using PAM template assisted electrochemical deposition.[159-160] Subsequently, MnO_2 in the form of either conformal coating or thick layer was electrochemically deposited onto Ni nanorods through controlling the electroplating time.

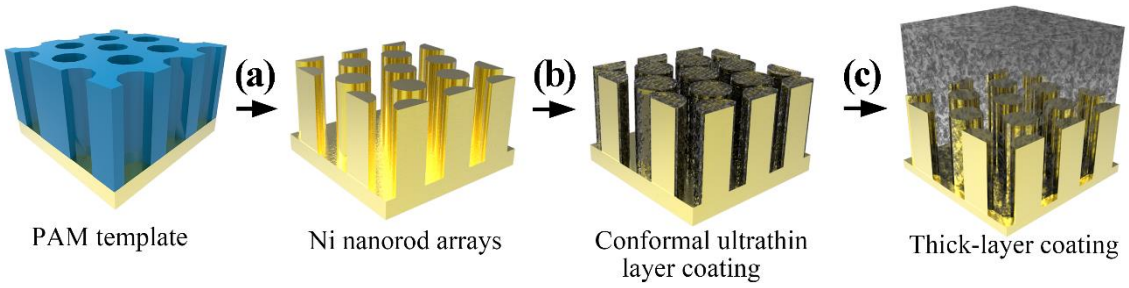

Figure 5-1 Schematic illustration of the fabrication process for the NN@MnO_2 electrodes. (a) PAM template-assisted fabrication of Ni nanorod arrays as nanoarchitectured current collectors; (b) ultrathin MnO_2 layer conformally coated on Ni nanorods by electrochemical deposition; (c) thick-layer MnO_2 coated on Ni nanorods by extending the electrochemical deposition time.

5.1.2 The morphology characterization of the NN@MnO_2 and Ni foil@MnO_2 (NF@MnO_2) electrodes

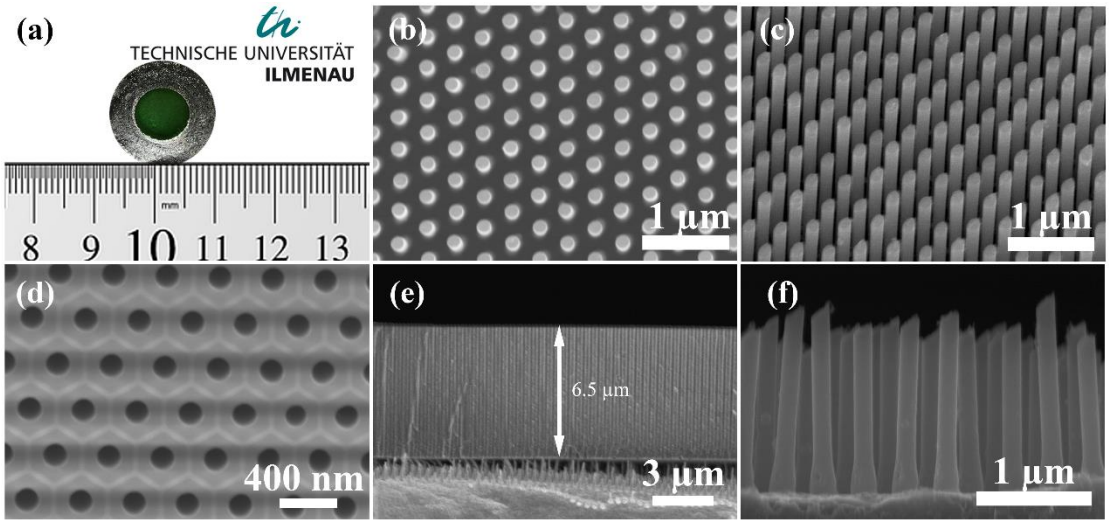

Figure 5-2 (a) The optical photograph image and (b) top- and (c) tilted-view SEM images of the bare Ni nanorod arrays, (d) the top- and (e) cross-sectional view SEM images of the PAM template and (f) cross-sectional view SEM image of the bare Ni nanorod arrays.

The optical photograph displayed in Figure 5-2a shows that the footprint area of the well-prepared Ni nanorod arrays is 0.5 cm^2. The representative top- and tilted-view SEM images clearly reveal the highly ordered and vertically well-aligned geometry of the as-prepared Ni nanorod arrays (Figure 5-2b and c). The Ni nanorods possess a uniform diameter of ~160 nm,

and the interval distance between Ni nanorods is ~240 nm, inherited from the as-prepared PAM templates (Figure 5-2d and e). The length of the Ni nanorods was measured to be ~1.6 μm according to the cross-sectional SEM image (Figure 5-2f).

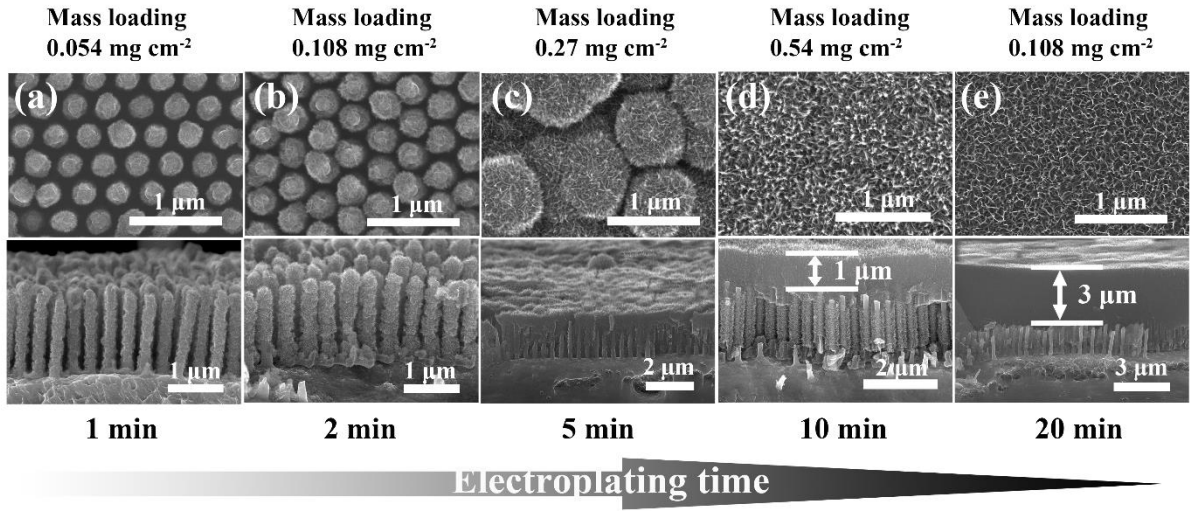

Figure 5-3 Top- and cross-sectional view SEM images of Ni nanorod arrays after electroplating MnO_2 of (a) 1 min, (b) 2 min, (c) 5 min, (d) 10 min, and (e) 20 min, respectively.

To prepare SCs electrodes, MnO_2 was subsequently electroplated onto these as-prepared Ni nanorods. Figure 5-3 show the SEM images of the as-prepared Ni nanorods after being coated with different amount of MnO_2. With the MnO_2 electroplating of 1 min (*i.e.*, the mass loading of MnO_2 is 0.054 mg cm^{-2}), a thin layer of MnO_2 were conformally coated onto each Ni nanorods (Figure 5-3a), which is the general way to construct SCs electrodes with nanoarchitectured current collectors. The obtained NN@MnO_2 electrode maintained the morphology as the bare Ni nanorod arrays and there are large enough interspaces between the adjacent MnO_2 coated Ni nanorods to allow the easy access of electrolyte ions. Such kind of electrode architecture has been proved to achieve very high specific capacitance. In the case with the MnO_2 electroplating of 2 min (*i.e.*, 0.108 mg cm^{-2} of MnO_2), the thickness of MnO_2 layer was significantly increased leading to the decreased interspaces between the adjacent MnO_2 coated Ni nanorods (Figure 5-3b). When further increasing the electroplating time to 5 min or even more, most of MnO_2 were found to deposit on the top rather than the wall of the

Ni nanorods, and eventually forming a thick MnO_2 layers on the top of Ni nanorods (Figure 5-3c-e). As can be seen from Figure 5-3e, a ~3 μm-thick MnO_2 layer was completely covered on the top of Ni nanorods after electroplating for 20 min and the corresponding mass loading of MnO_2 is 1.08 mg cm^{-2}.

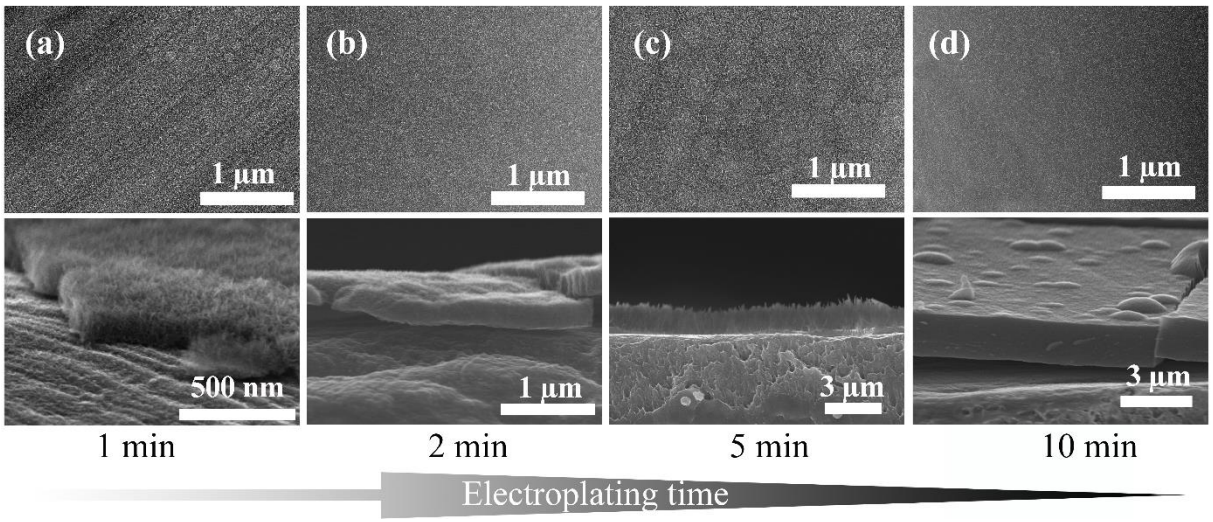

Figure 5-4 Top- and cross-sectional view SEM images of planar Ni foil current collector after electroplating MnO_2 of (a) 1 min, (b) 2 min, (c) 5 min, and (d) 10 min, respectively.

For comparison, we also deposited the same amount of MnO_2 on planar Ni foils as current collector with the same method. It seems no significant difference for thick MnO_2 layers deposited on flat Ni foil current collector (Figure 5-4), and the mass loading as well as layer thickness of MnO_2 increase with electroplating time. The major difference is under the thick MnO_2 layer, where there are much more electrical contact spots between MnO_2 layer and current collectors, attributing to the high specific surface area of Ni nanorod arrays. As reported previously,[134, 161] more electrical contact spots between pseudocapacitive materials and current collectors would be efficiently reduce the interfacial resistance, resulting in lower equivalent series resistance (ESR) in SCs, and finally an excellent energy storage capability could be highly expected. On the other hand, it is also worth noting that the lack of NF@MnO_2 electrode with the MnO_2 mass loading of 1.08 mg cm^{-2} is due to the fact that the MnO_2 layer became to crack and peeled off from Ni foils. From the other perspective, it demonstrates that the

utilization of nanoarchitectured current collectors for thick-layer SCs electrodes would increase the mechanical stability.

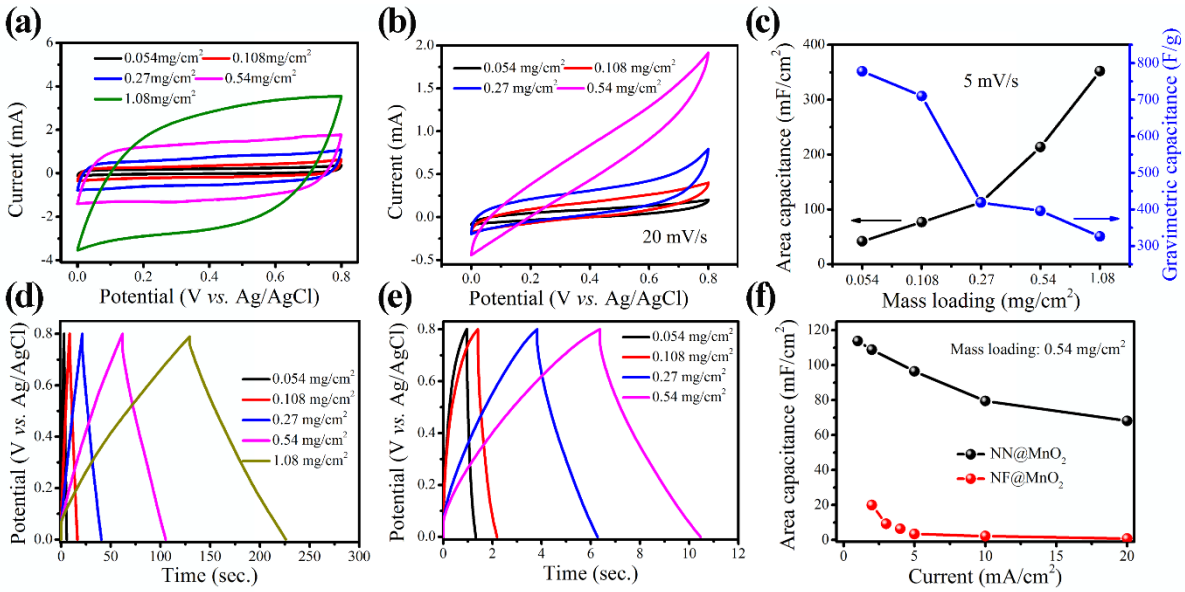

Figure 5-5 CV curves of (a) NN@MnO_2 and (b) NF@MnO_2 electrodes with different MnO_2 mass loading at a scan rate of 20 mV s^{-1}, respectively. (c) Area and gravimetric capacitance of NN@MnO_2 electrodes versus MnO_2 mass loading. GCD curves of (d) NN@MnO_2 and (e) NF@MnO_2 electrodes with different MnO_2 mass loading at current density of 2 mA cm^{-2}, respectively. (f) Areal capacitances comparison between NN@MnO_2 and NF@MnO_2 electrodes versus current density with the same MnO_2 mass loading of 0.54 mg cm^{-2}.

5.1.3 The electrochemical performance of NN@MnO_2 and NF@MnO_2 electrodes

The electrochemical properties of the NN@MnO_2 as SCs electrodes were firstly studied by carrying out CV and GCD using a conventional three-electrode configuration with a platinum foil as the counter electrode and Ag/AgCl as the reference electrode in an electrolyte of 1.0 M Na_2SO_4 aqueous solution. Figure 5-5a compares the CV curves of NN@MnO_2 electrodes with different MnO_2 mass loading at a scan rate of 20 mV s^{-1}. The CV curves of all NN@MnO_2 electrodes display a quasi-rectangular shape even for the NN@MnO_2 electrode with the high MnO_2 mass loading of 1.08 mg cm^{-2} (~3 μm in thickness). However, for MnO_2 coated Ni foils

(NF@MnO_2) electrodes with the same MnO_2 mass loading, the CV curves are severely distorted and the corresponding capacitive current is much lower than that of NN@MnO_2 electrodes (Figure 5-5b). The significant difference in CV performance should be mainly attributed to the current collectors, which is the only difference between NN@MnO_2 and NF@MnO_2 electrodes. In NN@MnO_2 electrodes, there is much larger interfacial area between MnO_2 and current collectors than that in NF@MnO_2 electrodes. Figure 5-5c summarizes the specific and areal capacitance (calculated from CV curves at a scan rate of 5 mV s^{-1}), respectively, of NN@MnO_2 electrodes with different MnO_2 mass loading. The highest specific capacitance is 795 F g^{-1} for NN@MnO_2 electrode with MnO_2 mass loading of 0.054 mg cm^{-2} (*e.g.*, ultrathin conformal coating), however, the corresponding areal capacitance is only 42 mF cm^{-2} due to the ultralow MnO_2 mass loading. When assembling into devices, the areal capacitance might be even lower and finally results in the low device energy density. This is why nanoarchitectured current collectors are always being complained for practical applications. With increasing the MnO_2 mass loading, the specific capacitance of NN@MnO_2 electrodes certainly decreases which the reason is generally believed to be the intrinsically low electric conductivity of MnO_2, on the contrary, the corresponding areal capacitance increases a lot (Figure 5-5c). For example, the specific capacitance of NN@MnO_2 electrode with MnO_2 mass loading of 1.08 mg cm^{-2} is only 326 F g^{-1}, but impressively the areal capacitance reaches 352 mF cm^{-2}, which is more than 8 times that of NN@MnO_2 electrode with MnO_2 mass loading of only 0.054 mg cm^{-2}, attributing to the much higher MnO_2 mass loading and also the contribution of nanoarchitectured current collectors. Figures 5-5d and e show the typical GCD curves of NN@MnO_2 and NF@MnO_2 electrodes with different MnO_2 mass loading, respectively, in the potential range of 0-0.8 V at a current density of 2 mA cm^{-2}. Remarkably, as compared to NF@MnO_2 electrodes, NN@MnO_2 electrodes exhibited more symmetrical charge-discharge curves and longer discharge time, suggesting the superior Coulombic efficiency and enhanced capacitance for

NN@MnO_2 electrodes. In accordance with the CV results, the areal capacitance of both NN@MnO_2 and NF@MnO_2 electrodes increases accompanying with the increased MnO_2 mass loading, but the areal capacitance of NN@MnO_2 electrodes was significantly higher than those of NF@MnO_2 electrodes with the same MnO_2 mass loading. The areal capacitance of NN@MnO_2 electrode with the MnO_2 mass loading of 0.54 mg cm^{-2} is 108 mF cm^{-2} at a current density of 2 mA cm^{-2}, while only 20 mF cm^{-2} for NF@MnO_2 electrode under the same conditions. Actually, the areal capacitance of NN@MnO_2 electrode at 20 mA cm^{-2} (*i.e.*, 69 mF cm^{-2}) is even much higher than that of NF@MnO_2 electrode at 2 mA cm^{-2}. Such remarkably high capacitance at high current density should still be attributed to the more electrical contact spots between pseudocapacitive materials and current collectors in NN@MnO_2 electrodes. In addition, NN@MnO_2 electrodes have remarkable rate capability with ~61% capacitance retention as the current density increasing from 1 to 20 mA cm^{-2}.

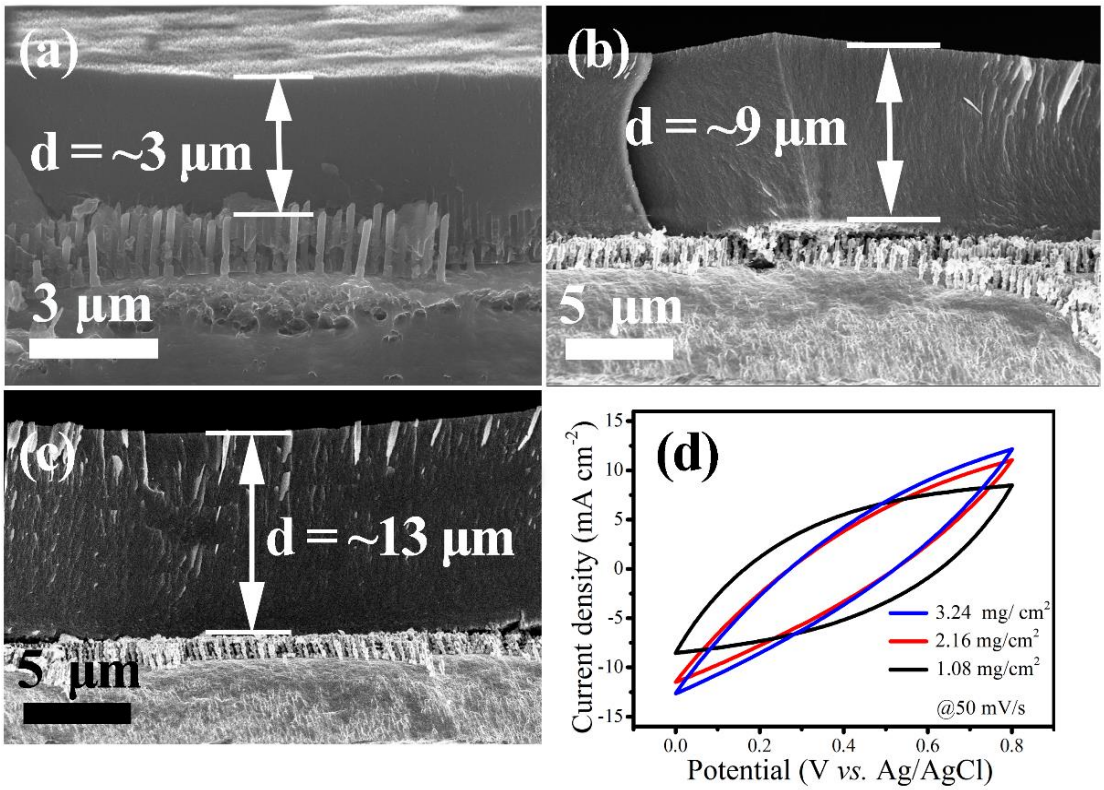

Figure 5-6 Typical cross-sectional SEM images of NN@MnO_2 electrodes with the MnO_2 electroplating time of (a) 20 min, (b) 40 min and (c) 60 min. With prolonged electrodeposition

time, the thickness of MnO_2 layer increased from 3 μm gradually to 13 μm and the corresponding MnO_2 mass loading increased from 1.08 to 3.24 mg cm^{-2}. (d) The CV curves of NN@MnO_2 electrodes with different MnO_2 thickness layers.

When further increasing the MnO_2 plating time from 20 min to 40 and 60 min, respectively, the MnO_2 layer thickness reached to 9 and 13 μm, respectively (Figure 5-6a-c), with the corresponding MnO_2 mass loading of 2.16 and 3.24 mg cm^{-2}, respectively. The CV characterizations (Figure 5-6d) revealed that the areal capacitance of the new NN@MnO_2 electrodes with 9 μm thick MnO_2 layer (MnO_2 mass loading of 2.16 mg cm^{-2}) was only 10% higher than that of NN@MnO_2 electrodes with 3 μm thick MnO_2 layer (MnO_2 mass loading of 1.08 mg cm^{-2}). Since all structural parameters of Ni nanorod arrays are kept constant in present work, the interfacial contact area between pseudocapacitive materials and current collectors is the same for all NN@MnO_2 electrodes with either 3 μm thick or 9 μm thick MnO_2 layer, thus resulting in the very small capacitance contribution from the 100% more MnO_2. The only 10% increase in areal capacitance compared with the 100% increase in MnO_2 mass loading further indicates the important role of the interfacial contacts between pseudocapacitive materials and current collectors in determining the energy storage capability of SCs electrodes with thick pseudocapacitive materials layer. Moreover, when further increasing the MnO_2 electroplating time to 60 min, the MnO_2 thickness reached to 13 μm (MnO_2 mass loading of 3.24 mg cm^{-2}), but the areal capacitance was only 2% higher than that of NN@MnO_2 electrodes with 9 μm thick MnO_2 layer compared to 50% increase in MnO_2 mass loading, while 12% higher than that of NN@MnO_2 electrodes with 3 μm thick MnO_2 layer compared to 200% increase in MnO_2 mass loading. Note that Ni nanorod arrays in this work are just one representative nanoarchitectured current collectors. To achieve higher areal capacitance in the case of much thicker pseudocapacitive material layer, the structural parameters of Ni nanorod arrays also

have to be further optimized to obtain much larger interfacial contact area between pseudocapacitive materials and current collectors.

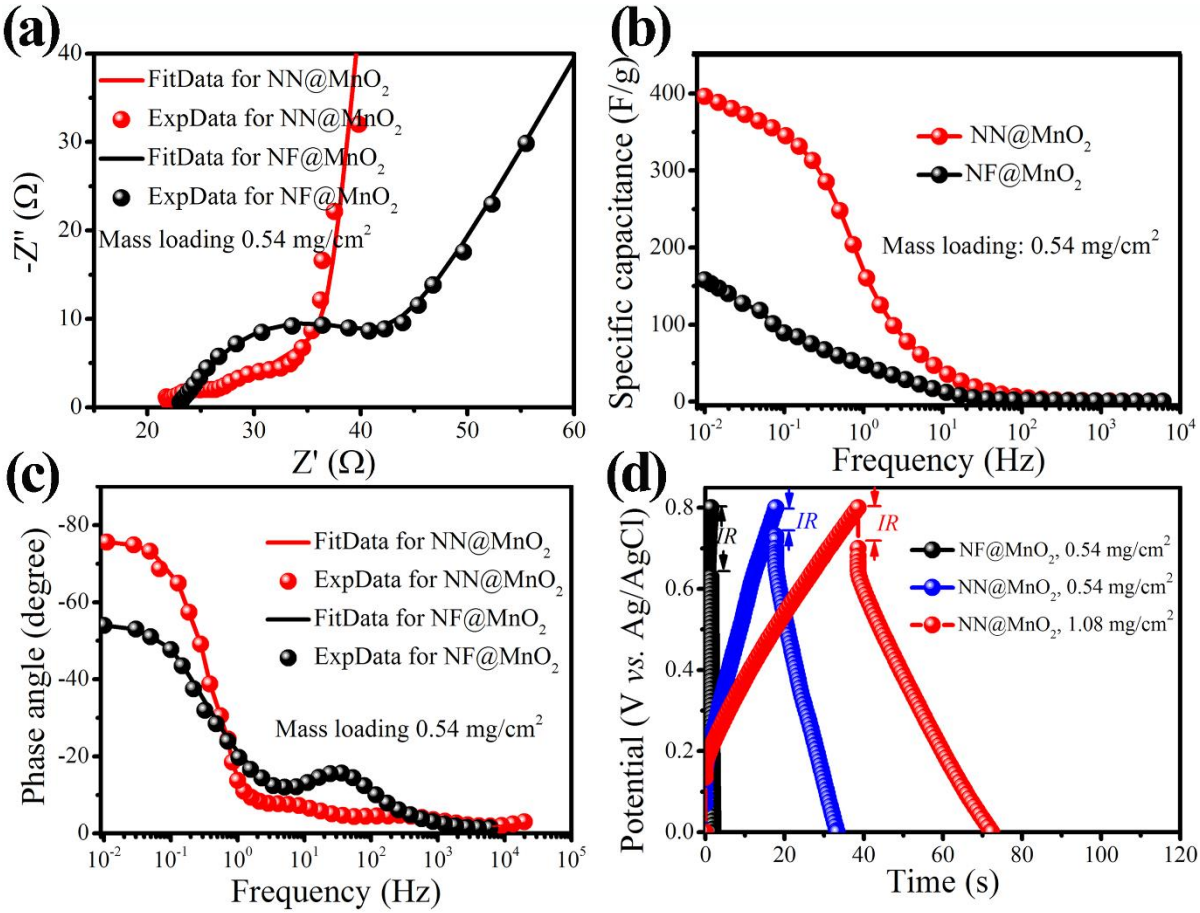

Figure 5-7 (a) Nyquist plots, (b) Frequency response of the capacitance, and (c) Bode plots of NN@MnO_2 and NF@MnO_2 electrodes with the MnO_2 mass loading of 0.54 mg cm^{-2}. (d) GCD curves of NN@MnO_2 and NF@MnO_2 electrodes with different MnO_2 mass loading at a current density of 5 mA cm^{-2}.

5.1.4 Electrochemical impedance analysis of NN@MnO_2 and NF@MnO_2 electrodes

Furthermore, EIS was performed in order to achieve better understanding about the role of nanoarchitectured current collectors in SCs electrodes with pseudocapacitive materials in the form of thick layer. Figure 5-7a shows the Nyquist plots of NN@MnO_2 and NF@MnO_2 electrodes with the same MnO_2 mass loading of 0.54 mg cm^{-2}. All Nyquist plots exhibit two distinct parts including a semicircle in the high-frequency region (charge transfer process) and

a sloped straight line in the low-frequency region (diffusion-limited process). At the high frequency, the intersection of the curve at the real part indicates the resistance of the electrochemical system (R_s, which includes the inherent resistance of the pseudocapacitive material, ionic resistance of electrolyte, and contact resistance at the interface between electrolyte and electrode) and the diameter of semicircle reflects the charge transfer resistance (R_{ct}) at the electroactive-material/current collector interface.[162-165] Both NN@MnO_2 and NF@MnO_2 electrodes have the similar R_s, suggesting the negligible influence on the series bulk resistance with the use of nanoarchitectured current collectors. As estimated from Nyquist plots, the R_{ct} of NN@MnO_2 electrode is 5.4 Ω, which is much smaller than that of NF@MnO_2 electrode (28 Ω). It could be concluded that the lower R_{ct} arises from the well adhered interface between MnO_2 and nanoarchitectured current collectors.

Bode plots of the frequency response of capacitance also indicate the significant difference between NN@MnO_2 and NF@MnO_2 electrodes with thick MnO_2 layer (Figure 5-7b). It is clear that NN@MnO_2 electrode has a higher capacitance at low frequencies compared to that of NF@MnO_2 electrode. Moreover, the operating frequency (that is the frequency at half-maximum capacitance) of NN@MnO_2 and NF@MnO_2 electrodes are 1 and 0.22 Hz, respectively, corresponding to the characteristic relaxation time constant (τ_0) of 1 and 4.55 s, respectively, indicating the better charge–discharge rate performance for NN@MnO_2 electrodes.[166] Since the MnO_2 in both electrodes were synthesized in the same way and the obtained dense MnO_2 layer has very similar mass loading as well as morphology, it could be concluded that the type of current collectors should be responsible for the observed difference in Bode plots. Moreover, the influence of current collectors is also reflected in the phase response of the frequency. With the same MnO_2 mass loading of 0.45 mg cm^{-2}, the phase angle of NN@MnO_2 electrode reaches −76º at low frequencies, while −54º for NF@MnO_2 electrode (Figure 5-7c), confirming a more ideal capacitive behavior of NN@MnO_2 electrode.

Additionally, Figure 5-7d presents the voltage (IR) drops NN@MnO_2 and NF@MnO_2 electrodes with different MnO_2 mass loading at a current density of 5 mA cm^{-2}. With the same MnO_2 mass loading (0.54 mg cm^{-2}), the IR drop of NN@MnO_2 electrode is 58 mV, much lower than that of NF@MnO_2 electrode (180 mV). Upon increasing the MnO_2 mass loading to 1.08 mg cm^{-2}, the IR drop of NN@MnO_2 electrode was increased to 97 mV, but still much lower than that of NF@MnO_2 electrode with low MnO_2 mass loading (0.54 mg cm^{-2}), confirming the good electrical conductivity in NN@MnO_2 electrodes.

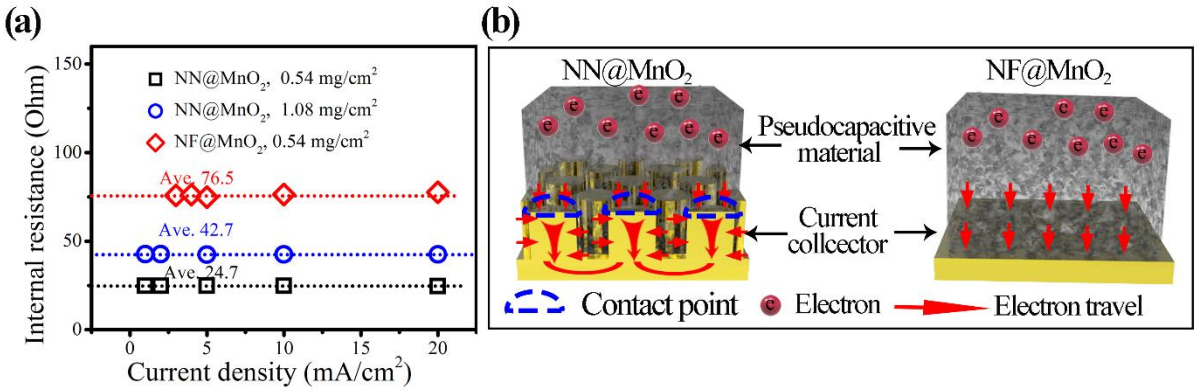

Figure 5-8 (a) Internal resistances of NN@MnO_2 and NF@MnO_2 electrodes calculated from GCD curves with different current densities. (b) Schematic illustration of electron transport between pseudocapacitive materials and different current collectors, respectively.

Figure 5-8a summarizes the internal resistance of NN@MnO_2 and NF@MnO_2 electrodes obtained from GCD curves with different current densities. The internal resistance has the same change tendency in accordance with the Nyquist plots and this result again indicates that nanoarchitectured current collectors could contribute to reduce the internal resistance of SCs electrodes when pseudocapacitive materials are in the form of thick layer. On the basis of all results discussed above, a schematic diagram can be proposed to compare the charge carrier transport between pseudocapacitive materials and different current collectors in the SCs with thick-layer pseudocapacitive materials (Figure 5-8b). By taking advantages of nanoarchitectured current collectors that have 3D conductive network and large specific surface,

there are more contact spots at the electroactive-material/current-collector interfaces to significantly lower the interfacial resistance caused by the limited contact spots in conventional thick-film SCs electrodes with planar current collectors like metallic foils. The more contact spots provide more possible pathways to facilitate charge carrier transport during charge–discharge process, then subsequently to reduce the charge transfer resistance at the electroactive-material/current collector interface. As a result, the internal resistance of the electrodes will be decreased and the energy storage capability will be further improved.

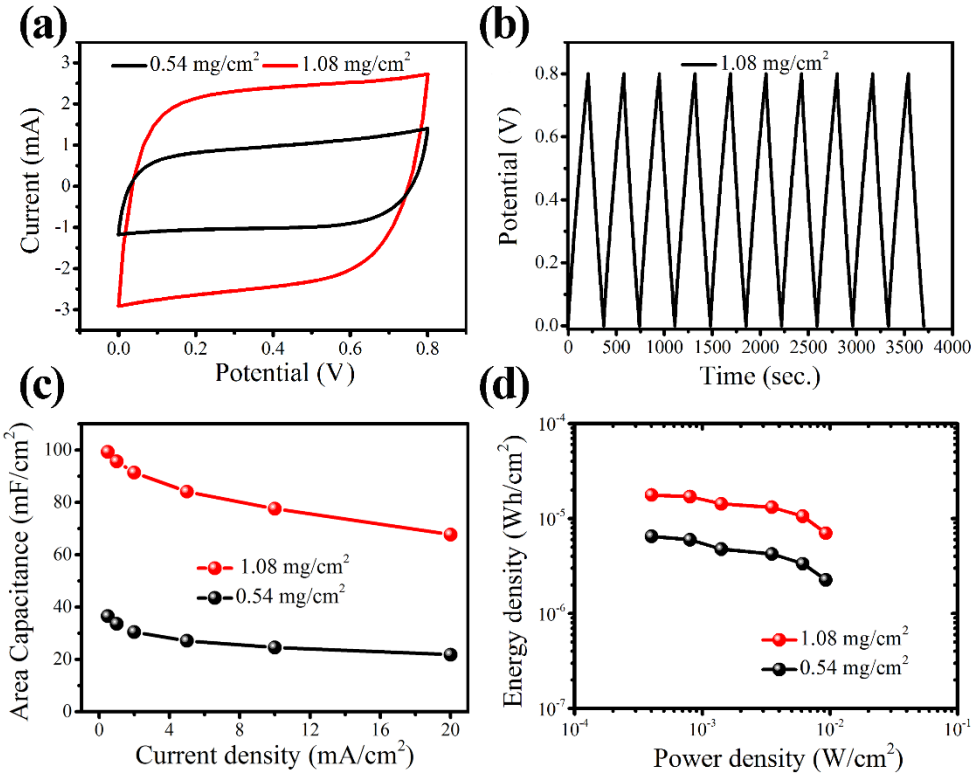

Figure 5-9 Performance of symmetric SC device based on NN@MnO_2 electrodes with different MnO_2 mass loading: (a) CV curves at a scan rate of 50 mV s^{-1}. (b) GCD curves at the current density of 0.5 mA cm^{-2}. (c) Areal capacitance as a function of current densities. (d) Ragone plots.

To further evaluate the SCs performance of NN@MnO_2 electrodes with thick-layer MnO_2, symmetric SCs were finally fabricated using two NN@MnO_2 electrodes with 1.0 M Na_2SO_4 aqueous solution as electrolyte. Figure 5-9 shows the typical electrochemical performance for

NN@MnO_2 electrodes with the MnO_2 mass loading of 0.54 and 1.08 mg cm^{-2}, respectively (corresponding to the MnO_2 layer thickness of 1 and 3 μm, respectively). Both CV curves show nearly symmetrical rectangular shapes at a scan rate of 50 mV s^{-1} (Figure 5-9a). With increasing the scan rate to 200 mV s^{-1}, the device based on NN@MnO_2 electrode with 3 μm thick MnO_2 layer still keeps a rather good rectangular-like CV curve, indicating the desirable fast charge–discharge properties. The typical GCD curves of the device based on NN@MnO_2 electrode with 3 μm thick MnO_2 layer show highly symmetric and nearly linear slopes at a current density of 0.5 mA cm^{-2} (Figure 5-9b). The area capacitance of the device with respect to the mass of MnO_2 has been calculated from GCD curves at different current densities and plotted in Figure 5-9c. The area capacitance is 100 and 37 mF cm^{-2} for the device based on NN@MnO_2 electrode with 3-μm- and 1-μm-thick MnO_2 layer, respectively, at a current density of 0.5 mA cm^{-2}. At a high current density of 20 mA cm^{-2}, the device based on NN@MnO_2 electrode with 3-μm-thick MnO_2 layer decayed to 68 mF cm^{-2}, but still higher than that of the device based on NN@MnO_2 electrode with 1 μm thick MnO_2 layer at a current density of 0.5 mA cm^{-2}. Figure 5-9d shows the Ragone plots comparing the areal energy density and power density of NN@MnO_2 electrode-based symmetric devices with different MnO_2 mass loading. It reveals a significant increase in the SCs performance when the MnO_2 mass loading increase from 0.54 to 1.08 mg cm^{-2}.

5.2 Design and characterization of EPAM@SnO_2 as nanoarchitectured current collectors

PAMs are usually served as nanostructuring templates and they are completely removed after the active material being deposited into the porous membranes, since the insulated nature of them is hardly useful for the electrochemical devices. The as-prepared nanostructured arrays preserve the vertical shape of the PAM templates, yet have a limited aspect ratio to avoid the agglomeration and to maintain highly oriented nature, otherwise the excessive aspect ratio could block the straight pathways for ion transport to the surface of active materials.[123] Besides,

from the electrode design point of view, the limited aspect ratio or agglomeration of 1 D nanostructure arrays would largely restrict the development of the PAM template-assist method. One way to break the boundaries of aspect ratio is to construct self-supported nanopore arrays, which use the highly etched nanoporous alumina membranes (EPAMs) as a building block instead of etching them away.

5.2.1 The design philosophy of EPAM scaffold

Nanoengineering of pseudocapacitive materials and/or current collectors is essentially an efficient methodology for improving the energy storage capability of MSCs.[70, 167-169] Especially, tremendous research efforts are ongoing to utilize PAMs as nanostructuring templates for fabricating nanostructured electrodes.[170-173] With PAMs as nanostructuring templates, the pseudocapacitive materials are normally synthesized into the arrayed nanowire and/or nanotube onto the conductive substrates as MSC electrodes.[108-111] In similar way, conductive materials are fabricated into the arrayed nanowire, nanotube or nanopore to serve as nanoarchitectured current collectors to produce hetero-nanostructured MSC electrodes.[31, 34, 106-107, 123, 174] Both approaches have been proved to significantly improve the performance of MSCs. Beyond as the nanostructuring templates and despite of the intrinsically insulating nature, PAMs have also been investigated as nanostructured substrates to fabricate high-performance metal-insulator-metal electrostatic nanocapacitor and all-in-one nanopore battery, respectively, mainly by taking advantages of its distinguished structural features, *i.e.*, high specific surface area and highly-oriented nanochannels.[170-172] For instance, with PAMs grown on an aluminum wire as both the nanostructuring templates and the nanostructural supporters for 3D graphene-nanotubes, all-solid-state wire-shaped SCs have been prepared and exhibited outstanding performance.[173] Inspired by the aforementioned results and considering the rigid electrode design criteria for MSCs, the design strategy is to construct MSC electrodes by taking

advantages of the highly-oriented nanochannels of PAMs as both nanostructuring template and structurally-supporting framework.

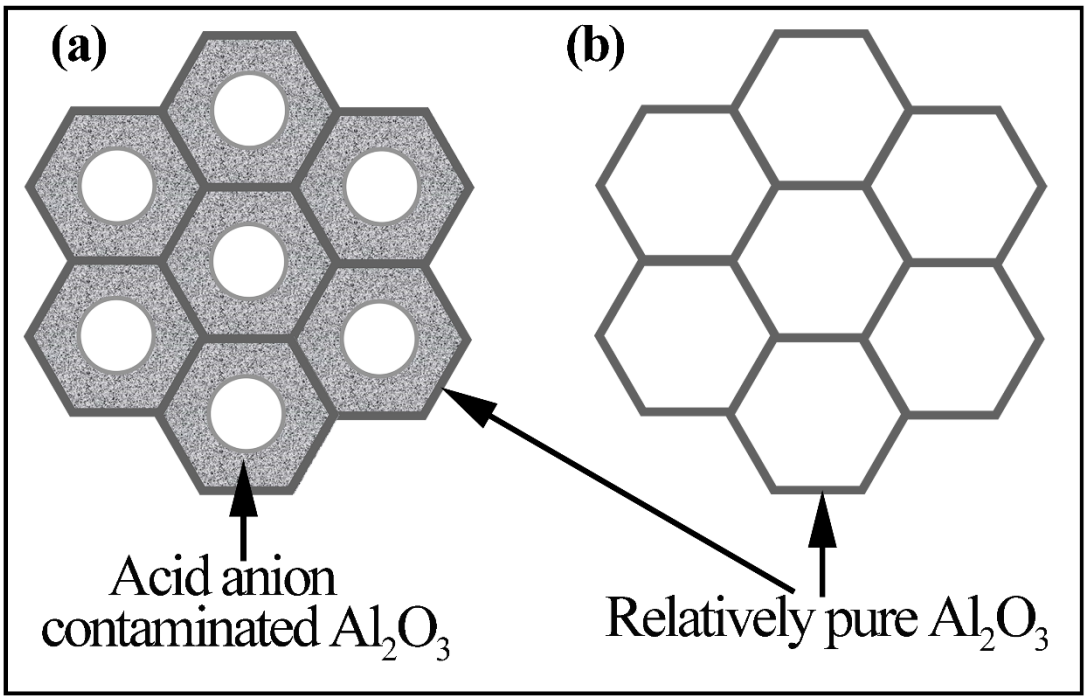

Figure 5-10 (a) Schematic illustration of the double-layer cell structure of PAM. (b) Schematic diagram showing EPAM consisting of only honeycomb-like structure.

From the structural point of view, PAM represents one promising electrode architecture for MSCs.[123] The vertically-aligned and robustly-stable nanoporous structure of PAM provides large surface area with high ionic accessibility to electrochemically store more charges, meanwhile facilitates rapid diffusion of electrolyte ions to achieve higher rate performance. Unfortunately, the insulating nature confines PAM to be generally utilized as nanostructuring templates to fabricate nanoelectrodes in the form of arrayed nanowires and/or nanotubes for MSCs,[31, 34] and these nanoelectrodes usually suffer from the limit of aspect ratio to avoid agglomeration and maintain highly-oriented nature. Although metallic nanopores have been fabricated though two-step replication PAM method, but in fact they still face the challenge of limited aspect ratio because of the nanowire intermediate during the fabrication process.[123] In the present work, besides serving as nanostructuring templates and instead of being completely

removed, PAM is intentionally etched and retained in the as-prepared nanoelectrodes. The significant merit of such design is that the presence of PAM would reinforce nanoelectrodes to ensure vertically-aligned and robustly-stable nanoporous feature without aspect ratio limitation. However, as a result of the insulating nature, PAM in electrodes will inevitably be obligated to "dead volume" similar with the nonconductive polymeric binders in conventional thin-film MSC electrodes, thus the proportion of PAM in nanoelectrodes must be reduced as far as possible. Thompson and Wood have revealed the double-layer cell structure of PAM (Figure 5-10a), which includes an acid anion-contaminated Al_2O_3 thick layer adjacent to the pore and a relatively pure Al_2O_3 thin layer remote from the pore.[175] Conventionally, the acid anion-contaminated Al_2O_3 thick layer is partially dissolved to finally obtain PAM with round-shaped pore and desired pore diameter, and then they are further utilized as nanostructuring templates. Once this acid anion-contaminated Al_2O_3 thick layer is completely dissolved, a honeycomb-like alumina nanoscaffold composing of only the relatively pure Al_2O_3 thin layer will be generated, as schematically depicted in Figure 5-10b, and this should be the critical structure of EPAM.

5.2.2 Morphology and nanostructure of EPAM@SnO_2

The fabrication process for SnO_2 coated EPAM (depicted as EPAM@SnO_2) electrodes is schematically illustrated in Figure 5-11. In the present work, an example EPAMs with highly-ordered hexagonal pore arrangement in a periodicity of 400 nm were firstly fabricated through anodizing a surface nanoscale-indented aluminum foil. Specifically, the key fabrication steps involve: (i) anodization of the indented aluminum foil at certain anodization time, (ii) deposition of an ultrathin Au/Ti layer and Ni substrate on the top of PAM template, (ii) removal of Al substrate and barrier layer on the backside of the anodized foil to obtain through-pore structure with a conductive substrate, (iii) further wet chemical etching to achieve EPAM skeleton, (iv) conformal deposition of SnO_2 layer on the EPAM scaffold. Notably, before etching PAM to

obtain honeycomb-like alumina nanoscaffold, a thick layer of Ni (~7 μm) was firstly deposited onto the surface of PAM as the supporting substrate. With this Ni layer as the conductive substrate, no additional current collector needs to be deposited.

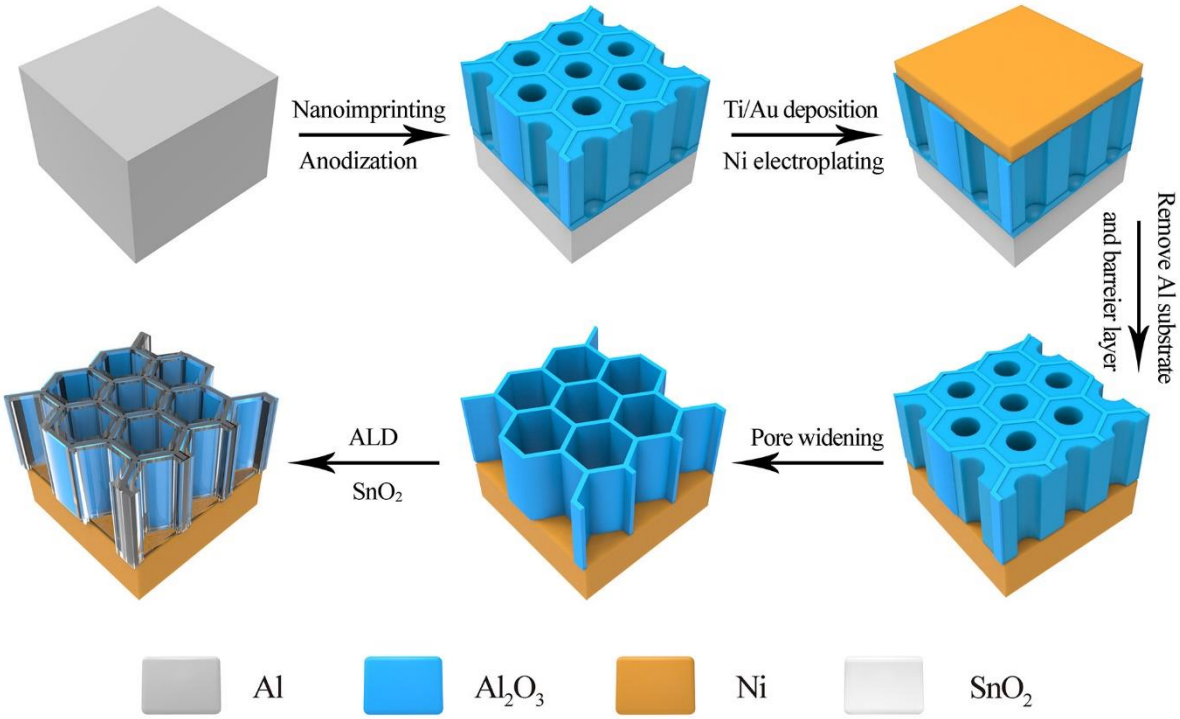

Figure 5-11 Schematic illustration of fabricating EPAM@SnO_2 scaffold.

Table 5-1 Summary of the fabrication details for the EPAM scaffolds with various anodization time.

Samples	Anodization time (min)	Pore-depth (μm)[1]	Wet chemical etching time (min)
EPAM20	20	6.4	20
EPAM40	40	12	30
EPAM90	90	25	40

[1]The pore-depth of the as-prepared EPAM is determined by the cross-sectional SEM images.

Note that the EPAM skeleton with honeycomb-like structure should be precisely etched by aqueous H_3PO_4 solution (5 wt%): if the etching time is short, the wall of pore is thick and will take a large dead volume in the nanochannels; on the contrary, if the etching time is too long,

the honeycomb structure will be undoubtedly damaged. Table 5-1 shows that the EPAM scaffolds with various pore-depths are precisely controlled by the anodization time, and accordingly the chemical etching time should also be varied. Figure 5-12a is the SEM image of PAM after removing the barrier layer, clearly unveiling the double-layer cell structure of PAM. Through a precisely controlled etching process to gain specific surface area as large as possible, the honeycomb nanoscaffold in large scale was obtained with the pore wall thickness of only 16 nm (Figure 5-12b), which almost reaches the limit for keeping the entire and stable nanoporous structure of EPAM. As a result, the proportion of EPAM in nanoelectrodes will be greatly reduced when constructing nanoelectrodes with such honeycomb nanoscaffold as keel.

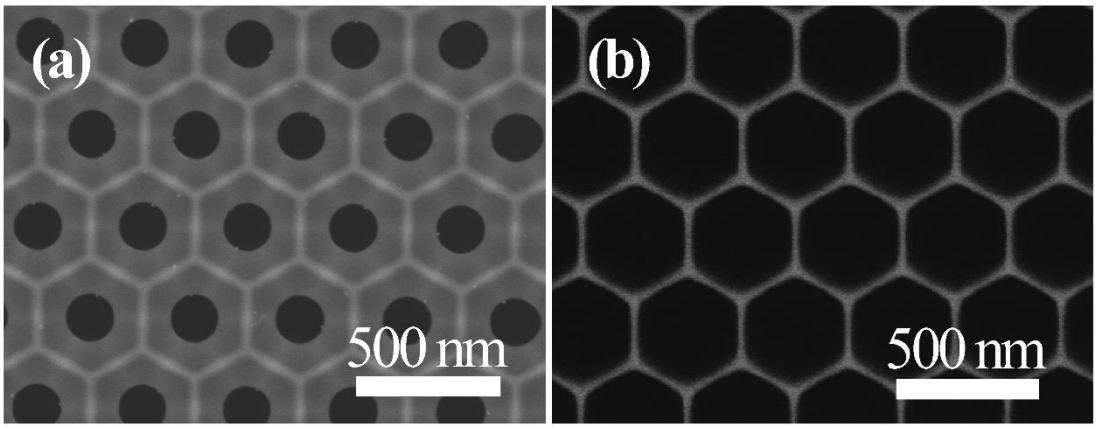

Figure 5-12 (a) SEM image of PAM after removing barrier layer. (b) SEM image of EPAM with honeycomb nanoscaffold after etching process.

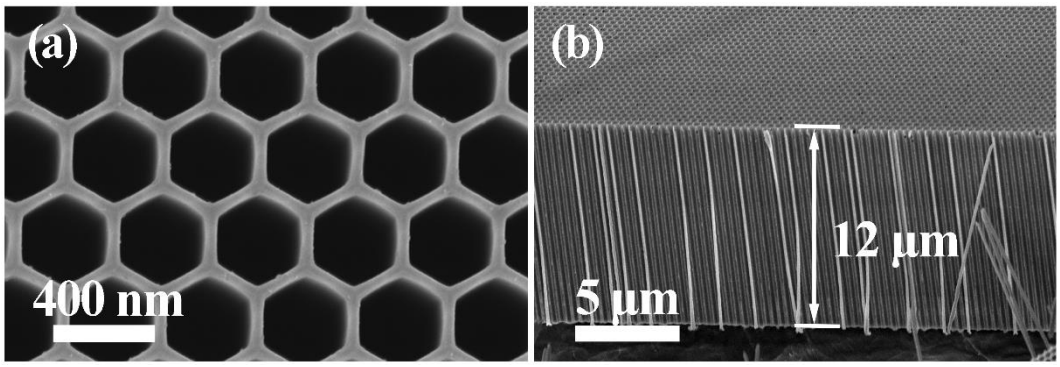

Figure 5-13 (a) Top- and (b) cross-sectional view SEM images of the EPAM40@SnO_2 electrode.

Finally, EPAMs with only the hexagonal skeleton were conformally coated with 12-nm-thick SnO_2 layer though ALD process (1500 cycles). Since EPAMs fabricated through 20, 40, and 90 min anodization, respectively, were used as the supporting framework, the as-prepared electrodes are depicted as EPAM20@SnO_2, EPAM40@SnO_2 and EPAM90@SnO_2 electrodes, respectively. Taking EPAM40@SnO_2 electrodes as an example, they were characterized by SEM (Figure 5-13a). Obviously, the EPAM40@SnO_2 electrodes remained the main structure features as EPAMs but only the pore diameter was slightly reduced. Figure 5-13b also reveals the pore-depth of EPAM40@SnO_2 electrodes to be about 12 μm, which the aspect ratio is calculated to be about 35. Here, the EPAMs functionalize as the mechanically robust supporting framework to ensure high specific surface area and straight ionic diffusion pathway being achieved simultaneously. Moreover, EPAMs as the supporting framework could strengthen the structural stability of the electrodes not only to eliminate the agglomeration and collapse of free-standing nanowire and/or nanotube arrays with high aspect ratio, but also benefit to improving the device performance stability during long-termed cycling.

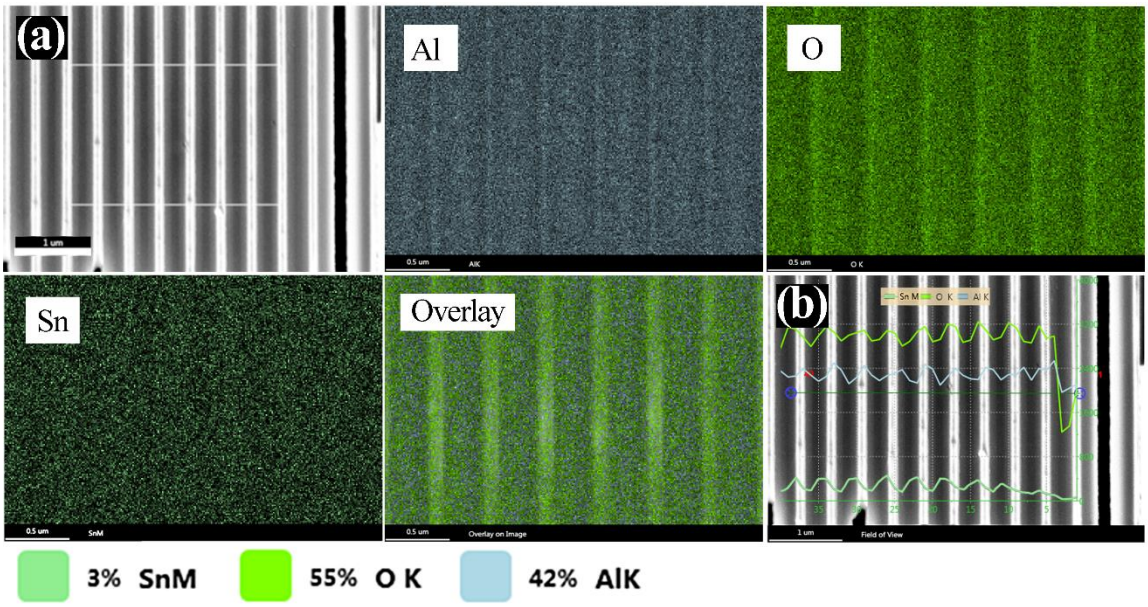

Figure 5-14 (a) EDX mapping and (b) EDX line-scan of cross-section of EPAM@SnO_2, showing a regular distribution profiles of Al, O, and Sn elements.

The composition of as-prepared EPAM@SnO_2 porous structure was confirmed by EDX mapping and line-scanning (Figure 5-14a). The cross-sectional EDX maps of the EPAM@SnO_2 porous structure confirmed the perfect matching of the spatial distributions of Al (cyan), O (green) and Sn (light green) with the vertically arrangement of uniform nanochannels. All the elemental distributions coincide with the frame of the remaining template. The EPAM@SnO_2 porous structure was also confirmed by an EDX line-scan along the radial direction of the cross-sectional structure (Figure 5-14b). The periodic elemental distributions of Al (cyan curve), O (green curve) and Sn (light green curve) perfectly match each other according to the periodic channel structure.

5.2.3 Electrochemical characterization for EPAM@SnO_2

To verify the possibility of EPAM@SnO_2 as nanoarchitectured current collectors, a symmetric MSC based on two EPAM@SnO_2 electrodes, EPAM@SnO_2//EPAM@SnO_2, was assembled and characterized since SnO_2 is also one kind of electroactive materials for SCs. Rate performance of MSCs, especially under high scan rate, could indirectly reflect the ionic and electronic transport behavior of EPAM@SnO_2 electrodes.

The ultrafast charging-discharging performance using CV experiments was firstly evaluated. The electrolyte was 1.0 M Na_2SO_4 aqueous solution, and the potential window was 0 – 1 V. For MSC based on two EPAM20@SnO_2 electrodes, the CV curves obtained at different scan rates are given in Figure 5-15a. All the CV curves maintain a quasi-rectangular shape even at an ultrahigh scan rate of 100 V s^{-1}, which reveals the ideal EDLC charge-storage behavior of the MSC. It should be noted that MSC based on two EPAM20@SnO_2 electrodes can even work very efficiently at ultrahigh scan rates up to 500 V s^{-1}. Figure 5-15b shows the corresponding variation of the discharge current density at different scan rates. Clearly, the discharge current maintained a linear relationship upon scan rates nearly until 150 V s^{-1}, indicating the high instantaneous power characteristics of MSC. Such ultrahigh rate performance should be

attributed to the straight nanochannels in EPAM20@SnO_2 electrodes allowing the rapid mass transport of ions during the ultrafast charging-discharging process. In addition to the ionic transport, the transport and collection of charges also play important role in determining the ultrahigh rate performance, which greatly relies on the electrical conductivity of the EPAM@SnO_2 electrodes.

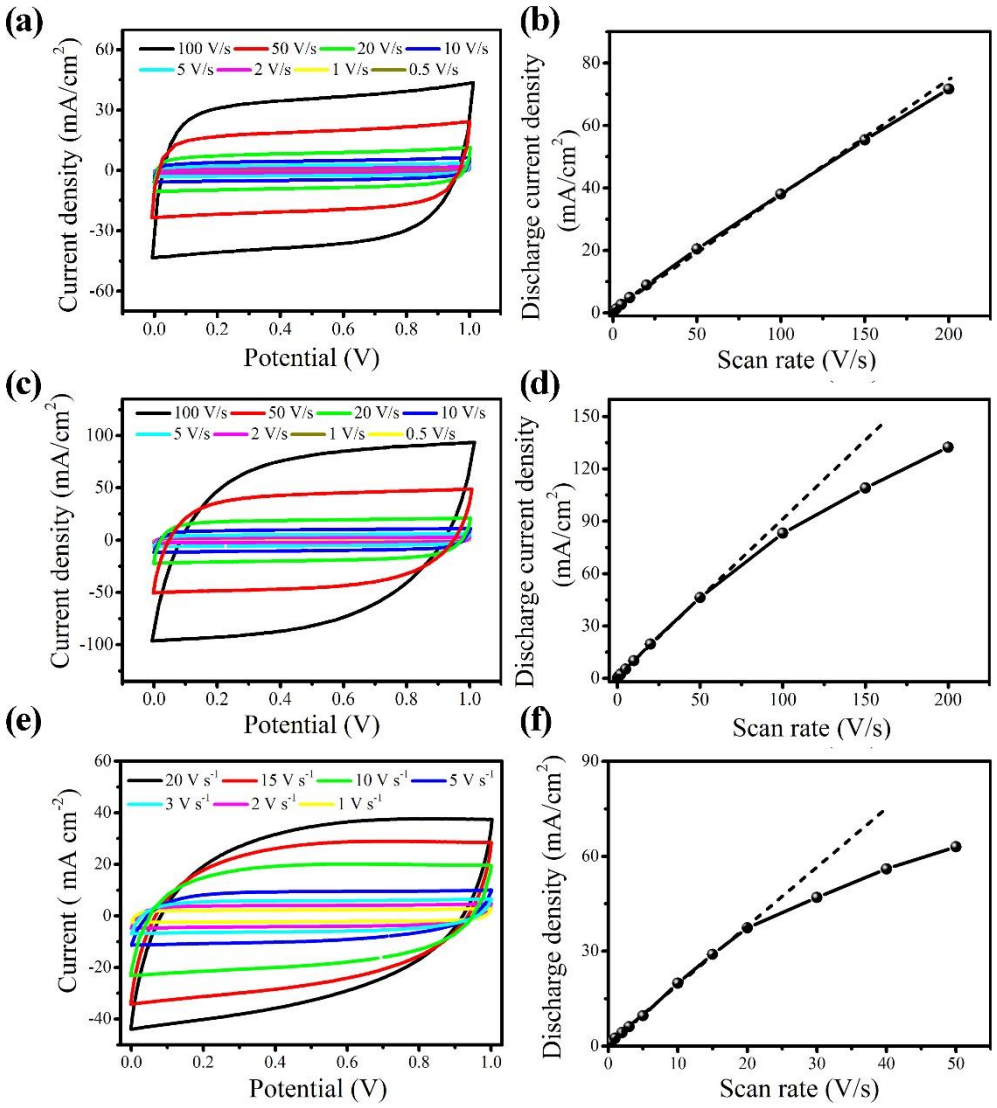

Figure 5-15 CV curves of MSCs at different scan rates and the corresponding discharge current as function of the scan rates: (a-b) EPAM20@SnO_2 electrodes based MSC; (c-d) EPAM40@SnO_2 electrodes based MSC; (e-f) EPAM90@SnO_2 electrodes based MSC.

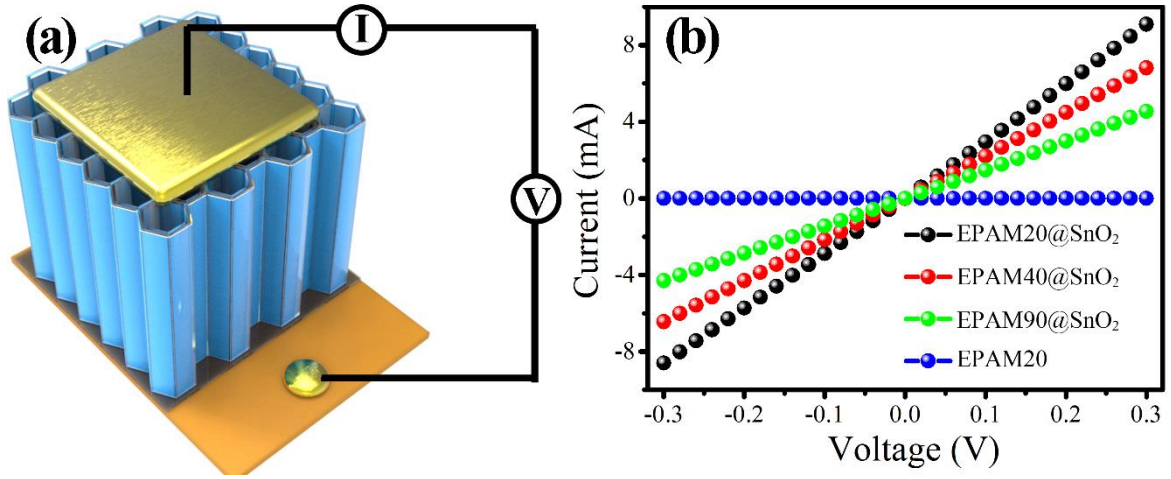

Figure 5-16 (a) A schematic view of a closed-loop circuit between the EPAM@SnO_2 film and the substrate and (b) typical current-voltage (I-V) characteristics for EPAM20@SnO_2, EPAM40@SnO_2 and EPAM90@SnO_2 electrodes, respectively.

However, the electrical resistances of EPAM40@SnO_2 electrodes and EPAM90@SnO_2 electrodes are higher than that of EPAM20@SnO_2 electrodes, confirmed by the I-V measurement results (Figure 5-16). The higher electrical resistance of EPAM40@SnO_2 and EPAM90@SnO_2 electrodes will bring negative effect on charges transport and collection during the ultrafast charging-discharging process. Consequently, the CV curves of the EPAM40@SnO_2 and EPAM90@SnO_2 electrodes based MSCs at various scan rates (Figures 5-15c and e) are not as good as those of EPAM20@SnO_2 electrodes based MSC, and Figure 5-15d and f indicate a linear relationship of the discharge current upon scan rates to reach until 50 V s^{-1} for EPAM40@SnO_2 electrodes based MSC and 20 V s^{-1} for EPAM90@SnO_2 electrodes based MSC, respectively, which are slightly inferior compared with that of EPAM20@SnO_2 electrodes based MSC that is 150 V s^{-1}.

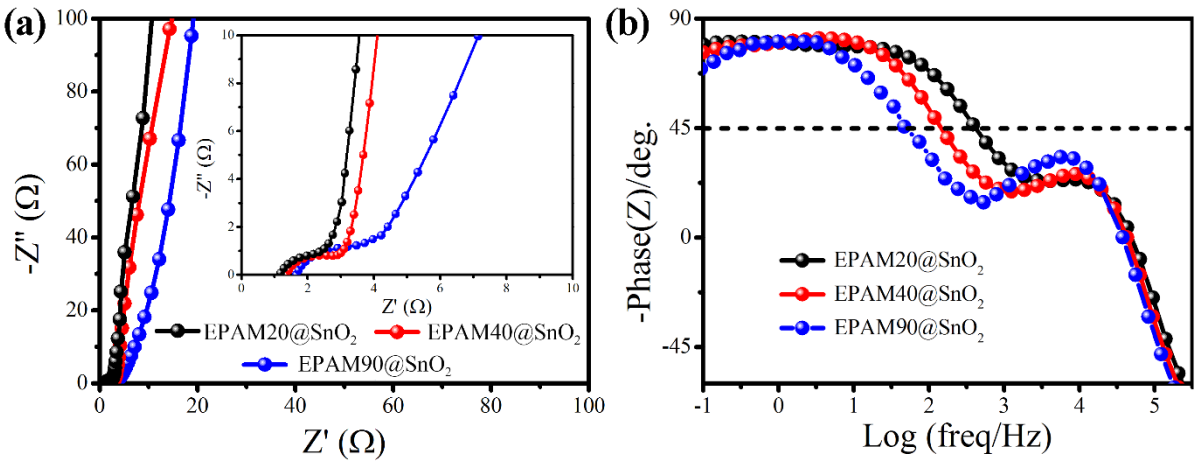

Figure 5-17 Impedance characterizations of MSCs based on EPAM20@SnO_2, EPAM40@SnO_2 and EPAM90@SnO_2 electrodes, respectively: (a) Nyquist plot; (b) Bode plot.

Furthermore, the EIS was performed to study the ultrafast ion and electron transport characteristics in MSCs based on EPAM20@SnO_2, EPAM40@SnO_2 and EPAM90@SnO_2 electrodes, respectively. It was found that the EIS results correlated well with the CV results. Figure 5-17a shows the representative Nyquist plots of the MSCs, and inset is the expanded view at the high-frequency region suggesting the capacitive behavior at high frequencies, which is attributed to the fully accessible surface area of the electrodes for electrolyte ion adsorption/desorption.[176] Obviously, the Nyquist plots show a high-frequency semicircle reflecting the R_{ct} in the electrodes. Compared to EPAM20@SnO_2 electrodes based MSC (R_{ct} = 1.3 Ω) or EPAM40@SnO_2 electrodes based MSC (R_{ct} = 1.5 Ω), the bigger semicircle (R_{ct} = 2.1 Ω) for EPAM90@SnO_2 electrodes based MSC should be ascribed to the fact that the charges need to transport through a longer path in EPAM90@SnO_2 electrodes before being collected by the current collector. The ESR are calculated to be 0.66 Ω for EPAM20@SnO_2 electrodes based MSCs, 0.92 Ω for EPAM40@SnO_2 electrodes based MSCs, and 1.6 Ω for EPAM90@SnO_2 electrodes based MSCs, respectively. Since the ESR is closely related to the diffusion behavior of ions within the electrode, the lower ESR suggests the more rapid accessibility of the ions for electro-sorption at the whole electrode-electrolyte interface in

EPAM20@SnO_2 electrodes or EPAM40@SnO_2 electrodes based MSCs than that in EPAM90@SnO_2 electrodes based MSC. Figure 5-17b is the Bode plots about the impedance phase angles of the MSCs as functions of frequency. The phase angles of both MSCs at the low frequency region are about -80°, indicating the near-ideally capacitive behavior. The characteristic frequency (f) at the phase angle of -45° is 707.9 Hz for the EPAM20@SnO_2 electrodes based MSCs, 199.5 Hz for EPAM40@SnO_2 electrodes based MSCs, and 52.5 Hz for EPAM90@SnO_2 electrodes based MSCs, corresponding to the time constant (τ_0) of 1.4, 5.0, and 19 ms respectively. The shorter τ_0 for the EPAM20@SnO_2 or EPAM40@SnO_2 electrodes based MSCs reveals the faster charge-discharge rate.

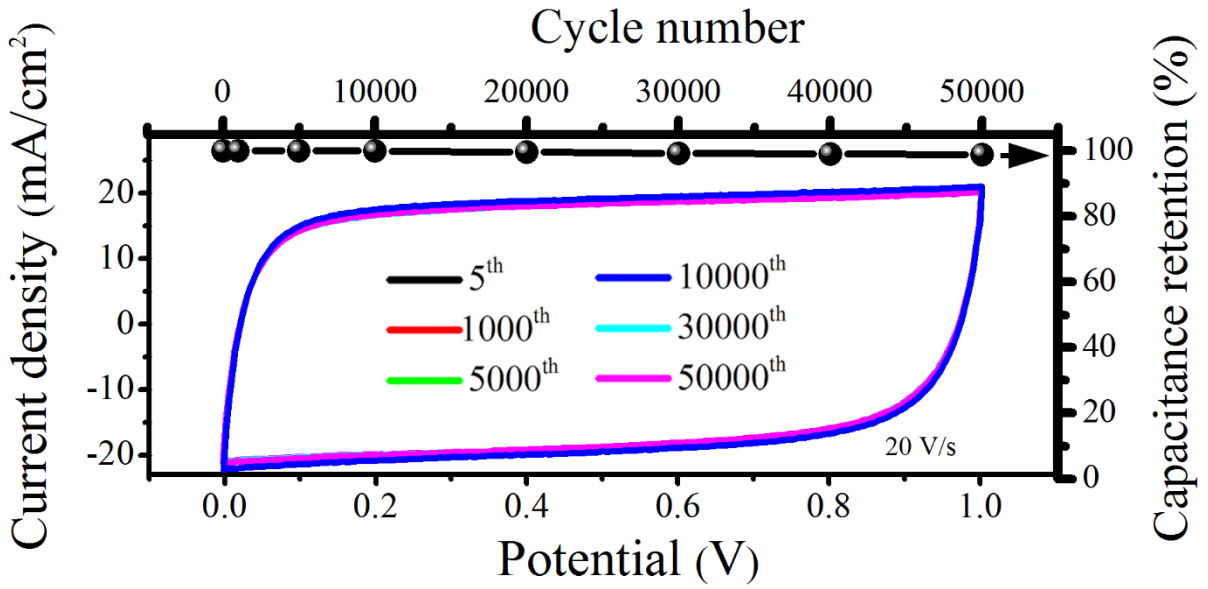

Figure 5-18 Cycling stability test of EPAM40@SnO_2 electrodes based MSCs at a scan rate of 20 V s^{-1}. The inset shows the corresponding CV curves at 20 V s^{-1} after various cycle numbers.

On the other hand, the cyclic stability of MSCs is also critical for practical applications. We take the EPAM40@SnO_2 electrodes based MSCs as an example, the EPAM40@SnO_2 electrodes based MSC shows excellent cycling stability as a result of EPAMs serving as a mechanically robust supporting framework in the hybrid electrodes, which retain 98% of the initial performance after 50,000 charge/discharge cycles at a scan rate of 20 V s^{-1} (Figure 5-18).

The CV curves of EPAM40@SnO_2 electrodes based MSCs before and after 50000th cycle show almost no change. In addition, the surface morphology and structure of EPAM40@SnO_2 electrodes after consecutive charging-discharging process were maintained very well (Figure 5-19), indicating the promising structural stability of the honeycomb EPAM40@SnO_2 electrodes.

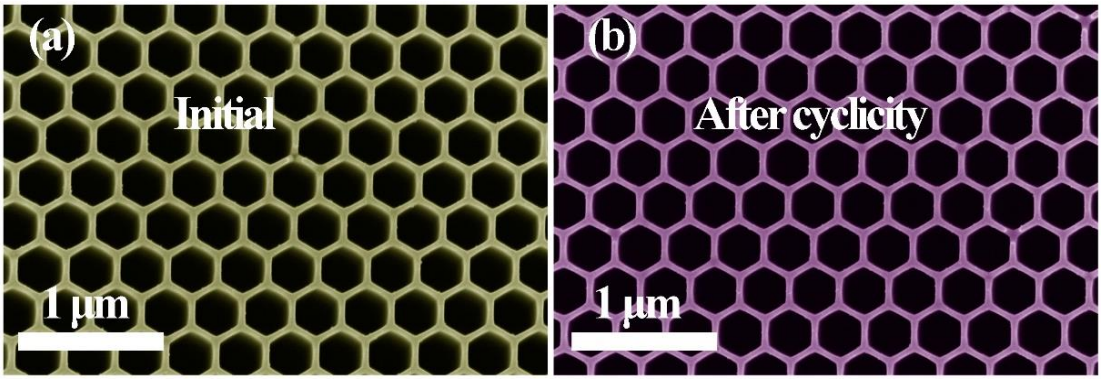

Figure 5-19 SEM images of EPAM40@SnO_2 electrode (a) before and (b) after 50000th cycle.

5.2.4 Mechanical stability of EPAM@SnO_2

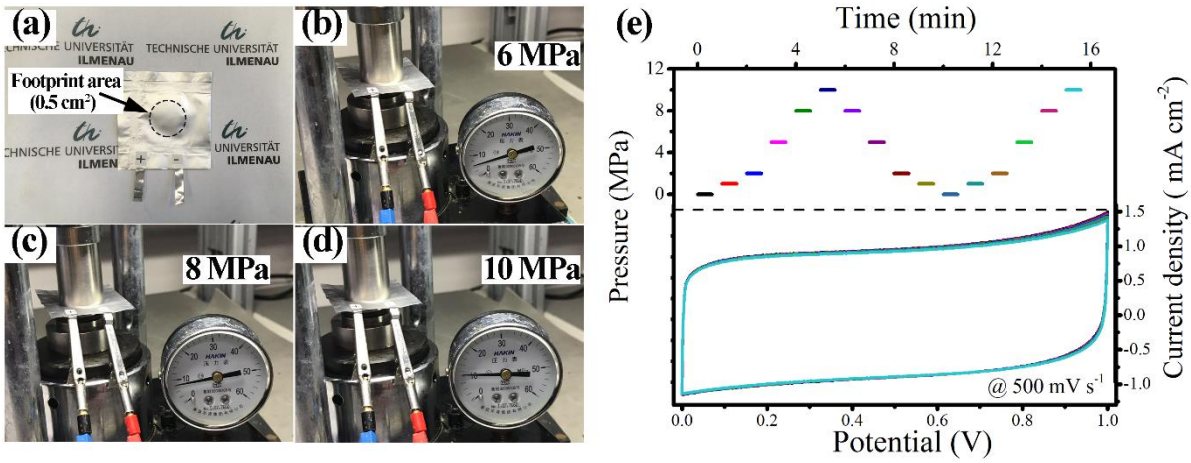

Figure 5-20 (a) Optical photo images of the pouch cell based on EPAM@SnO_2 electrodes, and the external extrusion pressure imposed on the pouch cell with (b) 6, (c) 8, and (d) 10 MPa. (e) In-situ CV curves of pouch cell under various external pressures.

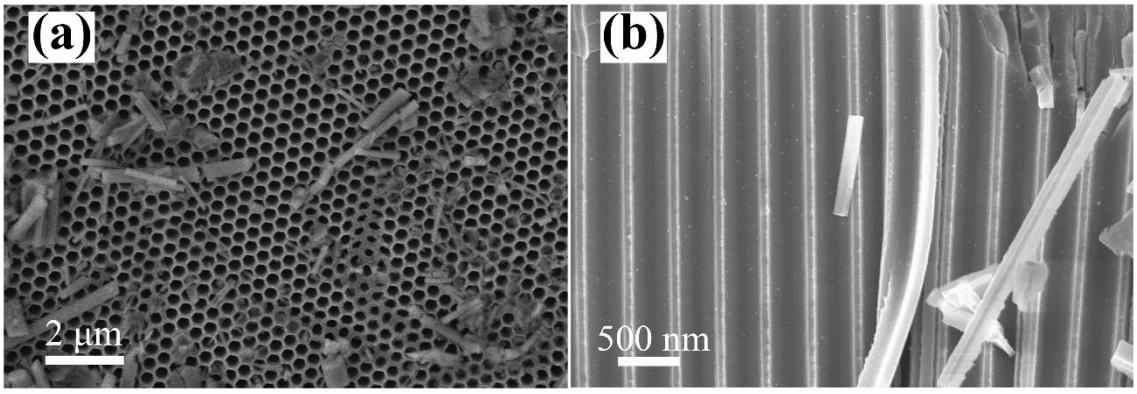

Figure 5-21 (a) Top- and (b) cross-sectional view SEM images of EPAM@SnO_2 electrodes after consecutively mechanical extrusion test.

In the previous section, the electrochemical characterization of EPAM@SnO_2 as electrode is systematically studied. In this section, the mechanical property of EPAM@SnO_2 (here, the pore-depth of the electrode is kept 25 μm) is explored, since the reliability of nanostructured electrodes under external stress is a big concern. To demonstrate its potential application under external mechanical stability during the device assembly, a soft package of symmetric SC (the pouch cell) is prepared with a pair of EPAM@SnO_2 electrodes using 1 M Na_2SO_4 as electrolyte, as shown in Figure 5-20a. The nanoarchitectured electrodes in the pouch cell should sustain severely external extrusion and maintain a normal electrochemical ability. The pouch cell is extruded under 0-10 MPa back and forth over several times by using the oil press system (Figure 5-20b-d). Specifically, the external stress is gradually loaded from 0 to 10 MPa and then the stepping sequence is repeated for several times. Meanwhile, the electrochemical performances for each stages were measured in-situ. As shown in Figure 5-20e, the measured CV curves at various extrusion intensities all delivered a rectangle shape and remained the same. This work demonstrates that the EPAM@SnO_2 possesses a high mechanical stability and can sustain high intensity stress mainly due to the honeycomb structure of EPAM. Furthermore, the SEM images (Figure 5-21) reveal that the EPAM@SnO_2 electrodes still remain the original nanoporous features after the electrochemical test under the continuous mechanical extrusion. Note that the residues in Figure 5-21a is the residual glass fibers from a glass microfiber filter that was used

as separator, and partials of the glass microfiber filter were damaged and fallen off during the disassembly of the EPAM@SnO_2//EPAM@SnO_2 device. This result further reveals the excellent mechanical stability of the EPAM that can efficiently sustain the mechanical extrusion pressure during the device assembly process to maintain the integrality of the nanoelectrodes. Overall, the excellent electrochemical performance and the superior structural stability verify the great capability of EPAM@SnO_2 as desirable nanoarchitectured current collectors to design nanoelectrodes for MSC.

5.3 Construction of pseudocapacitive nanoelectrodes based on EPAM@SnO_2 nanoarchitectured current collector for micro-supercapacitors

In this section, the pseudocapacitive nanoelectrodes based on the EPAM@SnO_2 as nanoarchitectured current collectors were constructed for realizing MSCs with high areal energy and power performance.

5.3.1 Structural and morphological characterizations for EPAM@SnO_2@MnO_2 electrode

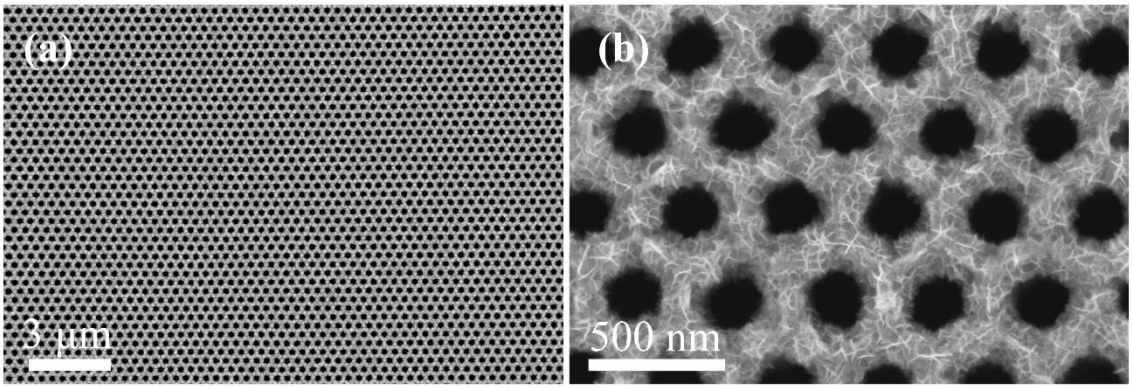

Figure 5-22 Typical top-view SEM images of EPAM@SnO_2@MnO_2 electrode: (a) low and (b) high magnification.

The EPAM@SnO_2 as nanoarchitectured current collector was firstly employed to electrochemically deposit a thin layer of MnO_2 materials. The uniformity of the resultant EPAM@SnO_2@MnO_2 over large scales can be demonstrated in Figure 5-22a. As shown in Figure 5-22b, the pore diameter of EPAM@SnO_2@MnO_2 electrode changed from the initial of

360 nm to 200 nm after the deposition of the MnO_2. Obviously, the hybrid structure maintains the highly oriented nanoporous structure as the original honeycomb structure of the EPAM@SnO_2. Besides, there are no blockage for the channels or defects on the surface of EPAM@SnO_2@MnO_2 electrode.

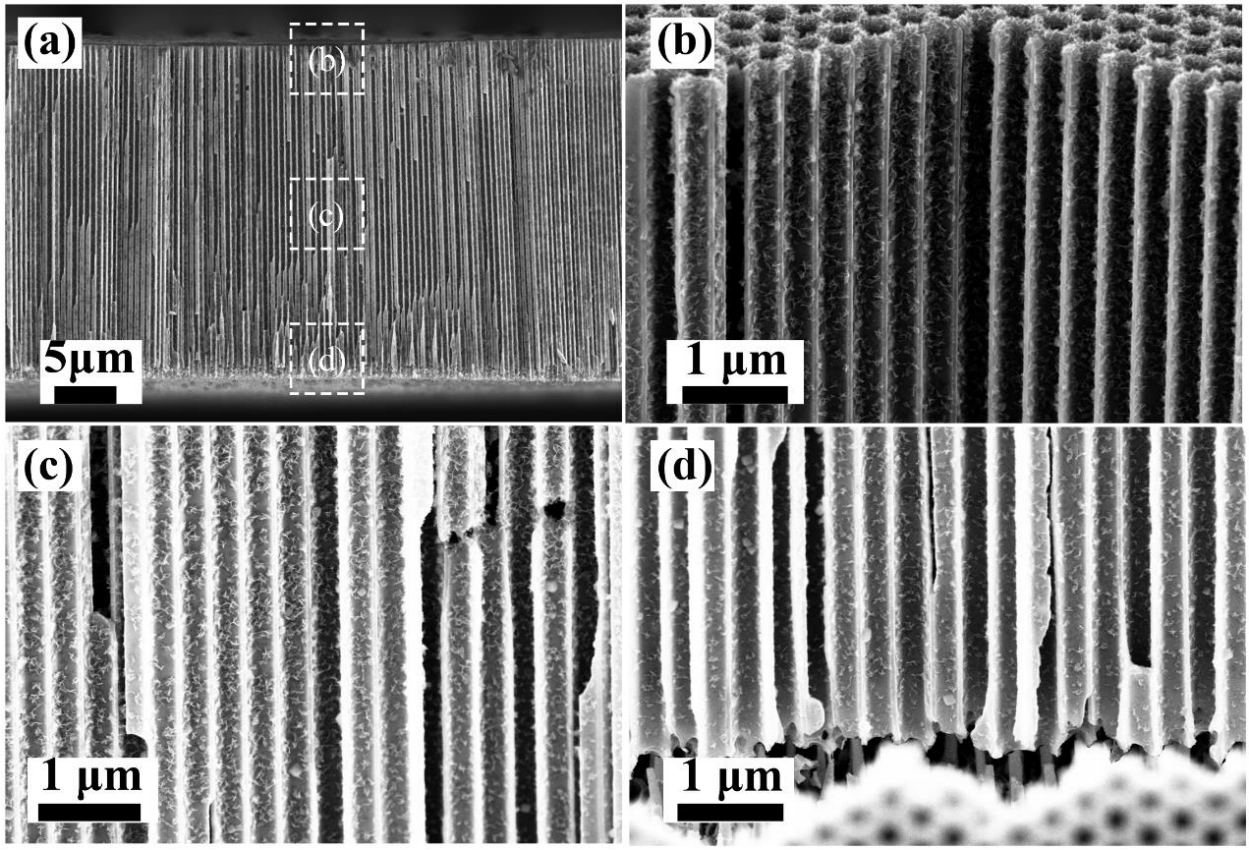

Figure 5-23 Cross-sectional SEM images of EPAM@SnO_2@MnO_2 electrodes. (a) Overall view of EPAM@SnO_2@MnO_2 electrode with an EPAM pore-depth of 25 μm, and corresponding high-resolution SEM image recorded from the region marked in (b), (c) and (d).

Figure 5-23a shows the cross-sectional SEM image of EPAM@SnO_2@MnO_2 with 25-μm-pore-depth EPAM, confirming the straight and stable porous structure after coating MnO_2 on the pore wall of EPAM@SnO_2. The detailed cross-sectional SEM images of different positions (Figure 5-23b-d) of EPAM@SnO_2@MnO_2 imply that the MnO_2 layers are conformally grown along with the straight channels of the porous structure. It is also worth mentioning that the layer thickness of MnO_2 in the upper, middle, and bottom parts of EPAM@SnO_2@MnO_2

electrode remains the same, demonstrating the uniformly deposited MnO_2 layer inside of the high-aspect ratio channels of the porous architecture. Such a highly oriented nanoporous structure (which remains so even after being coated with MnO_2) can promote the transport of electrolyte ions and improve the rate capability of MSCs.

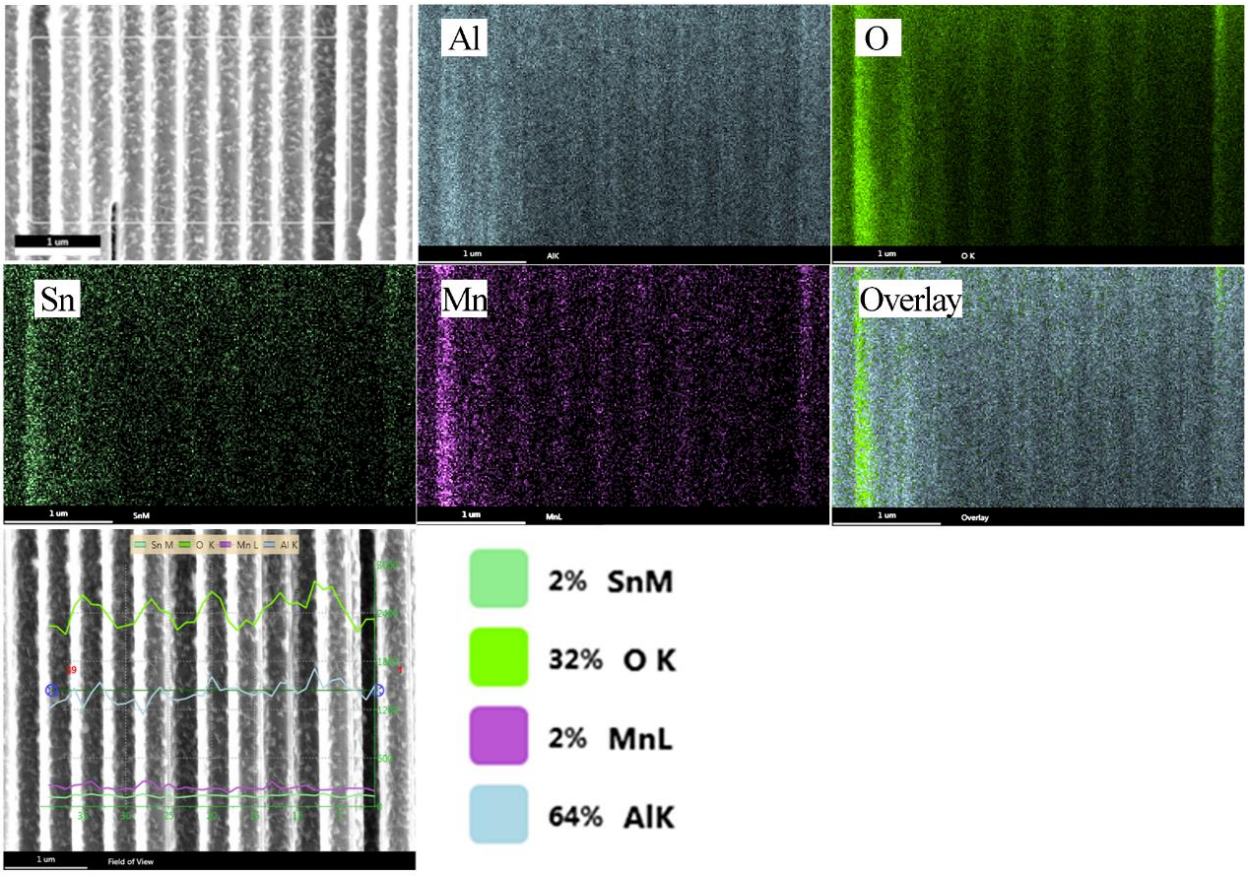

Figure 5-24 Cross-sectional EDX mapping and EDX line-scan of the cross-sectional view of EPAM@SnO_2@MnO_2 electrode, showing a well distribution profiles of Al, O, Sn, and Mn elements.

The element mapping images of EDX (Figure 5-24) in the selected cross-sectional SEM image demonstrate the overlapping of Al, O, Sn and Mn with even distribution over the entire nanochannels. An EDX line-scan recorded along the radial direction of several straight channels shows that the periodic distribution profiles of Sn (light green curve), O (green curve), Mn (purple curve) and Al (cyan curve) elements perfectly fits the arrangement of the channel arrays,

respectively. Species and content of elements for the EPAM@SnO_2@MnO_2 electrode are 2 % (Sn), 32% (O), 2% (Mn) and 64% (Al), respectively.

5.3.2 Electrochemical performance of EPAM@SnO_2@MnO_2//EPAM@SnO_2@MnO_2 micro-supercapacitors

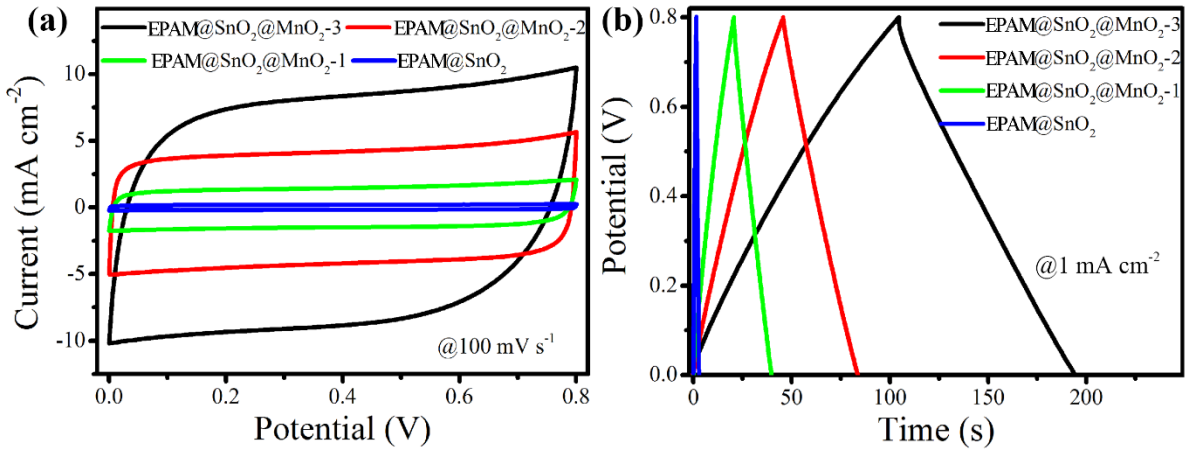

Figure 5-25 (a) CV and (b) GCD curves of the MSCs based on the symmetric EPAM@SnO_2@MnO_2 electrodes with various structural parameters. Note that the EPAM@SnO_2@MnO_2-1, EPAM@SnO_2@MnO_2-2, and EPAM@SnO_2@MnO_2-3 are the electrodes with 5, 16, and 25-μm-pore-depth, respectively.

MSCs with symmetric device configuration were assembled through stacking two same EPAM@SnO_2@MnO_2 electrodes separated by a glass microfiber filter and with 1.0 M Na_2SO_4 aqueous solution as electrolyte. The EPAM@SnO_2@MnO_2 electrodes with various pore-depths were chosen. In order to keep the pore size of each electrode the same, the mass loadings of MnO_2 were precisely tuned. Specifically, the mass loadings of MnO_2 are 0.11, 0.43, and 0.65 mg cm^{-2} for EPAM@SnO_2@MnO_2 electrodes with pore-depths of 5, 16, and 25 μm, respectively. Figure 5-25a is the CV curves of the assembled EPAM@SnO_2@MnO_2//EPAM@SnO_2@MnO_2 MSCs over a wide range of scan rates from 2 to 500 mV s^{-1} in a potential range of 0–0.8 V. Obviously, the CV curves at different scan rates exhibit a symmetrically rectangular shape, indicating an ideally capacitive behavior and fast

charge–discharge characteristics of MSCs. The GCD curves of EPAM@SnO_2@MnO_2//EPAM@SnO_2@MnO_2 MSCs at different current densities are shown in Figure 5-25b. These charging curves are very symmetric to the discharge counterparts, again indicating the excellent capacitive behaviors in MSCs.

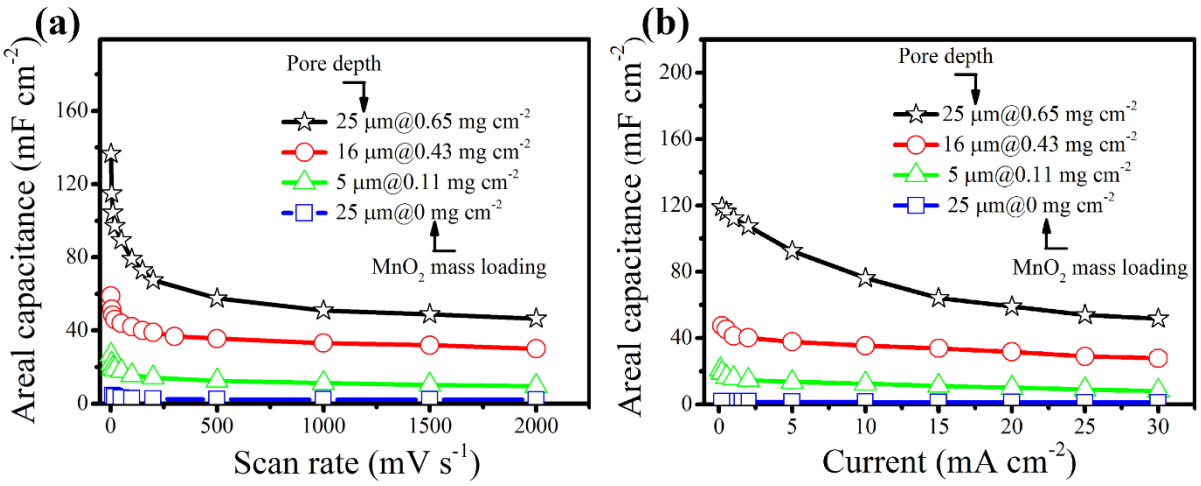

Figure 5-26 Device areal capacitance as a function of (a) scan rates and (b) current densities of EPAM@SnO_2@MnO_2//EPAM@SnO_2@MnO_2 MSCs, respectively.

When depositing MnO_2, the layer thickness of MnO_2 was kept the same in all EPAM@SnO_2@MnO_2 electrodes, thus electrodes with deeper EPAM have higher MnO_2 mass loading. Figure 5-26 illustrates the device areal capacitance of MSCs with different pore-depths of EPAM@SnO_2@MnO_2 electrode as a function of scan rates and current densities. The device capacitance depends strongly on the pore-depth of original EPAM and the subsequent changes of MnO_2 mass loading of EPAM@SnO_2@MnO_2 electrodes. For EPAM@SnO_2@MnO_2 electrodes consisting of 25-μm-pore-depth EPAM, the MnO_2 mass loading was 0.65 mg cm^{-2}, consequently resulting in highest device capacitance of 137 mF cm^{-2} at a scan rate of 2 mV s^{-1} (Figure 5-26a), and 121 mF cm^{-2} at a current density of 0.2 mA cm^{-2} (Figure 5-26b). Benefiting from the vertically-aligned nanoporous structure features, these symmetric stacked MSCs have good rate performance, *i.e.*, the capacitance of MSCs based on EPAM@SnO_2@MnO_2

electrodes with 25-μm-deep EPAM remains to be 47 mF cm^{-2} when the scan rate increasing from 10 to 2,000 mV s^{-1}.

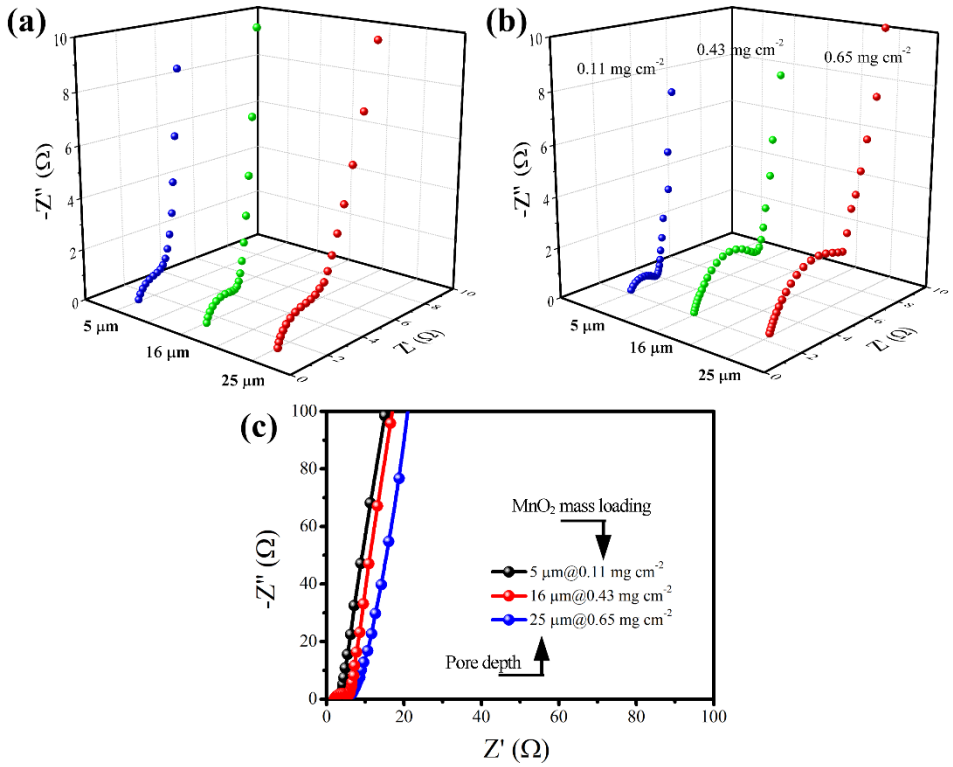

Figure 5-27 Nyquist plots of (a) EPAM@SnO_2//EPAM@SnO_2, and (b) EPAM@SnO_2@MnO_2//EPAM@SnO_2@MnO_2 MSCs with different pore-depths of EPAM. (c) Warburg region of the EPAM@SnO_2@MnO_2//EPAM@SnO_2@MnO_2 MSCs with different pore-depths of EPAM.

It can be concluded from Figure 5-26 that the negligible capacitance (< 4 mF·cm^{-2}) of EPAM@SnO_2//EPAM@SnO_2 MSCs, in which the pore-depth of EPAM in all electrodes was 25 μm, suggests the function of SnO_2 layer in EPAM@SnO_2 based pseudocapacitive electrodes mostly for charge transport rather than charge storage. Furthermore, EIS was performed in order to clearly understand the role of EPAM@SnO_2 as nanoarchitectured current collectors. Figure 5-27a is the Nyquist plot of EPAM@SnO_2//EPAM@SnO_2 MSCs with different pore-depth of original EPAM (*i.e.*, 5, 16 and 25 μm, respectively). Apparently, there is a significant raise in R_{ct} for these MSCs. The gradually increased R_{ct} should be the inevitable result arising from the

limited electrical conductivity of SnO_2, which is much lower than that of metals. The intrinsic electrical resistance of SnO_2 leads the total resistance of EPAM@SnO_2//EPAM@SnO_2 MSCs to be progressively increased accompanying with EPAM pore-depth increase, and then consequently results in an increase in R_{ct}. With respect to the Nyquist plots for EPAM@SnO_2@MnO_2//EPAM@SnO_2@MnO_2 MSCs (Figure 5-27b), they have the same trend as those of EPAM@SnO_2//EPAM@SnO_2 MSCs, which have the similar ESR but the increased R_{ct}. The similar ESR suggests the negligible influence on the series bulk resistance with the use of EPAM@SnO_2 as nanoarchitectured current collectors. Besides the increased electrical resistance in EPAM@SnO_2 current collectors, the gradual raise in R_{ct} of EPAM@SnO_2@MnO_2//EPAM@SnO_2@MnO_2 MSCs should be due to the low intrinsic conductivity of MnO_2. The low conductive MnO_2 layer makes the charge transport in EPAM@SnO_2@MnO_2 electrodes mainly rely on the conductive SnO_2 layer, which results in the exclusive pathway for charge transportation.

Furthermore, fast ion transport at the interface between electrode and electrolyte could be evident by the Warburg region. In the low frequency region (Figure 5-27c), all the EPAM@SnO_2@MnO_2//EPAM@SnO_2@MnO_2 MSCs exhibit an almost vertical line, representing the promising permeability for electrolyte infiltration and ion diffusion to access the surface of pseudocapacitive materials.

5.3.3 Structural and morphological characterizations for EPAM@SnO_2@PPy electrode

The SEM image in Figure 5-28a shows that the porous EPAM@SnO_2@PPy electrode has a hexagonal honeycomb pattern, inherited from the EPAM structure. The uniform and highly-ordered of the EPAM@SnO_2@PPy electrode in large scale with defect-free and crack-free surface are clearly evident. The corresponding high-resolution SEM image (Figure 5-28b) shows a wall thickness of 100 nm for the hybrid electrode after coating of PPy layer, while the

EPAM@SnO_2 nanoarchitectured current collector has a uniform wall thickness of 40 nm. Therefore it reveals that the coating layer of PPy is 30 nm.

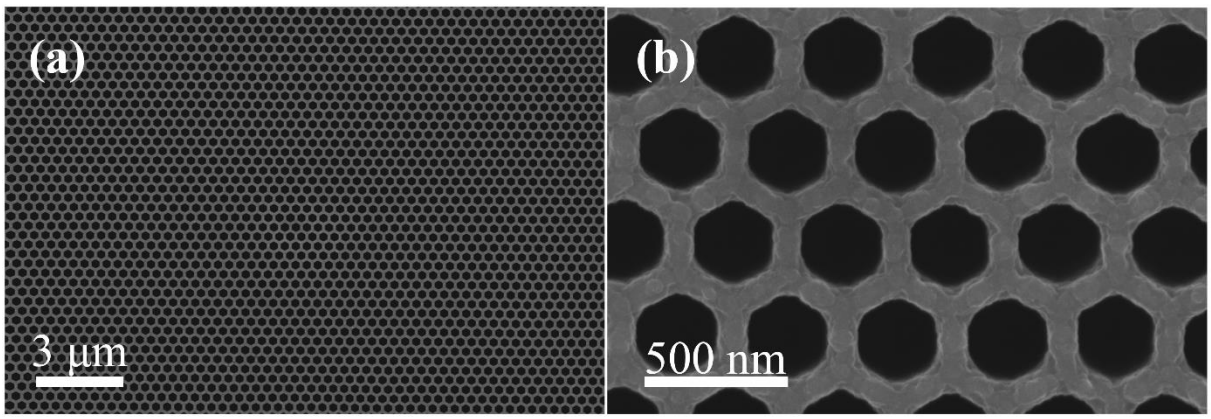

Figure 5-28 (a) Low- and (b) high-magnification SEM images of the EPAM@SnO_2@PPy electrode.

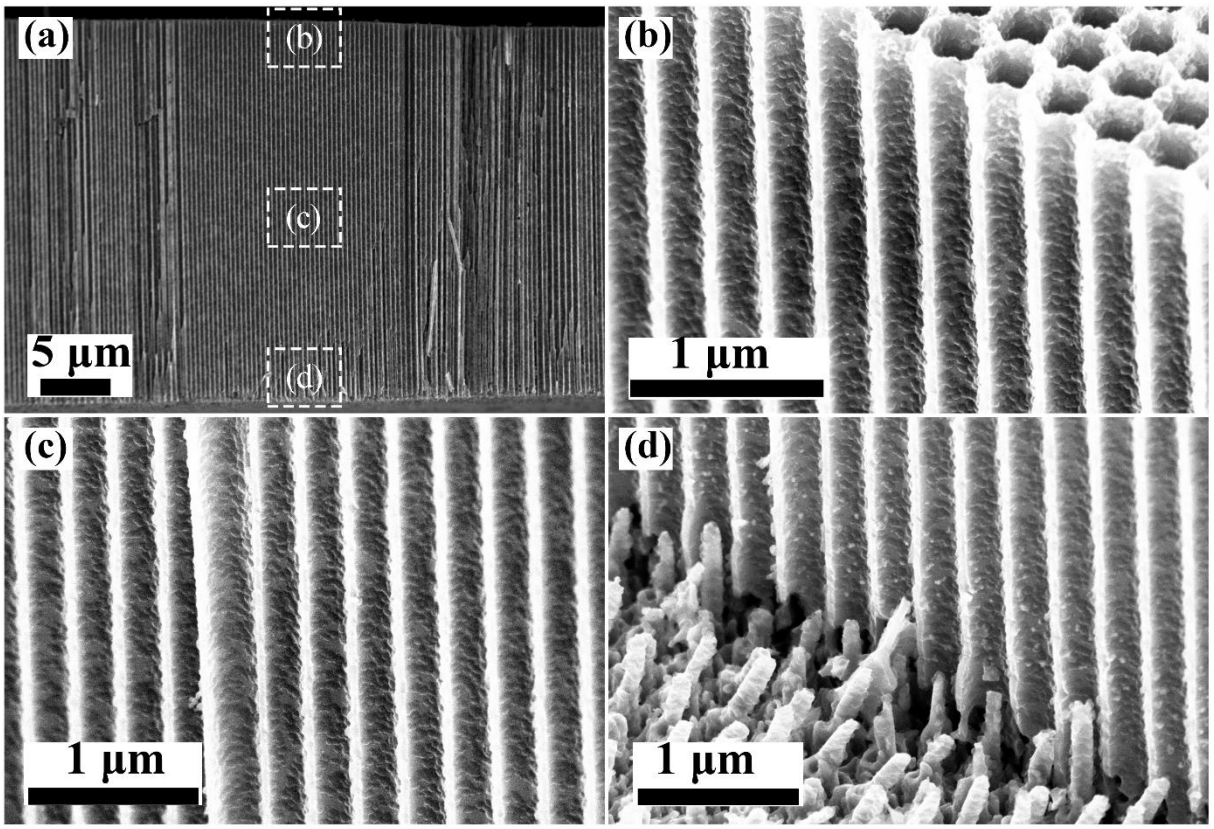

Figure 5-29 Cross-sectional SEM images of EPAM@SnO_2@PPy electrode. (a) Overall view of EPAM@SnO_2@PPy electrode with pore-depth of 25 μm, and corresponding high-resolution SEM image recorded from the boxed area marked in (b), (c) and (d).

The cross-sectional over-view SEM image of EPAM@SnO_2@PPy electrode under low magnifications is shown in Figure 5-29a, depicting that the channels are straight and well-aligned from top to bottom, with a typical height of ~25 μm. Figure 5-29b-d display the detailed geometric morphology of PPy layer inside of the channel, where uniform channels conformally coated with rough layer can be clearly observed, similar to the morphology of the EPAM@SnO_2@MnO_2 electrodes. Notably, the PPy nanolayer was uniformly grown inside the channels over the entire nanoporous channels, as can be demonstrated from the upper, middle, and bottom parts of the cross-sectional electrode.

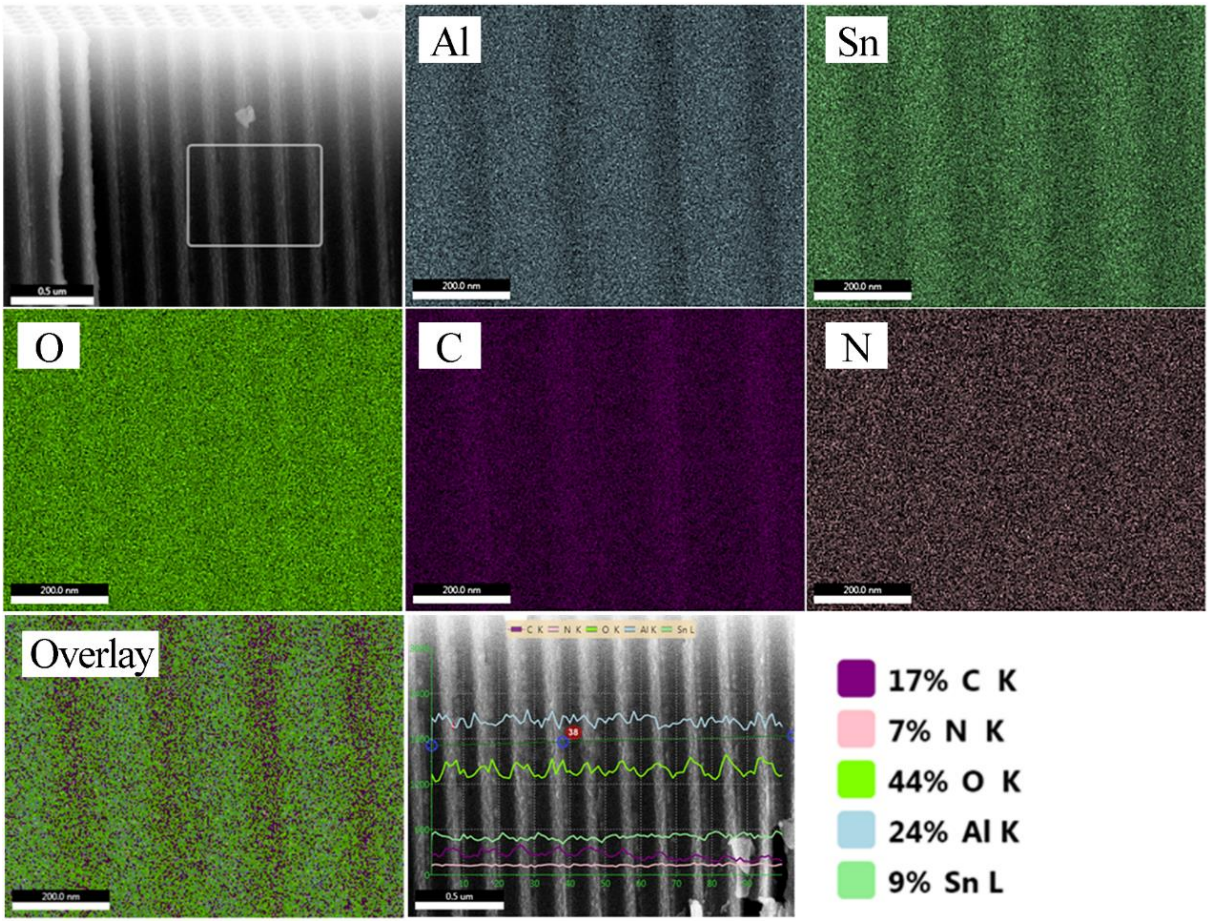

Figure 5-30 Cross-sectional EDX mapping and EDX line-scan of the cross-section of EPAM@SnO_2@PPy electrode, showing a well distribution profiles of Al, Sn, O, C, and N elements.

The uniform distribution of PPy nanolayer can be further confirmed by the EDX mapping recorded at the cross-sectional electrode in Figure 5-30. The element composition of the EPAM@SnO_2@PPy electrode shows the overlapping areas of Al (cyan), O (green), Sn (light green), C (purple) and N (pink) with uniform distribution along the nanochannels. The EDX line-scan shows that the periodically-distributed curves of Al (cyan curve), Sn (light green curve), O (green curve), C (purple curve) and N (pink curve), respectively. The contents of elements in the EPAM@SnO_2@PPy electrode are 9 % (Sn), 44% (O), 17% (C), 7% (N) and 24% (Al), respectively.

5.3.4 Electrochemical performance for EPAM@SnO_2@PPy//EPAM@SnO_2@PPy micro-supercapacitors

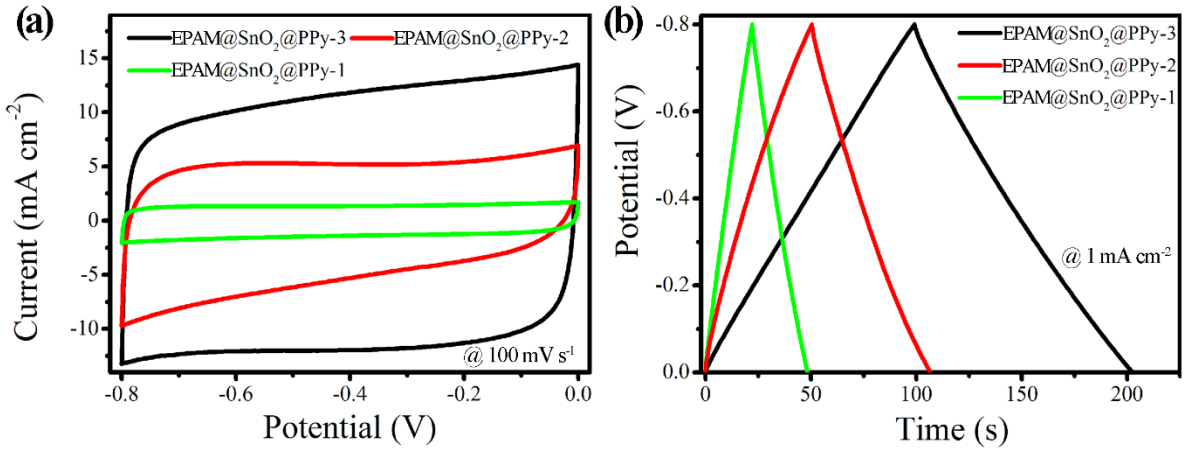

Figure 5-31 (a) CV and (b) GCD curves of the EPAM@SnO_2@PPy//EPAM@SnO_2@PPy MSCs with various structural parameters. Note that the EPAM@SnO_2@PPy-1, EPAM@SnO_2@PPy-2, and EPAM@SnO_2@PPy-3 are the electrodes with 5, 16, and 25-μm-pore-depth, respectively.

The EPAM@SnO_2@PPy//EPAM@SnO_2@PPy MSCs have the similar electrochemical performance to that of EPAM@SnO_2@MnO_2//EPAM@SnO_2@MnO_2 MSCs except the different operating potential window that is from -0.8 to 0 V. EPAM@SnO_2@PPy electrodes with three different pore-depths, *i.e.*, 5, 16, and 25 μm, are adopted, of which the corresponding

PPy mass loadings are 0.21, 0.83, and 1.32 mg cm^{-2}, respectively. Figure 5-31 outlines the CV and GCD curves of the EPAM@SnO_2@PPy//EPAM@SnO_2@PPy MSCs. The CV and GCD curves all display a quasi-rectangular shape and isosceles triangle shape, respectively, indicating an ideal capacitive behavior of MSCs.

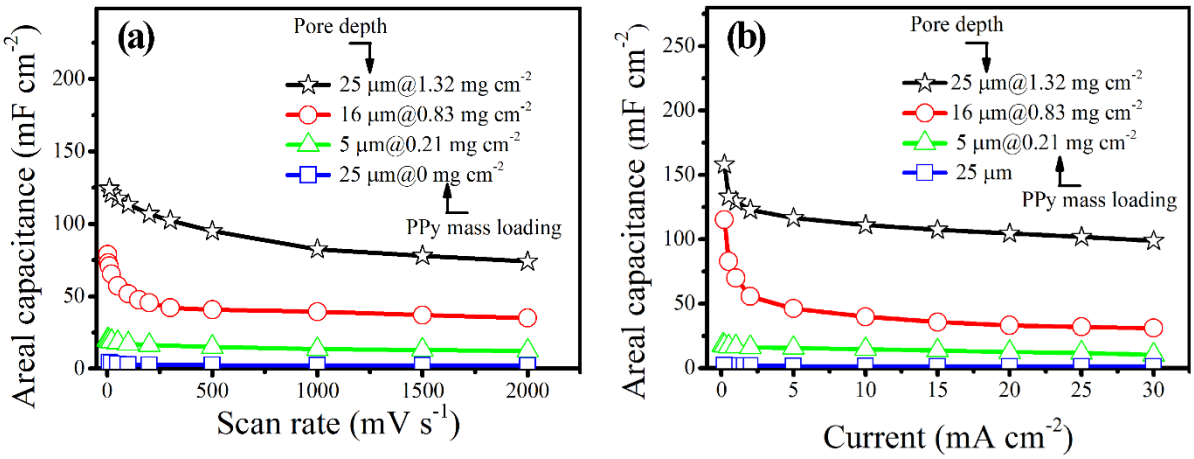

Figure 5-32 Device areal capacitance as a function of (a) scan rates and (b) current densities of EPAM@SnO_2@PPy//EPAM@SnO_2@PPy MSCs, respectively.

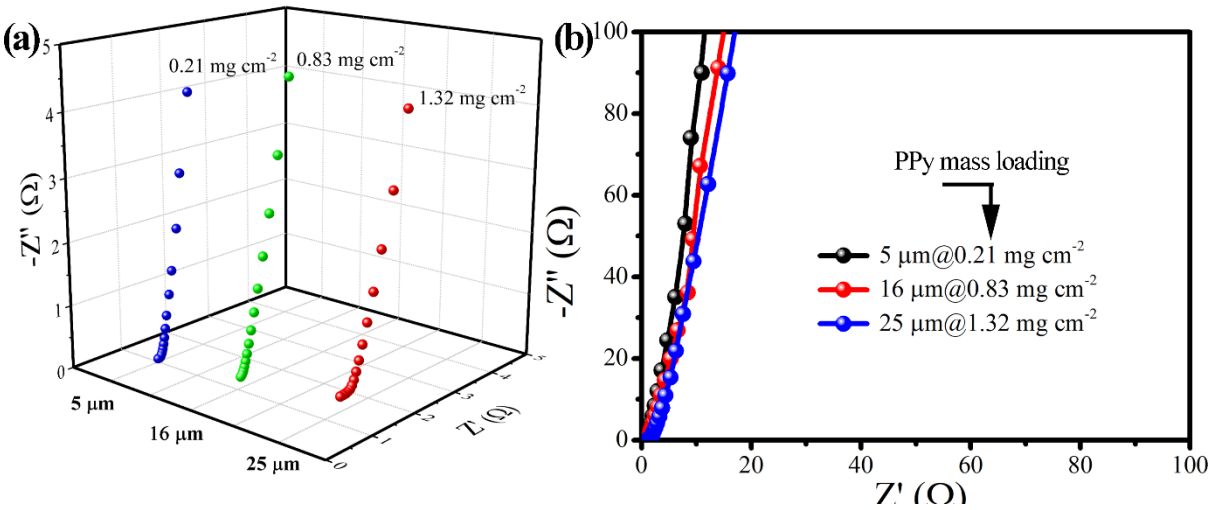

Figure 5-33 (a) Nyquist plots and (b) Warburg region of EPAM@SnO_2@PPy//EPAM@SnO_2@PPy MSCs with different pore-depths of original EPAM.

Figure 5-32 demonstrates the device areal capacitance of MSCs with different pore-depths of EPAM@SnO_2@PPy electrode as a function of scan rates and current densities. The device

capacitance depends strongly on the pore-depths of original EPAM and the subsequent changes of PPy mass loading of EPAM@SnO_2@PPy electrodes. For EPAM@SnO_2@PPy electrodes consisting of 25-μm-pore-depth based EPAM, the maximum device capacitance of EPAM@SnO_2@PPy//EPAM@SnO_2@PPy MSCs reaches 124 $mF \cdot cm^{-2}$ at a scan rate of 10 $mV \cdot s^{-1}$ (158 $mF \cdot cm^{-2}$ at a current density of 0.2 $mA \cdot cm^{-2}$). Thanks to the vertically-oriented nanoporous structure properties, these EPAM@SnO_2@PPy//EPAM@SnO_2@PPy MSCs have good rate performance, *i.e.*, the capacitance of MSCs with 25-μm-deep EPAM remains to be 75 $mF \cdot cm^{-2}$ when the scan rate increasing to 2,000 $mV \cdot s^{-1}$.

Figure 5-33a shows the Nyquist plots of EPAM@SnO_2@PPy//EPAM@SnO_2@PPy MSCs in the high frequency region. All MSCs have the similar ESR and slightly increased R_{ct} along with the pore-depths of the electrodes. Particularly, the R_{ct} values for EPAM@SnO_2@PPy//EPAM@SnO_2@PPy MSCs with the electrodes pore-depth of 5, 16 and 25 μm are 0.2, 0.4, and 0.9 Ω, respectively, which are much smaller than that of the EPAM@SnO_2//EPAM@SnO_2 and EPAM@SnO_2@MnO_2//EPAM@SnO_2@MnO_2 MSCs with the same structure parameters. This is mainly because the highly conductive PPy layer could not only store charges but also partially contribute to the charge transport for improving the charge transport efficiency in EPAM@SnO_2@PPy electrodes, resulting in lower R_{ct} of EPAM@SnO_2@PPy//EPAM@SnO_2@PPy MSCs. On the other hand, as shown in the Warburg region at low frequency (Figure 5-33b), all the EPAM@SnO_2@PPy//EPAM@SnO_2@PPy MSCs display a nearly vertical line, revealing the fast ion diffusion inside the MSCs.

5.3.5 Asymmetric micro-supercapacitors of EPAM@SnO_2@MnO_2//EPAM@SnO_2@PPy

Generally, the energy and power densities of SCs are restricted by the use of pseudocapacitive materials with a narrow potential window. An asymmetric device configuration affords the opportunity for the expansion of the operating potential window of MSCs, and subsequently accomplishes the enhanced energy and power densities. Asymmetric MSCs were therefore

assembled by using EPAM@SnO_2@MnO_2 as positive electrode and EPAM@SnO_2@PPy as negative electrode. The two electrodes were stacked together with a glass microfiber filter as separator and 1.0 M Na_2SO_4 aqueous solution as electrolyte. As the aforementioned symmetric MSCs, the footprint of EPAM@SnO_2@MnO_2//EPAM@SnO_2@PPy MSCs was also 0.5 cm^2. Figure 5-34 graphically illustrates the design concept of the asymmetric device taking advantage of the unique structural merits of porous structure, including robust structural controllability, high stability, large aspect ratio and straight nanochannels, etc.

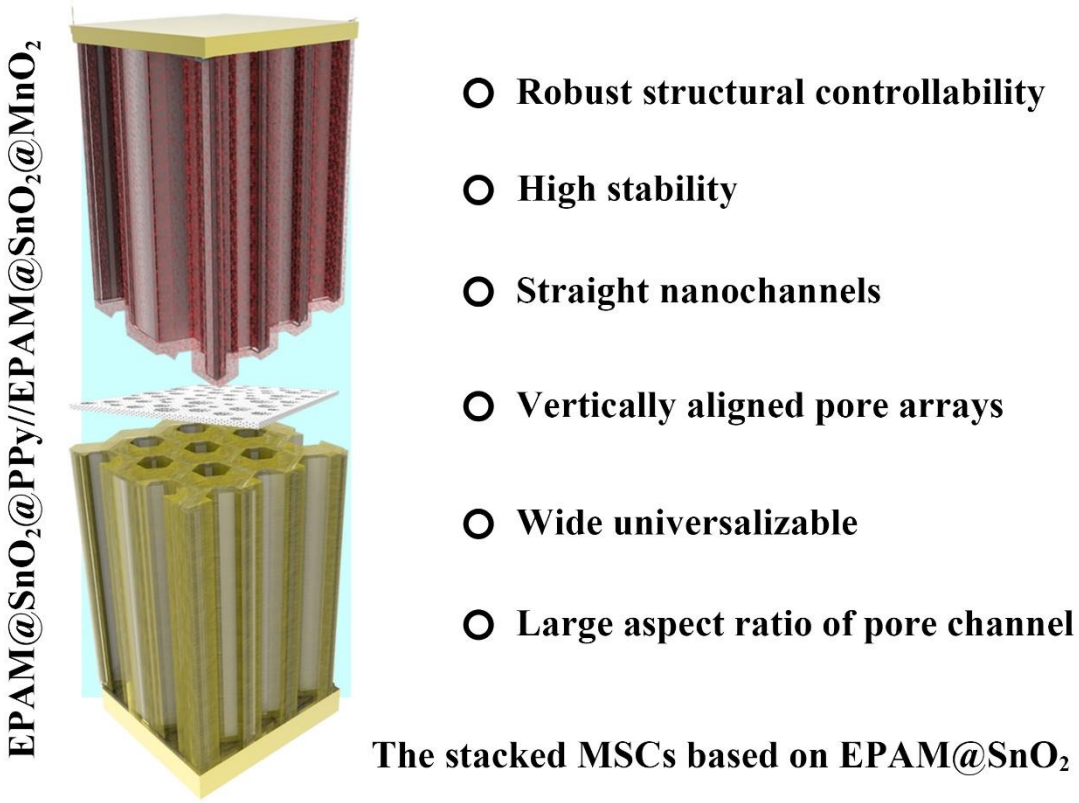

Figure 5-34 Graphical illustration of the design concept of the asymmetric MSCs.

Note that a charge balance between the two electrodes was accomplished by controlling the deposition time of MnO_2 at the positive electrode and the thickness of the PPy film at the negative electrode.

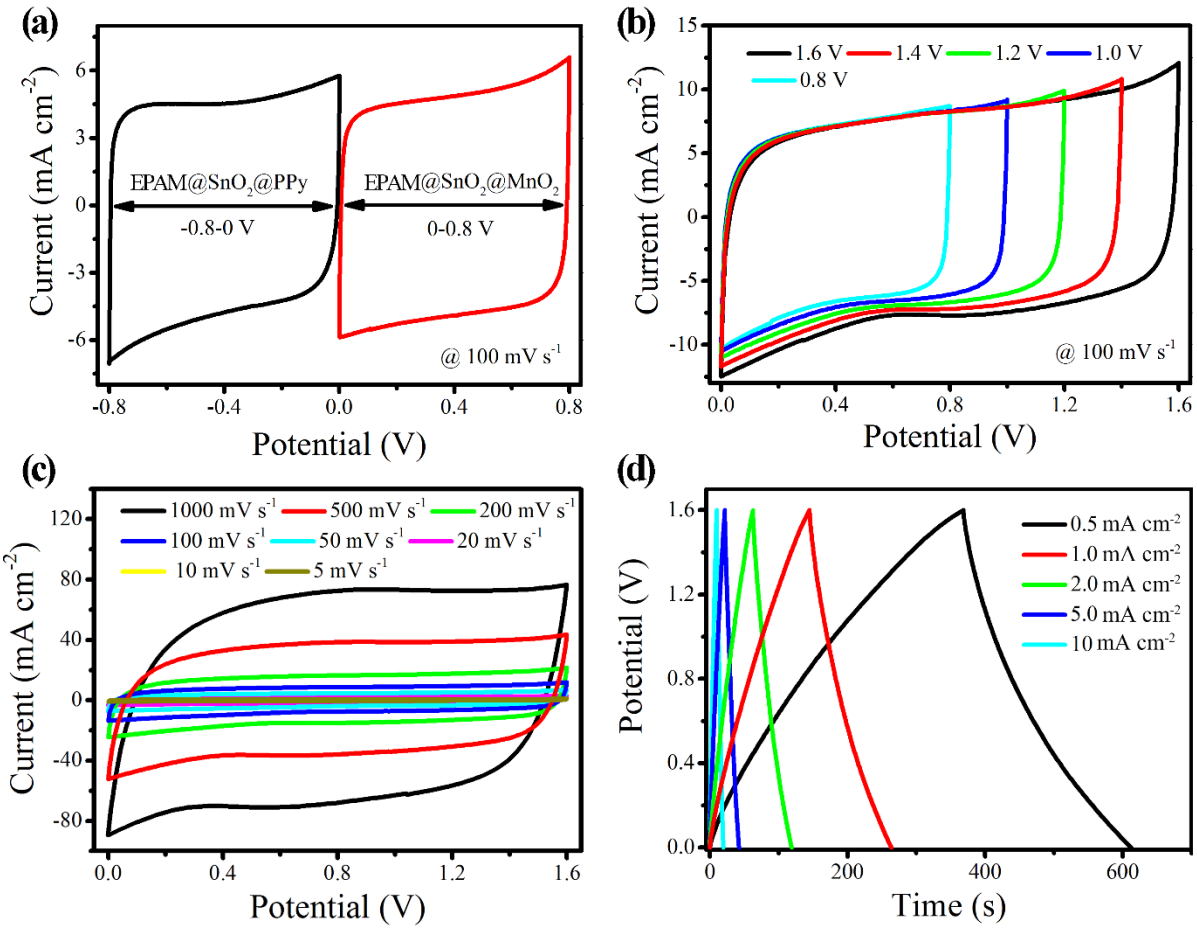

Figure 5-35 Electrochemical performance of EPAM@SnO_2@MnO_2//EPAM@SnO_2@PPy asymmetric stacked MSCs. (a) Typical CV curves of EPAM@SnO_2@MnO_2 and EPAM@SnO_2@PPy based symmetric MSCs, respectively, with 1.0 M Na_2SO_4 electrolyte. (b) CV curves within different potential ranges. (c) CV curves at different scan rates. (d) GCD profiles at different current densities.

Figure 5-35a outlines the working potential windows of each electrode based symmetric MSCs individually, -0.8 – 0 V for EPAM@SnO_2@PPy and 0 – 0.8 V for EPAM@SnO_2@MnO_2, so that the integration of both electrodes into single MSCs will result in an increased operating cell voltage up to 1.6 V. As shown in Figure 5-35b, the asymmetric MSCs with 16-µm-pore-depth EPAM in all electrodes work efficiently in the range from 0.8 to 1.6 V. Figures 5-35c and d are the corresponding CV and GCD curves of asymmetric MSCs in a potential range of 0 – 1.6 V, respectively. The nearly rectangular CV curves and the highly triangular charge-

discharge profiles reveal an ideally capacitive behavior and the fast charge-discharge characteristics of asymmetric MSCs. Particularly, the CV curves retain their rectangular shape without apparent distortions when increasing scan rates up to a high rate of 1,000 mV s^{-1}, indicating the extraordinary high-rate performance of asymmetric MSCs.

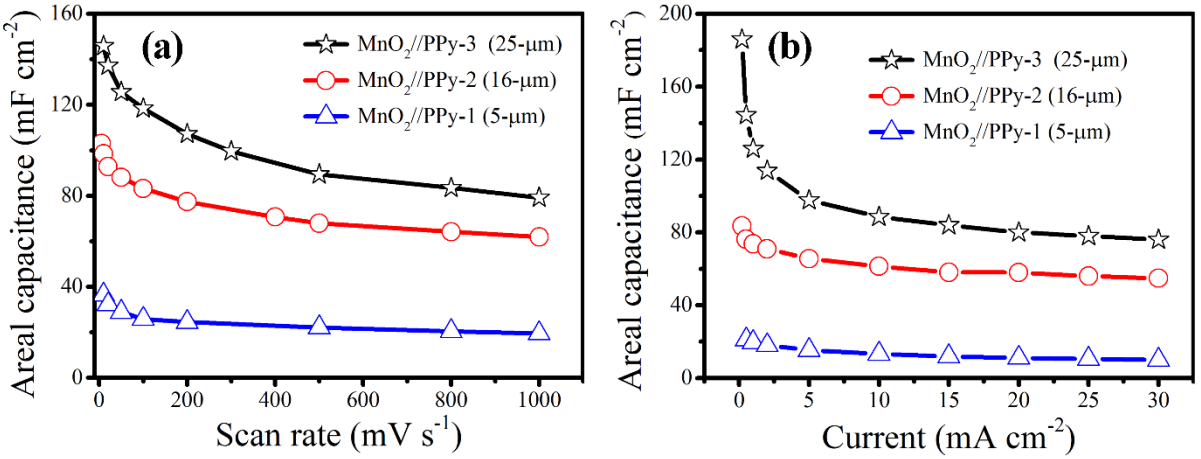

Figure 5-36 Device areal capacitance as a function of (a) scan rates and (b) current densities.

As the as-assembled asymmetric MSCs, the device capacitance also closely relies on the pore-depth of the original EPAM in electrodes as well as the corresponding mass loading of pesudocapacitive materials (Figure 5-36). For asymmetric MSCs based on positive and negative electrodes both with 25-μm-pore-depth EPAM, a highest device capacitance of 147 mF cm^{-2} has been achieved at a scan rate of 10 mV s^{-1} and still remain 80 mF cm^{-2} at the scan rate of 1,000 mV s^{-1} (Figure 5-36a). Besides, the maximum capacity of the same device could reach 186 mF cm^{-2} at a current density of 0.2 mA cm^{-2} (Figure 5-36b).

Besides the adoption of asymmetric device configuration, the utilization of ionic liquid electrolyte is another efficient approach to extend the operating potential window of MSCs. As shown in Figures 5-37a and b, the asymmetric device configuration coupled with the ionic liquid electrolyte (1.0 M EMIM-TFSI in ACN) enables the device to work efficiently in a potential range of 0 – 3.0 V. Figure 5-37c shows the device capacitance for varied current densities of asymmetric stacked MSCs in which the pore-depth of EPAM in all electrodes was

25 μm. The device capacitance reaches 128 mF cm^{-2} at a current density of 0.5 mA cm^{-2}, which is slightly lower than that with 1.0 M Na_2SO_4 aqueous electrolyte. When the current density is increased from 0.5 to 5 mA cm^{-2}, the capacitance drops to 93 mF cm^{-2} (72% retention) and it recovers to 123 mF cm^{-2} (96% retention) with the current density again being decreased to 0.5 mA cm^{-2}. In addition, the stacked asymmetric MSCs with ionic liquid electrolyte still exhibit remarkable cycling stability with 82.5% of initial capacitance at 20 mA cm^{-2} over a potential window of 0 – 3.0 V withstanding continued 10,000 cycles with high Coulombic efficiency of nearly 100% (Figure 5-37d).

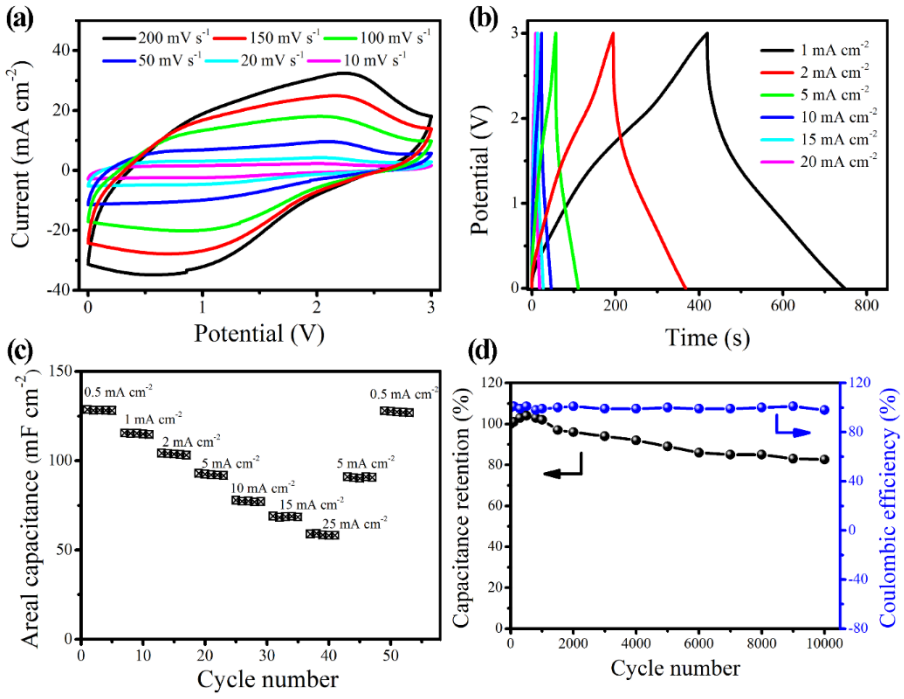

Figure 5-37 (a) CV curves at different scan rates, (b) GCD profiles at different current densities, (c) rate performance, and (d) cycling stability test at 20 mA cm^{-2} for 10000 times of EPAM@SnO_2@MnO_2//EPAM@SnO_2@PPy asymmetric MSCs with EMIM-TFSI electrolyte.

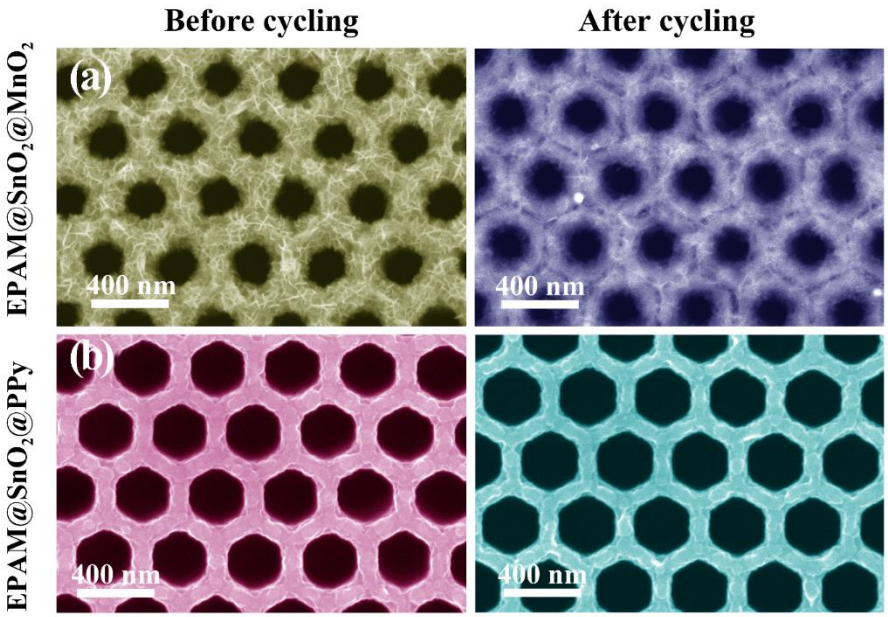

Figure 5-38 The morphological stability of EPAM-reinforced pseudocapacitive electrodes. SEM images of (a) EPAM@SnO_2@MnO_2 and (b) EPAM@SnO_2@PPy electrodes before (left) and after (right) cyclic test.

Furthermore, the surface morphology and structure of the positive electrode of EPAM@SnO_2@MnO_2 and the negative electrode of EPAM@SnO_2@PPy before and after 10,000th cycles of consecutive charging and discharging process are shown in Figure 5-38, which shows almost no change for these electrodes. The well intact of porous electrodes based on the robust mechanical stability of EPAM architecture is responsible for the long cycle performance of MSCs. It is noteworthy that the performance degradation is mainly arising from the small portion loss of MnO_2, as evidenced by the obvious morphological changes after cycling.

As it can be furthermore noted, the insufficient energy of MSCs is their crucial flaw compared with micro-batteries and remains a major challenge to be addressed. In the current electrodes design, four strategies have been combined together into stacked MSCs aiming to achieve high energy storage capability: (i) the utilization of pseudocapacitive materials with high specific capacitance in both positive and negative electrodes; (ii) the adoption of asymmetric device

configuration to extend the operating potential window of MSCs; (iii) the application of ionic liquid electrolyte to further widen the operating potential window of MSCs; and more importantly, (iv) the prominent nanoelectrode architecture design based on EPAM@SnO_2 nanoarchitectured current collector for both positive and negative electrodes.

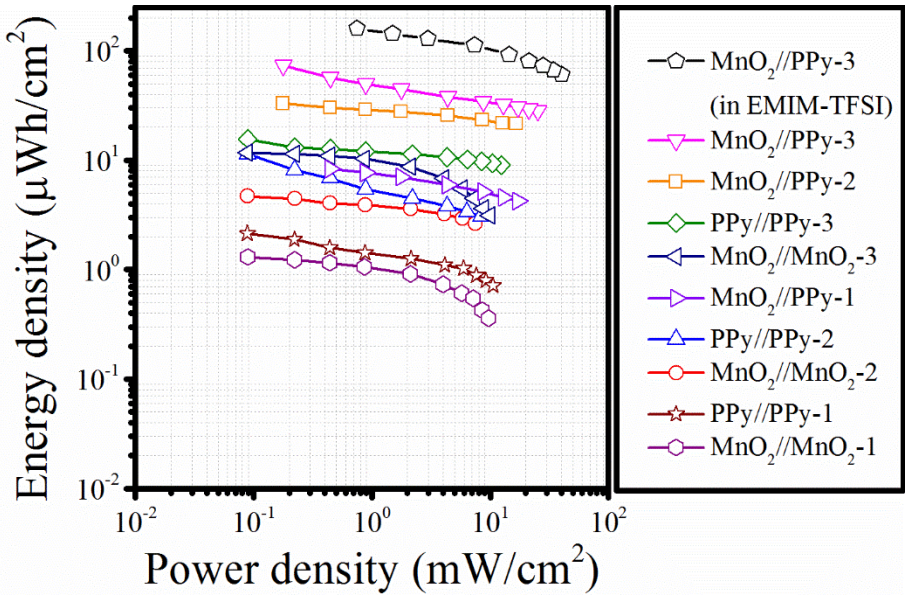

Figure 5-39 Ragone plots of energy and power density of a series of MSCs based on EPAM-reinforced nanoelectrodes. (Here, the MnO_2//PPy is short for EPAM@SnO_2@MnO_2//EPAM@SnO_2@PPy MSCs, and the Arabic number behind reply different pore-depth of EPAM, *e.g.*, MnO_2//PPy-1, MnO_2//PPy-2 and MnO_2//PPy-3 represent the asymmetric MSCs based on positive and negative electrodes with 5, 16, and 25-μm-deep EPAM, and the electrolyte utilized in these devises refers to the Na_2SO_4 aqueous solution, unless otherwise specified.)

Figure 5-39 compares the areal energy performance metrics of one representative EPAM@SnO_2@MnO_2//EPAM@SnO_2@PPy asymmetric stacked MSCs using EMIM-TFSI ionic liquid electrolyte, with other EPAM reinforced MSCs. The peak energy and power densities are 160 μWh cm^{-2} and 40 mW cm^{-2}, respectively. Although the replacement of 1.0 M Na_2SO_4 electrolyte with EMIM-TFSI ionic liquid electrolyte results in the slight decline in device capacitance, the widest operating potential range with EMIM-TFSI electrolyte assures

to achieve the highest energy and power densities among all the as-assembled stacked MSCs in this work. Remarkably, the energy storage performance of the asymmetric MSCs is among the best comprehensive performance of the reported stacked MSCs (Figure 5-40).[157, 167, 177-186] In particular, the peak energy density of the stacked asymmetric MSCs in this work is roughly fourfold that of the carbide-derived-carbons (CDC) based stacked MSCs (~40 μWh cm^{-2}) but with a similar peak power density.[177] Additionally, the areal energy density of the asymmetric MSCs with EMIM-TFSI electrolyte is even comparable with that of some state-of-the-art 3D micro-batteries but with much higher areal power density.[187-188]

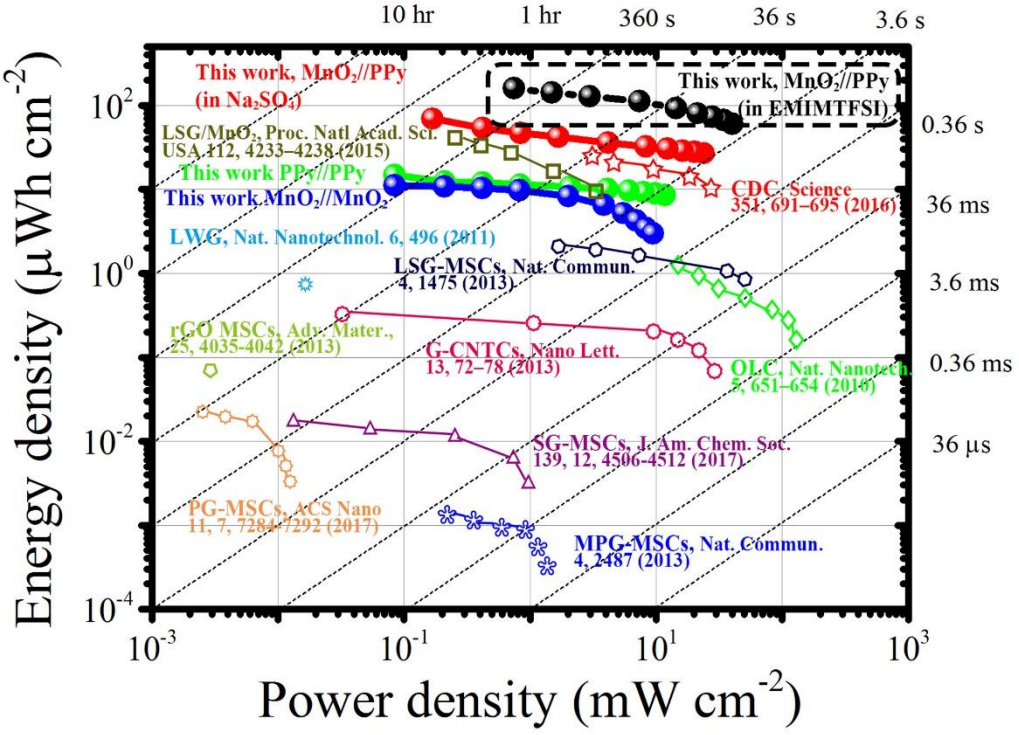

Figure 5-40 Ragone plots of EPAM@SnO_2@MnO_2//EPAM@SnO_2@PPy asymmetric MSCs compared with some reported MSCs.

5.4 Fabrication of non-aggregative and robust 1D pseudocapacitive nanoelectrode arrays with a large aspect ratio for micro-supercapacitors

5.4.1 The challenge for the conventional 1D nanoelectrodes

Among various nanostructured electrodes, arrayed 1D nanostructures (*i.e.*, nanowires and nanotubes) are usually taken as a typical example to demonstrate the advantages of nanostructured electrodes for MSCs, *e.g.*, larger specific surface area to provide ample electroactive sites for storing more charges, and shorter pathways to facilitate ionic and electronic transport for improving rate capability.[31, 34, 189-191] And yet, these advantages are on the premise that 1D nanoelectrode arrays are ideally erect and robustly stable. As is generally known, 1D nanoelectrode arrays suffer from the aspect ratio limit to maintain the erect feature. When the aspect ratio is above a certain value (*e.g.*, >10), arrayed 1D nanoelectrodes more tend to irreversibly self-aggregate into some clusters rather than retain erect.[123-124] As a result of the agglomeration of high-aspect-ratio 1D nanoelectrodes, the effective specific surface area of the whole electrode is decreased and meanwhile, the ionic transport resistance of the electrode is increased, both of which impose adverse effects on SC performance. Even though some approaches like freeze-drying and specific electric field radiation treatment have once been applied to alleviate the aspect ratio restriction issue for 1D nanostructure arrays, the results are still not satisfied.[192-195] Moreover, the structural stability is another crucial concern about practical applications of arrayed 1D nanoelectrodes because they have to be structurally stable enough to keep the original erect manner when they are assembled into a real SC device like MSC and also thereafter during the continued electrochemical reactions. Admittedly, arrayed 1D stubby nanoelectrodes are vertically-aligned and robustly stable, but the corresponding enhancement of specific surface area is rather limited compared to that of the planar electrode, which leads to the insignificant amount of performance improvement. Extending the length of every individual 1D stubby nanoelectrode is one way to dramatically improve the entire specific

surface area of arrayed 1D stubby nanoelectrodes, nevertheless, it will again result in the inevitable agglomeration of 1D nanoelectrodes arising from the high aspect ratio, which means that all issues have not been effectively tackled but repeat in an endless loop. So far, there is still a lack of an efficient solution to simultaneously address both the aspect ratio restriction and the mechanical instability to obtain non-aggregative and robust 1D nanoelectrode arrays.

Taking the NiNWs as an example, with electrochemical deposition of Ni into the nanopores of PAM templates attached on Ni substrate, nanowires will grow within the nanopores. Since the nanopores of PAM template are uniform in pore size (*i.e.*, 150 nm) and perpendicularly arranged with a hexagonal periodicity, the NiNWs embedded in the template own high regularity and vertical alignment. After the removal of PAM template, the NiNWs were still regularly and vertically aligned in the case of a small aspect ratio for NiNWs, for instance, the aspect ratio of 17 (which NiNWs are 150 nm in diameter and 2.5 μm in length), as shown in SEM images in Figures 5-41a and b. It is worth noting that such stubby type of metal nanowire arrays have been widely adopted as conductive scaffold to produce nanoelectrodes for SCs and batteries,[41, 159, 196] but they are frequently complained for their low efficient specific surface area. When the aspect ratio of NiNWs reaches 27 (*e.g.*, 4 μm in length, Figure 5-41c), regular and vertical arrays of NiNWs became disordered, and dozens of NiNWs leaned against each other and dislocated their original position. After further increasing the aspect ratio of NiNWs to 40 (6 μm in length) or even larger (Figures 5-41d and 1e), more NiNWs were found to adhere to each other at their tips and clustered into disordered domains. As can be seen from the cross-sectional view SEM image (Figure 5-41f), NiNWs with aspect ratio of 67 (10 μm in length) are like stalk lodging in the field, which severely aggregated into bundles without uniform interwire spacing. Noteworthy, the agglomeration is driven by the surface tension force exerting on each NiNW when being dried and its degree strongly depends on the aspect ratio of NiNWs.[193, 197]

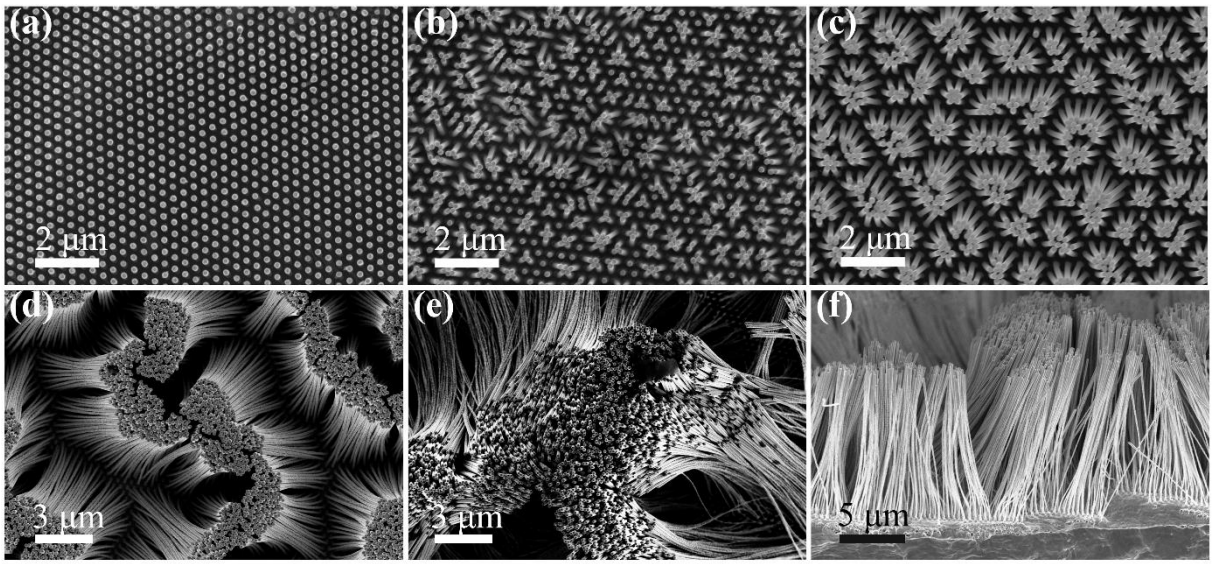

Figure 5-41 Top-view SEM images of NiNWs with the length of (a) 2 μm, (b) 2.5 μm, (c) 4 μm, (d) 6 μm, and (e) 10 μm. The corresponding aspect ratios are 13, 17, 27, 40, and 67, respectively. (f) Cross-sectional view SEM images of NiNWs with length of 10 μm.

5.4.2 Non-aggregative property of the 1D NiNWs-EPAM platform

To address the agglomeration issue of NiNWs with high aspect ratio, in this work PAM template was partially retained, instead of being completely etched away. After the electrochemical deposition of NiNWs, a precisely-controlled wet chemical etching process was carried out to form an EPAM membrane, and finally, each NiNW was concentrically confined in every single long straight nanopore of EPAM. The fabrication process for the NiNWs-EPAM is shown in Figure 5-42a. Since each NiNW is isolated in an independent nanopore unit, the self-aggregation in NiNWs will be fundamentally avoided. The representative top-view SEM image in Figure 5-42b shows that the as-prepared NiNWs-EPAM possesses uniform hexagonal pores of EPAM with a pore size of 380 nm and NiNWs with diameter of 150 nm evenly arranged in each pore. The tilted-view SEM image (Figure 5-42c) reveals that the top of the NiNWs-EPAM structure is merely constructed by ultra-thin pore wall of EPAM, which effectively prevents the tip of NiNWs from adhering to each other when being dried. Besides, it should be noted that NiNWs-EPAM scaffold can be fabricated over a large scale (Figure 5-

42b and c). The unique structure of EPAM offers free and isolated spaces for each NiNW and meanwhile endows NiNWs with the structural merits of erect orientation, high regularity, and ordered arrangement. Besides, the sufficient room between the NiNW and the pore wall of EPAM allows the active materials to be conformally loaded along the NiNW. Figure 5-42d and e show the cross-section view of NiNWs-EPAM scaffold with NiNW of 10 μm in length (aspect ratio of 67) retained in a highly erect orientation. An EDX top-view overlay map (Figure 5-42f) shows that the hexagonally periodic distribution of O (green colour), Al (cyan colour) and Ni (golden colour) elements, respectively, with Ni being concentrically located in the hexagonal pore composing of Al and O. The EDX overlay map in a cross-sectional view (Figure 5-42g) also demonstrates that the pore wall of EPAM and NiNWs are alternately and vertically arranged, which is in accordance with the arrangement of scaffold architecture characterized above.

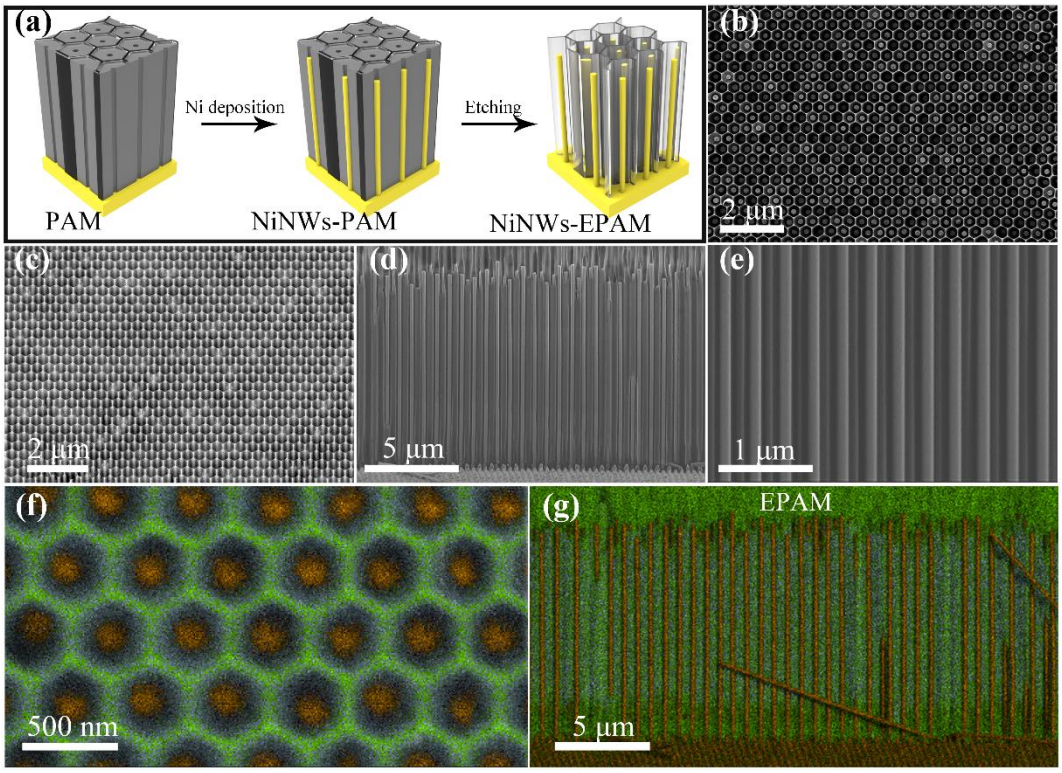

Figure 5-42 (a) Schematic illustration of the preparation process of the NiNWs-EPAM scaffold. (b) Top-, (c) tilted-, and (d) cross-sectional view SEM images and (e) the enlarged image. The

corresponding EDX overlay maps comprising of O (green colour), Al (cyan colour) and Ni (golden colour) elements: (f) top- and (g) cross-sectional view.

5.4.3 Mechanical reliability of the 1D NiNWs-EPAM platform

In addition to the self-aggregation, the conventional 1D nanoelectrode arrays usually suffer from the structural collapse issue during the device assembly process. The stress intolerance is becoming an application bottleneck for 1D nanoelectrode arrays particularly with high aspect ratio.[198] Noteworthy, the structural stability of 1D nanoelectrode arrays is largely dependent on the degree of their mechanical robustness, which needs to sustain external pressure without large structural strain or deformation. However, the structure of conventional NiNWs is susceptible to the external stress and becomes to irreversibly collapse after being applied a compressive strength, as schematically illustrated in Figure 5-43a. The SEM images in Figure 5-43b shows that the NiNWs with an aspect ratio of 67 severely distorted with arrays tightly sticking together and attaching horizontally to the substrate after the extrusion test under a pressure of 5 MPa. In this case, the irreversible collapse of electrode scaffold induced by its poor mechanical stability would block the efficient ionic transport pathway in the electrode and finally lead to a remarkable decay of the device performance. In the case of NiNWs-EPAM (Figure 5-43c), the robust EPAM structure can withstand considerable stress with almost no strain or structural damage owing to the high stiffness of EPAM structure, and thus the NiNWs-EPAM would maintain the desirable structural integrity after the same extrusion test. Meanwhile, the NiNWs can be still regularly and vertically aligned because the EPAM structure with high dense of hexagonal pores stands across the overall scaffold with its height over the length of NiNWs, which can well protect the NiNWs from crushing when an external force is loaded on the surface of the NiNWs-EPAM. As a result, NiNWs with length of 10 μm (*e.g.*, aspect ratio of 67) were well preserved in its straight-through nanopores, remaining the original vertical alignment of NiNWs (Figure 5-43d). Moreover, the robust mechanical stability of

NiNWs-EPAM would benefit to retaining the structural integrity of nanoelectrodes during device assembly. Furthermore, the optical image in Figure 5-43e shows the relatively colour change of NiNWs before and after extrusion test, revealing the dramatic structural evolution of NiNWs during this process. Whereas, no observed variation for the NiNWs-HAN implies that the robust HAN could sustain the extrusion force to protect the nanoelectrodes from destruction. Through evaluating the electrochemically active surface area (ECSA) of the NiNWs and NiNWs-EPAM before and after extrusion treatment, the significance of EPAM has been further highlighted. ECSA is estimated by calculating the double-layer capacitance (C_{dl}) values from CV, which is directly proportional to the ECSA.[199-200] As shown in Figure 5-43f, the ECSA before the extrusion is 192 cm^2 for NiNWs-EPAM, 138 cm^2 for NiNWs, and 4.5 cm^2 for bare EPAM, respectively. Here, NiNWs were 10 μm in length and 150 nm in diameter. The larger ECSA of NiNWs-EPAM indicates that the EPAM efficiently prevents high-aspect-ratio NiNWs from the self-aggregation to ensure the full play of NiNWs in contributing to a high ECSA. After the extrusion (Figure 5-43g), the ECSA of NiNWs-EPAM and EPAM scaffolds are 190 cm^2 and 4.5 cm^2, respectively. However, the ECSA of NiNWs was significantly reduced by nearly half (only 73 cm^2 left) due to the collapse of NiNWs (Figure 5-43b). The almost invariable ECSA again reveals that EPAM in NiNWs-EPAM contributes to not only avoiding the agglomeration of high-aspect-ratio NiNWs but also at the same time counteracting the impact of the external stress on NiNWs, and these features are of great benefit to the further construction of high-performance and mechanically-stable nanoelectrode.[201]

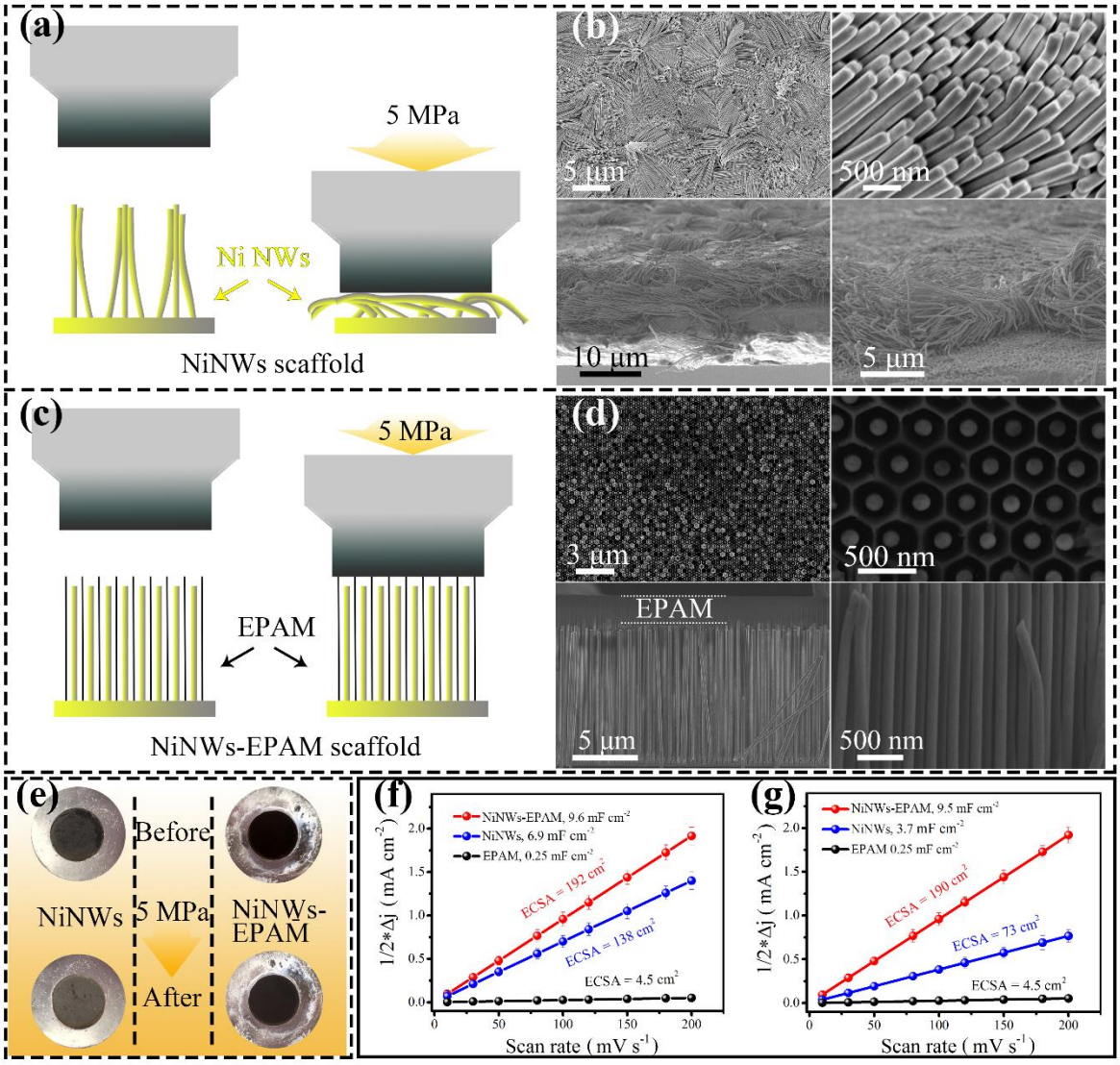

Figure 5-43 Schematic diagrams of extrusion tests for (a) NiNWs and (c) NiNWs-EPAM, and corresponding top- and cross-sectional view SEM images of the (b) NiNWs and (d) NiNWs-EPAM after extrusion tests. (e) Optical images of NiNWs and NiNWs-EPAM scaffolds before and after extrusion test. The estimation of double-layer capacitance (C_{dl}) and electrochemically active surface area (ECSA) (f) before and (g) after extrusion test for the NiNWs-EPAM, NiNWs and EPAM scaffolds.

Furthermore, by taking NiNWs-EPAM as nanoarchitectured current collector, MnO_2 and PPy were chosen as the representative pseudocapacitive materials to fabricate NiNWs@MnO_2-EPAM and NiNWs@PPy-EPAM nanoelectrodes, respectively. Figure 5-44a-c are the SEM images of NiNWs@MnO_2-EPAM nanoelectrode. The cross-sectional view SEM images

(Figures 5-44b and c) clearly revealed the conformal coating of MnO_2 on NiNWs, and the diameter of NiNWs@MnO_2 core-shell nanowires was about 200 nm. Moreover, there are still enough gaps in the interspace between NiNWs@MnO_2 and pore wall in each nanopore and these gaps will allow the infiltrated electrolyte to rapidly access to the pseudocapacitive materials for the fast electrochemical response. Similarly, Figure 5-44d-f shows the structural morphology of the as-obtained NiNWs@PPy-EPAM nanoelectrode. Noteworthy, with the help of EPAM, both NiNWs@MnO_2 and NiNWs@PPy with aspect ratio of 50 (10 μm in length) kept in highly erect arrangement (Figures 5-44b and e). Meanwhile, for comparison, the same amount of electrode materials (MnO_2 and PPy) were deposited on the identically structured NiNWs without EPAM support and protection to construct nanoelectrodes counterparts. Inherited from the frail structure of NiNWs, both NiNWs@MnO_2 and NiNWs@PPy nanoelectrodes severely aggregated. The agglomeration and collapse of both NiNWs@MnO_2 and NiNWs@PPy nanoelectrodes might be even worse when they were assembled into a MSC device, which will be elaborated afterward. As can be seen in Figures 5-44b and e, the length of electrically insulated EPAM is above that of NiNWs@MnO_2 and NiNWs@PPy units, thus MSC can be assembled by directly stacking two nanoelectrodes impregnated with electrolyte, which omits the separator to reduce the device volume. Figure 5-44g shows an assembled asymmetric MSC with the overall device thickness of 36 μm and the chip-like device has a whole footprint area of 0.4 cm^2 (Figure 5-44h).

5.4.4 Electrochemical performance of the NiNWs@MnO_2-EPAM//NiNWs@PPy-EPAM asymmetric micro-supercapacitors

An asymmetric MSC was constructed by using a NiNWs@MnO_2-EPAM as positive nanoelectrode and a NiNWs@PPy-EPAM as negative nanoelectrode, depicted as EPAM-assisted MSCs. The electrolyte for the asymmetric MSCs was 1.0 M Na_2SO_4. Prior to that, the mass loadings of pseudocapacitive materials in both positive and negative nanoelectrodes were

precisely tuned to meet the charge balance and prevent each nanoelectrode in MSC device from overcharging.

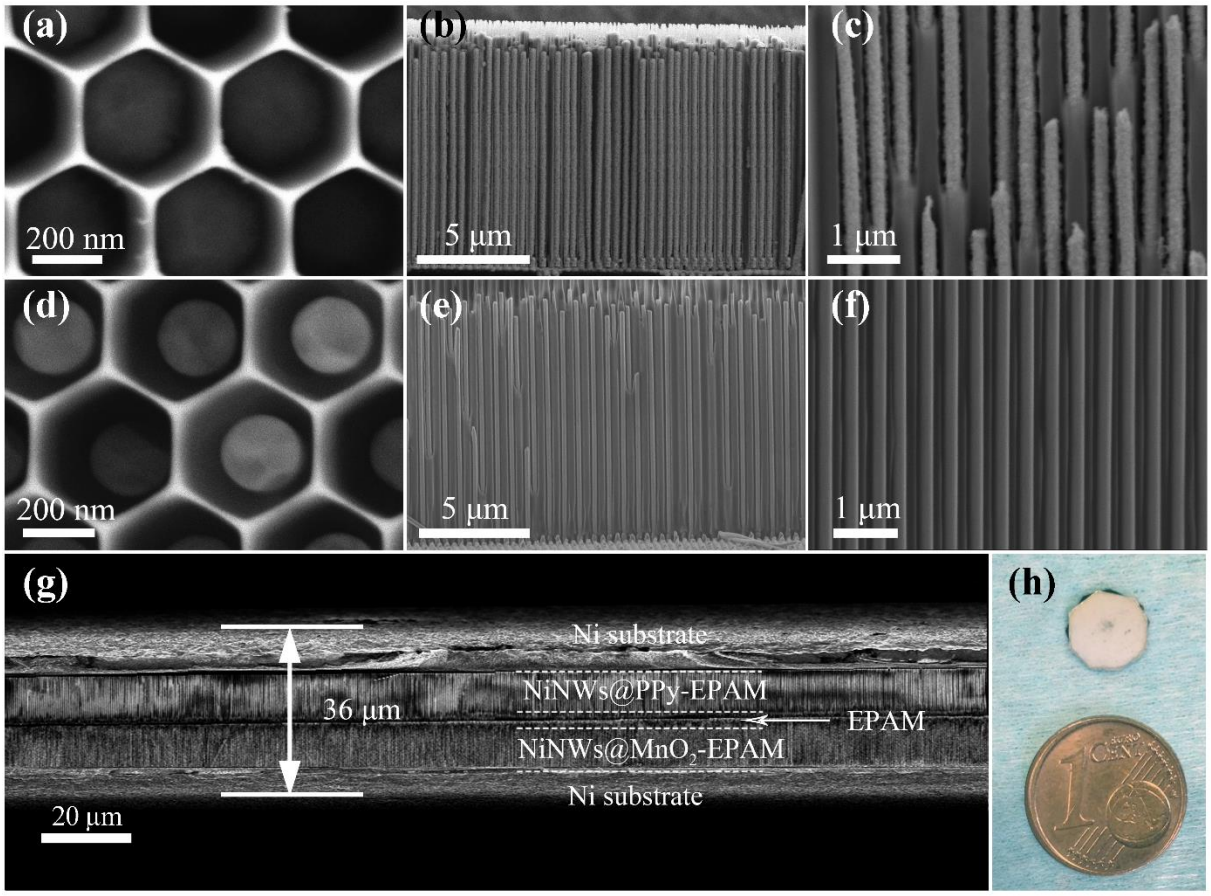

Figure 5-44. Top- and cross-sectional view SEM images of (a-c) NiNWs@MnO_2-EPAM, (d-f) NiNWs@PPy-EPAM nanoelectrodes. (g) The typical cross-sectional SEM image and (h) optical photograph of a stacked MSC.

In view of the individual voltage range of the positive and negative nanoelectrodes, an optimized voltage window of 0 – 1.6 V for the asymmetric MSC was achieved by gradually increasing voltage value from 0.8 to 1.6 V. To identify the role of EPAM in nanoelectrodes, the asymmetric MSC was also assembled with a NiNWs@MnO_2 and a NiNWs@PPy nanoelectrodes (depicted as EPAM-free MSC), and all the characterizations are conducted under the same conditions as those for EPAM-assisted MSC.

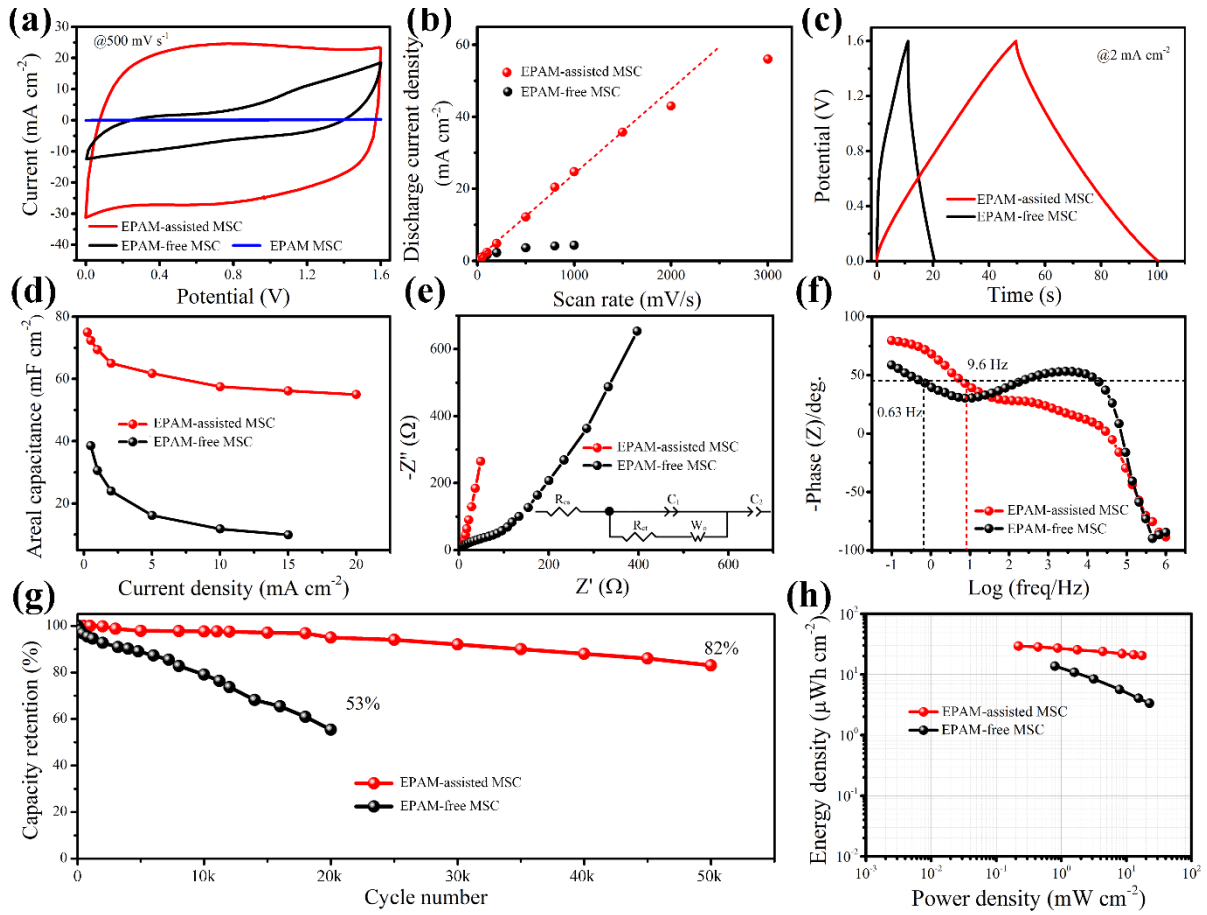

Figure 5-45 Electrochemical performance evaluation between EPAM-assisted MSC (NiNWs@MnO_2-EPAM//NiNWs@PPy-EPAM) and EPAM-free MSC (NiNWs@MnO_2//NiNWs@PPy): (a) CV curves at scan rate of 500 mV s^{-1}, (b) The discharge current with response to the scan rates. (c) GCD profiles at current density of 2 mA cm^{-2}. (d) Corresponding areal capacitance as a function of current densities. (e) Nyquist plots and inset figure is the equivalent circuit model. (f) Bode-phase plots. (g) Cycling performance. (h) Ragone plots.

Figure 5-45a compares the CV curves obtained at a scan rate of 500 mV s^{-1} for both EPAM-assisted and EPAM-free MSCs. The quasi-rectangular CV curve of EPAM-assisted MSC indicates its better capacitive behavior than that of EPAM-free MSC. Besides, with respect to EPAM-assisted MSC, the discharge current densities derived from CV profiles at various scan rates exhibited a perfect linear relationship within the scan rates from 5 to 1,500 mV s^{-1} (Figure 5-45b), while the discharge current densities of EPAM-free MSC severely deviated from the

linear relationship when scan rate exceeds to 100 mV s^{-1}. Such fast response capability of EPAM-assisted MSC should be ascribed to the rapid ion diffusion and electron transfer inside the nanoelectrodes benefiting from the synergistic effect of numerous accessible nanopores of EPAM for electrolyte ions infiltration and straight-through conductive NiNWs with large effective specific surface area.[202-203] Figure 5-45c presents the GCD curves at current density of 2 mA cm^{-2}. In accordance with the CV measurement, EPAM-assisted MSC exhibited a standard symmetrical charge-discharge profile with a small voltage drop and prolonged discharge time, indicating the superior charge-storage efficiency and low internal resistance. In contrast, EPAM-free MSC suffered from short discharge time and limited Coulombic efficiency, which largely arises from the blocked ionic diffusion path as a consequence of the collapse of nanoelectrode arrays during the device assembly. Figure 5-45d lists the areal capacitances calculated from the GCD curves. The EPAM-assisted MSC delivered a high areal capacitance of 75 mF cm^{-2} at current density of 0.2 mA cm^{-2}, which is nearly two times of that of the EPAM-free counterpart (38 mF cm^{-2}) at the same current density, and still retained 55 mF cm^{-2} (73% capacitive retention) as the current density is increased from 0.2 mA cm^{-2} up to 20 mA cm^{-2}.

The EIS was further recorded in a range of 1 MHz to 100 mHz to evaluate the role of EPAM in nanoelectrodes. Figure 5-45e shows the Nyquist plots and the equivalent electrical circuit in the right inset. Remarkably, the plot of EPAM-assisted MSC at low frequency region was almost perpendicular to the real axis and the slope of this range was superior to that of EPAM-free MSC, further highlighting the significant role of voids available inside the EPAM nanopores and erect geometry of NiNWs@MnO_2 or NiNWs@PPy units in contributing to the rapid ions diffusion in EPAM-assisted nanoelectrodes.[204] Besides, as can be seen from the magnified portion of the Nyquist plots, EPAM-assisted MSC possesses a much small R_{ct} of 5.6 Ω, which is considerably smaller than that of EPAM-free MSC (51.2 Ω). The smaller R_{ct}

suggests the rapid charge transport efficiency for the EPAM-assisted nanoelectrodes. The phase response of frequency for the MSCs are shown in Figure 5-45f. The frequency at phase angle of −45°, where the resistive and capacitive impedances are equal, was measured to be 9.6 Hz for EPAM-assisted MSC and 0.6 Hz for EPAM-free MSC. Therefore, the corresponding time constant (τ_0), which is defined as the minimum time required for the energy release with an efficiency above 50%, was calculated to be ~0.1 s for the EPAM-assisted MSC, far lower than that of the EPAM-free MSC (1.6 s). The smaller τ_0 again confirms that the erect geometry and free void of the EPAM-assisted nanoelectrodes facilitates the rapid ions diffusion within the electrode structure, ultimately improving the capability of instantaneous energy and power delivery.[203]

Additionally, EPAM-assisted MSC delivered a remarkable capacitance retention of 82% after 50,000 consecutive charge-discharge cycles (Figure 5-45g), whereas merely 53% capacitance retention after 20,000 cycles for the EPAM-free MSC. This excellent cyclic stability of EPAM-assisted MSC should be attributed to the structural advantage that the spatially confined effect of EPAM help to prevent the fast degradation of electrode materials.[200, 205-206] To evaluate the practical potential, Ragone plots of energy and power densities of MSCs were calculated in Figure 5-45h. The EPAM-assisted MSC delivered a peak energy density of 29.3 μWh cm^{-2} at power density of 0.22 mW cm^{-2}, which is over twice that of the EPAM-free MSC (13.6 μWh cm^{-2}). Moreover, when the ionic liquid electrolyte (EMIM-TFSI) was adopted in EPAM-assisted MSC, the potential window of device was further extended to 3.0 V (Figure 5-46a and b). Besides, MSC still retained desired electrochemical properties, either from the large capacitance density (67.8 mF cm^{-2} at 0.5 mA cm^{-2}) or high rate capability (16 mF cm^{-2} at 10 mA cm^{-2}, Figure 5-46c). Impressively, the peak energy and power densities of MSC with ionic liquid electrolyte are 84 μWh cm^{-2} and 26 mW cm^{-2}, respectively, which are comparable with those of state-of-the-art MSCs that reported recently (Figure 5-46d).[157, 177, 185, 207-213]

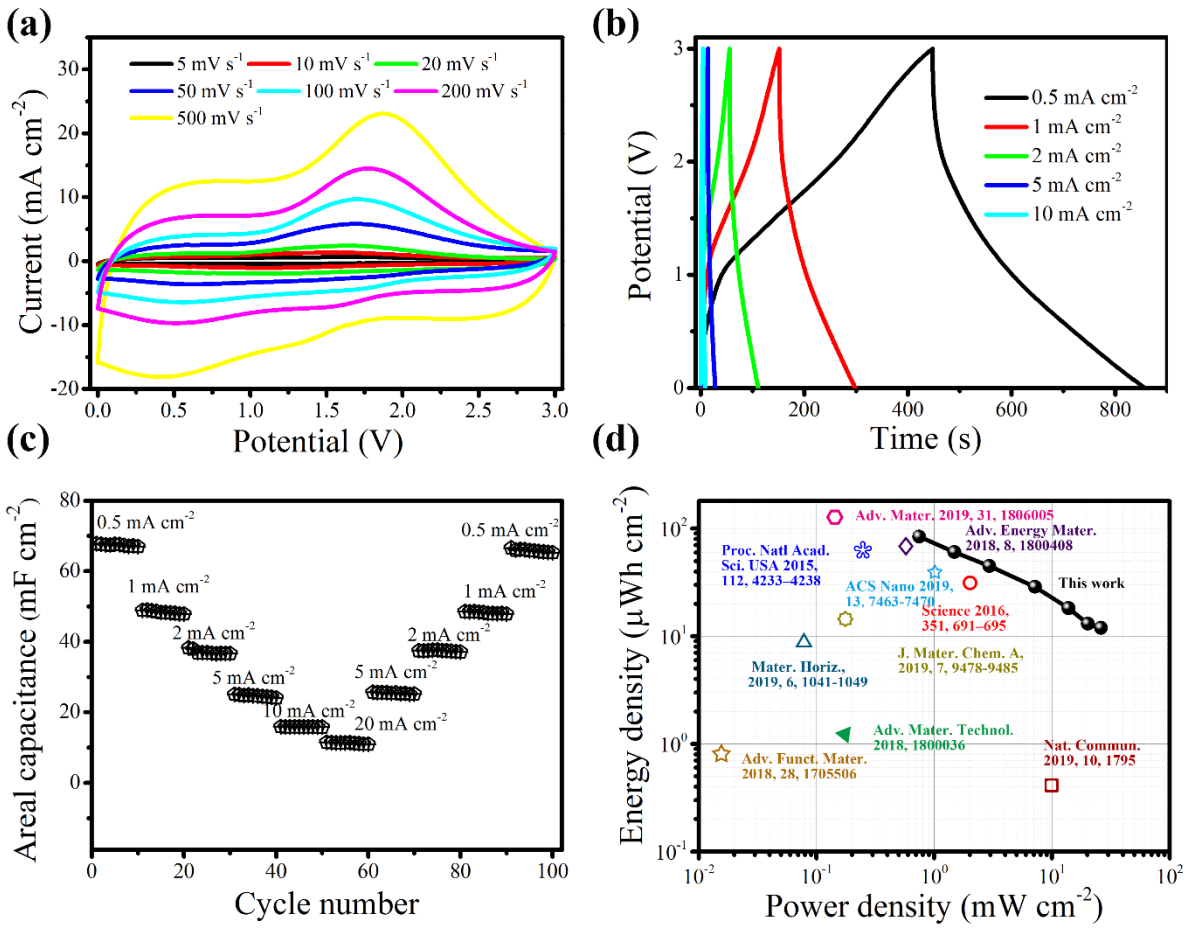

Figure 5-46 (a) CV curves, (b) GCD profiles, (c) rate performance and (d) Ragone plots of NiNWs@MnO_2-EPAM//NiNWs@PPy-EPAM MSC with ionic liquid electrolyte (1M EMIM-TFSI in ACN).

After the electrochemical measurements, the nanoelectrodes was detached from MSCs and their structural changes were probed by SEM. Apparently, NiNWs@MnO_2 or NiNWs@PPy nanoelectrode without EPAM suffers from severe structural distortion, forming a textile-like film constituted by the 1D nanostructure arrays, as exhibited in Figure 5-47a and b. In this case, the reduction in the longitudinal charges/ions transport efficiency and effective electrode area caused by the structural collapse yields a significant loss in the electrochemical performance. Nevertheless, EPAM-assisted nanoelectrodes with identically structured NiNWs@MnO_2 or NiNWs@PPy units maintain nearly intact 1D nanostructure with high vertically alignment (Figure 5-47c and d), and their robust mechanical stability is in accordance with that of NiNWs-

EPAM electrode scaffold as mentioned above. The integrated 1D nanostructure arrays with erect feature and ample void endowed by EPAM play a crucial role in not only reducing the diffusion resistance of electrolyte but also maintaining the smooth electron pathways, which is responsible for the substantially improved performance.

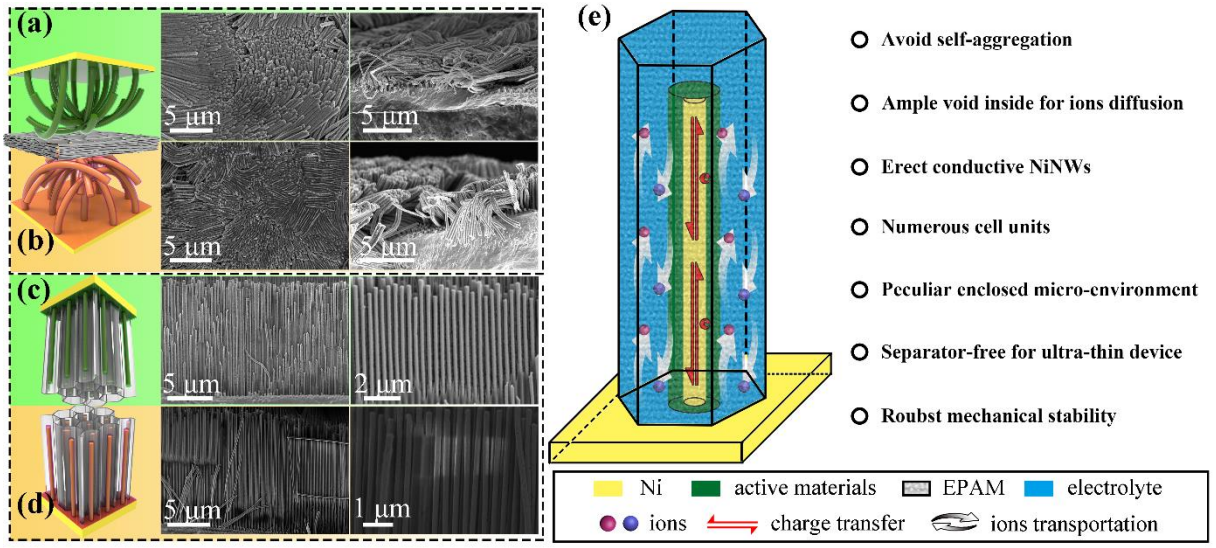

Figure 5-47 Schematic structure models and corresponding SEM images of the (a) NiNWs@MnO_2, (b) NiNWs@PPy, (c) NiNWs@MnO_2-EPAM and (d) NiNWs@PPy-EPAM nanoelectrodes after electrochemical performance. (e) Schematic illustration of a single cell unit in the EPAM-assisted nanoelectrode.

In view of the above analysis, several distinctive design merits of EPAM-assisted nanoelectrode are outlined in Figure 5-47e: i) the ultra-thin pore wall of EPAM acts as "spacers" to avoid the aggregation of nanoelectrodes; ii) ample void available inside the EPAM promotes fast ions transfer; iii) vertically-aligned NiNWs contribute to the electrical conductivity of overall nanoelectrode; iv) numerous cell units in nanoelectrode play for the whole performance; v) peculiar enclosed micro-environment prevents fast degradation of electrode materials; vi) separator-free of stacked MSC reduces thickness of device; vii) 1D nanoelectrode structure with large aspect ratio have high degree of erectness and robustness. Overall, EPAM-assisted nanoelectrode with intriguing architecture integrates the above merits to synergistically

facilitate the transportation of ions and electrons in a quick, efficient and steady state, without any concession in mechanical robustness.

6 Summary and Conclusion

In summary, three different nanoarchitectured current collectors were rationally designed to satisfy the following two categories: One is replacing conventional current collectors in thick-layer electrodes to improve the mass loading, and the other is the construction of the mechanically robust nanoelectrodes for high-energy MSCs. The main contributions of this dissertation can be concluded in the following aspects:

1. We have studied the role of nanoarchitectured current collectors in fabricating SC electrodes with the pseudocapacitive materials in the form of thick layer. Here, Ni nanorod arrays were fabricated as an example of nanoarchitectured current collectors, while MnO_2 was selected as typical pseudocapacitive material and was electrochemically deposited onto Ni nanorod arrays to construct SC electrodes. With the same mass loading of MnO_2 as pseudocapacitive materials in SC electrodes, the utilization of Ni nanorod arrays as current collectors have achieved much higher areal capacitance and better rate capability as well as higher structural stability compared to the planar Ni foils as current collectors, in the both cases of MnO_2 in ultrathin and thick layer. Detailed electrochemical characterization revealed that nanoarchitectured current collector in SC electrodes with thick-layer pseudocapacitive materials could significantly reduce the interfacial resistance at the pseudocapacitive-materials/current-collectors interfaces to improve the charge transfer efficiency, and finally to accomplish high energy storage capability.

2. We demonstrated the design and fabrication of the EPAM nanoscaffold with ultrathin pore wall and stiff honeycomb structure for the first time. After converting the insulating EPAM to a nanoarchitectured current collector, the resultant EPAM@SnO_2 retains the original honeycomb features and vertically aligned and robustly stable nanoporous structure. The electrochemical performance demonstrated that EPAM@SnO_2 exhibited ultrafast ion migration and transportation, which is attributing to its numerous straight and uniform nanochannels. The combination of pseudocapacitive materials with the unique EPAM@SnO_2 nanoarchitectured

current collector results in the increased areal capacitance for MSCs, meanwhile the adoption of asymmetric configuration coupled with ionic liquid electrolyte helps to overcome the narrow operating potential window of pseudocapacitive materials. As a result, an asymmetric MSC constructed with the EPAM@SnO_2-based nanoelectrodes exhibits record high-energy performance among the reported MSCs.

3. We have developed an efficient strategy to address the challenging issue regarding the unreliable structural properties of high-aspect-ratio 1D nanoelectrode arrays. High-aspect-ratio, non-aggregative and robust 1D nanoelectrode arrays were successfully fabricated by confining every freestanding 1D nanoelectrode with a high aspect ratio (*e.g.*, 50) into individual nanopore of the EPAM with ultrathin pore wall. The existence of EPAM avoids the self-agglomeration of high-aspect-ratio 1D nanoelectrode arrays and at the same time protects them from the destruction during both the assembly of MSCs and thereafter the consecutive charge-discharge of MSCs. As a result, EPAM-assisted MSCs exhibited the significantly improved electrochemical performance, *i.e.*, high energy density, remarkable rate capability and excellent cyclic stability in contrast to EPAM-free MSCs.

Overall, nanoarchitectured current collectors play vital roles in enhancing the electrochemical performance of SCs. The successful applications of nanoarchitectured current collectors in SCs will provide a new avenue to the energy storage and conversion related devices such as fuel cells and batteries, which also suffer from the inferior practical energy density.

7 Bibliography

1. Shao, Y.; El-Kady, M. F.; Sun, J.; Li, Y.; Zhang, Q.; Zhu, M.; Wang, H.; Dunn, B.; Kaner, R. B., *Chem. Rev.* **2018,** *118* (18), 9233-9280.

2. Simon, P.; Gogotsi, Y.; Dunn, B., *Science* **2014,** *343* (6176), 1210-1211.

3. Gogotsi, Y.; Penner, R. M., *ACS Nano* **2018,** *12* (3), 2081-2083.

4. Conway, B. E., *Electrochemical Supercapacitors: Scientific Fundamentals and Technological Applications*. Kluwer Academic/Plenum: New York, 1999.

5. Liu, J.; Wang, J.; Xu, C.; Jiang, H.; Li, C.; Zhang, L.; Lin, J.; Shen, Z. X., *Adv. Sci.* **2017,** *5* (1), 1700322.

6. Snook, G. A.; Kao, P.; Best, A. S., *J. Power Sources* **2011,** *196* (1), 1-12.

7. Brezesinski, T.; Wang, J.; Tolbert, S. H.; Dunn, B., *Nat. Mater.* **2010,** *9* (2), 146.

8. Griffith, K. J.; Forse, A. C.; Griffin, J. M.; Grey, C. P., *J. Am. Chem. Soc.* **2016,** *138* (28), 8888-8899.

9. Augustyn, V.; Come, J.; Lowe, M. A.; Kim, J. W.; Taberna, P.-L.; Tolbert, S. H.; Abruña, H. D.; Simon, P.; Dunn, B., *Nat. Mater.* **2013,** *12* (6), 518.

10. Anasori, B.; Lukatskaya, M. R.; Gogotsi, Y., *Nat. Rev. Mater.* **2017,** *2* (2), 16098.

11. Dubal, D. P.; Ayyad, O.; Ruiz, V.; Gomez-Romero, P., *Chem. Soc. Rev.* **2015,** *44* (7), 1777-1790.

12. Brezesinski, K.; Wang, J.; Haetge, J.; Reitz, C.; Steinmueller, S. O.; Tolbert, S. H.; Smarsly, B. M.; Dunn, B.; Brezesinski, T., *J. Am. Chem. Soc.* **2010,** *132* (20), 6982-6990.

13. Lukatskaya, M. R.; Dunn, B.; Gogotsi, Y., *Nat. Commun.* **2016,** *7*, 12647.

14. Salanne, M.; Rotenberg, B.; Naoi, K.; Kaneko, K.; Taberna, P.-L.; Grey, C. P.; Dunn, B.; Simon, P., *Nat. Energy* **2016,** *1*, 16070.

15. Augustyn, V.; Simon, P.; Dunn, B., *Energy Environ. Sci.* **2014,** *7* (5), 1597-1614.

16. Zuo, W.; Li, R.; Zhou, C.; Li, Y.; Xia, J.; Liu, J., *Adv. Sci.* **2017,** *4* (7), 1600539.

17. Bélanger, D.; Brousse, L.; Long, J. W., *Electrochem. Soc. Interface* **2008,** *17* (1), 49.

18. Adeyemo, A.; Hunter, G.; Dutta, P. K., *Sens. Actuators, B* **2011,** *152* (2), 307-315.

19. Nandy, S.; Maiti, U.; Ghosh, C.; Chattopadhyay, K., *J. Phys.: Condens. Matter* **2009,** *21* (11), 115804.

20. Hamdani, M.; Singh, R.; Chartier, P., *Int. J. Electrochem. Sci* **2010,** *5* (4), 556-577.

21. Chen, Z.; Augustyn, V.; Wen, J.; Zhang, Y.; Shen, M.; Dunn, B.; Lu, Y., *Adv. Mater.* **2011,** *23* (6), 791-795.

22. Wang, X.; Li, G.; Chen, Z.; Augustyn, V.; Ma, X.; Wang, G.; Dunn, B.; Lu, Y., *Adv. Energy Mater.* **2011,** *1* (6), 1089-1093.

23. Zhai, T.; Sun, S.; Liu, X.; Liang, C.; Wang, G.; Xia, H., *Adv. Mater.* **2018,** *30* (12), 1706640.

24. Eftekhari, A.; Li, L.; Yang, Y., *J. Power Sources* **2017,** *347*, 86-107.

25. Laforgue, A.; Simon, P.; Sarrazin, C.; Fauvarque, J.-F., *J. Power Sources* **1999,** *80* (1-2), 142-148.

26. Zhi, M.; Xiang, C.; Li, J.; Li, M.; Wu, N., *Nanoscale* **2013,** *5* (1), 72-88.

27. Yuan, C.; Wu, H. B.; Xie, Y.; Lou, X. W. D., *Angew. Chem. Int. Ed.* **2014,** *53* (6), 1488-1504.

28. Simon, P.; Gogotsi, Y., *Nat. Mater.* **2008,** *7* (11), 845-854.

29. Wang, G.; Zhang, L.; Zhang, J., *Chem. Soc. Rev.* **2012,** *41* (2), 797-828.

30. Kou, T.; Yao, B.; Liu, T.; Li, Y., *J. Mater. Chem. A* **2017,** *5* (33), 17151-17173.

31. Zhao, H.; Liu, L.; Vellacheri, R.; Lei, Y., *Adv. Sci.* **2017,** *4* (10), 1700188.

32. Wen, L.; Zhou, M.; Wang, C.; Mi, Y.; Lei, Y., *Adv. Energy Mater.* **2016,** *6* (23), 1600468.

33. Wang, Z.; Cao, D.; Xu, R.; Qu, S.; Wang, Z.; Lei, Y., *Nano Energy* **2016,** *19*, 328-362.

34. Zhao, H.; Zhou, M.; Wen, L.; Lei, Y., *Nano Energy* **2015,** *13*, 790-813.

35. Wei, Q.; Xiong, F.; Tan, S.; Huang, L.; Lan, E. H.; Dunn, B.; Mai, L., *Adv. Mater.* **2017,** *29* (20), 1602300.

36. Aricò, A. S.; Bruce, P.; Scrosati, B.; Tarascon, J.-M.; Van Schalkwijk, W., *Nat. Mater.* **2005,** *4* (5), 366-377.

37. Zhao, X.; Sánchez, B. M.; Dobson, P. J.; Grant, P. S., *Nanoscale* **2011,** *3* (3), 839-855.

38. Yu, X.; Yun, S.; Yeon, J. S.; Bhattacharya, P.; Wang, L.; Lee, S. W.; Hu, X.; Park, H. S., *Adv. Energy Mater.* **2018,** *8* (13), 1702930.

39. Kang, J.; Zhang, S.; Zhang, Z., *Adv. Mater.* **2017,** *29* (48), 1700515.

40. Rolison, D. R.; Long, J. W.; Lytle, J. C.; Fischer, A. E.; Rhodes, C. P.; McEvoy, T. M.; Bourg, M. E.; Lubers, A. M., *Chem. Soc. Rev.* **2009,** *38* (1), 226-252.

41. Taberna, P.-L.; Mitra, S.; Poizot, P.; Simon, P.; Tarascon, J.-M., *Nat. Mater.* **2006,** *5* (7), 567.

42. Evanko, B.; Yoo, S. J.; Lipton, J.; Chun, S.-E.; Moskovits, M.; Ji, X.; Boettcher, S. W.; Stucky, G. D., *Energy Environ. Sci.* **2018**, DOI:10.1039/C8EE00546J.

43. Lu, Q.; Chen, J. G.; Xiao, J. Q., *Angew. Chem. Int. Ed.* **2013,** *52* (7), 1882-1889.

44. Jiang, J.; Li, Y.; Liu, J.; Huang, X.; Yuan, C.; Lou, X. W. D., *Adv. Mater.* **2012,** *24* (38), 5166-5180.

45. Wan, M., *Adv. Mater.* **2008,** *20* (15), 2926-2932.

46. Zhu, H.; Xiao, C.; Cheng, H.; Grote, F.; Zhang, X.; Yao, T.; Li, Z.; Wang, C.; Wei, S.; Lei, Y., *Nat. Commun.* **2014,** *5*, 3960.

47. Cao, D.; Nasori, N.; Wang, Z.; Mi, Y.; Wen, L.; Yang, Y.; Qu, S.; Wang, Z.; Lei, Y., *J. Mater. Chem. A* **2016,** *4* (23), 8995-9001.

48. Liang, L.; Xu, Y.; Lei, Y.; Liu, H., *Nanoscale* **2014,** *6* (7), 3536-3539.

49. Mi, Y.; Wen, L.; Wang, Z.; Cao, D.; Fang, Y.; Lei, Y., *Appl. Catal., B* **2015,** *176*, 331-337.

50. Xue, Q.; Gan, H.; Huang, Y.; Zhu, M.; Pei, Z.; Li, H.; Deng, S.; Liu, F.; Zhi, C., *Adv. Energy Mater.* **2018,** *8*, 1703117.

51. Liu, L.; Chen, N.; Lei, Y.; Xue, X.; Li, L.; Wang, J.; Komarneni, S.; Zhu, H.; Yang, D., *J. Hazard. Mater.* **2018,** *360* (15), 279-287.

52. Yang, Q.; Lu, Z.; Liu, J.; Lei, X.; Chang, Z.; Luo, L.; Sun, X., *Prog. Nat. Sci.* **2013,** *23* (4), 351-366.

53. Liu, J.; Jiang, J.; Cheng, C.; Li, H.; Zhang, J.; Gong, H.; Fan, H. J., *Adv. Mater.* **2011,** *23* (18), 2076-2081.

54. Sarkar, D.; Das, S.; Sharada, G.; Pal, B.; Rensmo, H.; Shukla, A.; Sarma, D., *J. Electrochem. Soc.* **2017,** *164* (6), A987-A994.

55. Ren, Q.-H.; Zhang, Y.; Lu, H.-L.; Wang, Y.-P.; Liu, W.-J.; Ji, X.-M.; Devi, A.; Jiang, A.-Q.; Zhang, D. W., *ACS Appl. Mater. Interfaces* **2017,** *10* (1), 468-476.

56. Liu, J.; Cheng, C.; Zhou, W.; Li, H.; Fan, H. J., *Chem. Commun.* **2011,** *47* (12), 3436-3438.

57. He, W.; Liang, Z.; Ji, K.; Sun, Q.; Zhai, T.; Xu, X., *Nano Res.* **2018,** *11* (3), 1415-1425.

58. He, W.; Wang, C.; Li, H.; Deng, X.; Xu, X.; Zhai, T., *Adv. Energy Mater.* **2017,** *7* (21), 1700983.

59. Zhu, J.; Huang, L.; Xiao, Y.; Shen, L.; Chen, Q.; Shi, W., *Nanoscale* **2014,** *6* (12), 6772-6781.

60. Liu, L.; Hou, H.; Wang, L.; Xu, R.; Lei, Y.; Shen, S.; Yang, D.; Yang, W., *Nanoscale* **2017,** *9* (40), 15650-15657

61. Xia, X.; Tu, J.; Zhang, Y.; Wang, X.; Gu, C.; Zhao, X.-b.; Fan, H. J., *ACS Nano* **2012,** *6* (6), 5531-5538.

62. Yang, P.; Chao, D.; Zhu, C.; Xia, X.; Zhang, Y.; Wang, X.; Sun, P.; Tay, B. K.; Shen, Z. X.; Mai, W.; Fan, H. J., *Adv. Sci.* **2016,** *3* (6), 1500299.

63. Li, Z.; Wang, F.; Wang, X., *Small* **2017,** *13* (1), 1603076.

64. Han, H.; Huang, Z.; Lee, W., *Nano Today* **2014,** *9* (3), 271-304.

65. Mai, L.; Tian, X.; Xu, X.; Chang, L.; Xu, L., *Chem. Rev.* **2014,** *114* (23), 11828-11862.

66. Mirvakili, S. M.; Hunter, I. W., *Adv. Mater.* **2017,** *29* (27), 1700671.

67. Kim, J.-H.; Zhu, K.; Yan, Y.; Perkins, C. L.; Frank, A. J., *Nano Lett.* **2010,** *10* (10), 4099-4104.

68. Zhou, H.; Zou, X.; Zhang, K.; Sun, P.; Islam, M. S.; Gong, J.; Zhang, Y.; Yang, J., *ACS Appl. Mater. Interfaces* **2017,** *9* (22), 18699-18709.

69. Ozkan, S.; Nguyen, N. T.; Hwang, I.; Mazare, A.; Schmuki, P., *Small* **2017,** *13* (14), 1603821.

70. Vellacheri, R.; Zhao, H.; Mühlstädt, M.; Al‐Haddad, A.; Jandt, K. D.; Lei, Y., *Adv. Funct. Mater.* **2017,** *27* (18), 1606696.

71. Vellacheri, R.; Zhao, H.; Mühlstädt, M.; Ming, J.; Al‐Haddad, A.; Wu, M.; Jandt, K. D.; Lei, Y., *Adv. Mater. Technol.* **2016,** *1* (1), 1600012.

72. Yu, C.; Wang, Y.; Zhang, J.; Yang, W.; Shu, X.; Qin, Y.; Cui, J.; Zheng, H.; Zhang, Y.; Ajayan, P. M., *J. Power Sources* **2017,** *364*, 400-409.

73. Li, X.-J.; Zhao, Y.; Chu, W.-G.; Wang, Y.; Li, Z.-J.; Jiang, P.; Zhao, X.-C.; Liang, M.; Liu, Y., *RSC Adv.* **2015,** *5* (94), 77437-77442.

74. Liu, J.; Essner, J.; Li, J., *Chem. Mater.* **2010,** *22* (17), 5022-5030.

75. Ortaboy, S.; Alper, J. P.; Rossi, F.; Bertoni, G.; Salviati, G.; Carraro, C.; Maboudian, R., *Energy Environ. Sci.* **2017,** *10* (6), 1505-1516.

76. Zhang, S.; Yin, B.; Jiang, H.; Qu, F.; Umar, A.; Wu, X., *Dalton Trans.* **2015,** *44* (5), 2409-2415.

77. Dam, D. T.; Wang, X.; Lee, J.-M., *Nano Energy* **2013,** *2* (6), 1303-1313.

78. Wang, X.; Sumboja, A.; Lin, M.; Yan, J.; Lee, P. S., *Nanoscale* **2012,** *4* (22), 7266-7272.

79. Wang, S.; Shao, Y.; Liu, W.; Wu, Y.; Hao, X., *J. Mater. Chem. A* **2018,** *6* (27), 13215-13224.

80. Wang, S.; Sun, C.; Shao, Y.; Wu, Y.; Zhang, L.; Hao, X., *Small* **2017,** *13* (8), 1603330.

81. Ding, Y.; Chen, M.; Erlebacher, J., *J. Am. Chem. Soc.* **2004,** *126* (22), 6876-6877.

82. Guo, X.; Han, J.; Zhang, L.; Liu, P.; Hirata, A.; Chen, L.; Fujita, T.; Chen, M., *Nanoscale* **2015,** *7* (37), 15111-15116.

83. Yu, J.; Ding, Y.; Xu, C.; Inoue, A.; Sakurai, T.; Chen, M., *Chem. Mater.* **2008,** *20* (14), 4548-4550.

84. Kang, J.; Chen, L.; Hou, Y.; Li, C.; Fujita, T.; Lang, X.; Hirata, A.; Chen, M., *Adv. Energy Mater.* **2013,** *3* (7), 857-863.

85. Lang, X.; Hirata, A.; Fujita, T.; Chen, M., *Nat. Nanotechnol.* **2011,** *6* (4), 232-236.

86. Kang, J.; Hirata, A.; Qiu, H. J.; Chen, L.; Ge, X.; Fujita, T.; Chen, M., *Adv. Mater.* **2014,** *26* (2), 269-272.

87. Kang, J.; Hirata, A.; Chen, L.; Zhu, S.; Fujita, T.; Chen, M., *Angew. Chem. Int. Ed.* **2015,** *127* (28), 8218-8222.

88. Shin, H.-C.; Dong, J.; Liu, M., *Adv. Mater.* **2003,** *15* (19), 1610-1614.

89. Varzi, A.; Mattarozzi, L.; Cattarin, S.; Guerriero, P.; Passerini, S., *Adv. Energy Mater.* **2018,** *8* (1), 1701706.

90. Ferris, A.; Garbarino, S.; Guay, D.; Pech, D., *Adv. Mater.* **2015,** *27* (42), 6625-6629.

91. Ji, Y.; Xie, J.; Wu, J.; Yang, Y.; Fu, X.-Z.; Sun, R.; Wong, C.-P., *J. Power Sources* **2018,** *393*, 54-61.

92. Yu, Z.; Cheng, Z.; Wang, X.; Dou, S. X.; Kong, X., *J. Mater. Chem. A* **2017,** *5* (17), 7968-7978.

93. Saravanakumar, B.; Jayaseelan, S. S.; Seo, M.-K.; Kim, H.-Y.; Kim, B.-S., *Nanoscale* **2017,** *9* (47), 18819-18834.

94. Kang, K.-N.; Kim, I.-H.; Ramadoss, A.; Kim, S.-I.; Yoon, J.-C.; Jang, J.-H., *Phys. Chem. Chem. Phys.* **2018,** *20* (2), 719-727.

95. Ashassi-Sorkhabi, H.; La'le Badakhshan, P., *Appl. Surf. Sci.* **2017,** *419*, 165-176.

96. Seok, J. Y.; Lee, J.; Yang, M., *ACS Appl. Mater. Interfaces* **2018,** *10* (20), 17223-17231.

97. Gao, G.; Wu, H. B.; Ding, S.; Liu, L. M.; Lou, X. W., *Small* **2015,** *11* (7), 804-808.

98. Zhenghui, P.; Jun, Z.; Qichong, Z.; Jie, Y.; Yongcai, Q.; Xiaoyu, D.; Kaiqi, N.; Hua, Y.; Kun, F.; Xianshu, W.; Guoguang, X.; Wanfei, L.; Yagang, Y.; Qinwen, L.; Meinan, L.; Yuegang, Z., *Adv. Energy Mater.* **2018,** *8* (14), 1702946.

99. Tappan, B. C.; Steiner, S. A.; Luther, E. P., *Angew. Chem. Int. Ed.* **2010,** *49* (27), 4544-4565.

100. Wen, L.; Wang, Z.; Mi, Y.; Xu, R.; Yu, S. H.; Lei, Y., *Small* **2015,** *11* (28), 3408-3428.

101. Wen, L.; Xu, R.; Mi, Y.; Lei, Y., *Nat. Nanotechnol.* **2017,** *12* (3), 244-250.

102. Lei, Y.; Chim, W.; Sun, H.; Wilde, G., *Appl. Phys. Lett.* **2005,** *86* (10), 103106.

103. Wang, Z.; Cao, D.; Wen, L.; Xu, R.; Obergfell, M.; Mi, Y.; Zhan, Z.; Nasori, N.; Demsar, J.; Lei, Y., *Nat. Commun.* **2016,** *7*, 10348.

104. Lei, Y.; Yang, S.; Wu, M.; Wilde, G., *Chem. Soc. Rev.* **2011,** *40* (3), 1247-1258.

105. Lei, Y.; Cai, W.; Wilde, G., *Prog. Mater Sci.* **2007,** *52* (4), 465-539.

106. Liu, L.; Zhao, H.; Wang, Y.; Fang, Y.; Xie, J.; Lei, Y., *Adv. Funct. Mater.* **2018,** *28* (6), 1705107.

107. Grote, F.; Zhao, H.; Lei, Y., *J. Mater. Chem. A* **2015,** *3* (7), 3465-3470.

108. Grote, F.; Lei, Y., *Nano Energy* **2014,** *10*, 63-70.

109. Wen, L.; Mi, Y.; Wang, C.; Fang, Y.; Grote, F.; Zhao, H.; Zhou, M.; Lei, Y., *Small* **2014,** *10* (15), 3162-3168.

110. Grote, F.; Kühnel, R.-S.; Balducci, A.; Lei, Y., *Appl. Phys. Lett.* **2014,** *104* (5), 053904.

111. Grote, F.; Wen, L.; Lei, Y., *J. Power Sources* **2014,** *256*, 37-42.

112. Zhan, Z.; Lei, Y., *ACS Nano* **2014,** *8* (4), 3862-3868.

113. Zhao, H.; Liu, L.; Lei, Y., *Front. Chem. Sci. Eng.* **2018,** *12*, 481-493.

114. Wu, M.; Wen, L.; Lei, Y.; Ostendorp, S.; Chen, K.; Wilde, G., *Small* **2010,** *6* (5), 695-699.

115. Zhu, S. J.; Zhang, J.; Ma, J. J.; Zhang, Y. X.; Yao, K. X., *J. Power Sources* **2015,** *278*, 555-561.

116. Fan, H. J.; Lee, W.; Scholz, R.; Dadgar, A.; Krost, A.; Nielsch, K.; Zacharias, M., *Nanotechnology* **2005,** *16* (6), 913.

117. Deng, M.-J.; Ho, P.-J.; Song, C.-Z.; Chen, S.-A.; Lee, J.-F.; Chen, J.-M.; Lu, K.-T., *Energy Environ. Sci.* **2013,** *6* (7), 2178-2185.

118. Choi, B. G.; Yang, M.; Hong, W. H.; Choi, J. W.; Huh, Y. S., *ACS Nano* **2012,** *6* (5), 4020-4028.

119. Zhou, M.; Xu, Y.; Wang, C.; Li, Q.; Xiang, J.; Liang, L.; Wu, M.; Zhao, H.; Lei, Y., *Nano Energy* **2017,** *31*, 514-524.

120. Zhang, H.; Yu, X.; Braun, P. V., *Nat. Nanotechnol.* **2011,** *6* (5), 277.

121. Deng, M.-J.; Song, C.-Z.; Ho, P.-J.; Wang, C.-C.; Chen, J.-M.; Lu, K.-T., *Phys. Chem. Chem. Phys.* **2013,** *15* (20), 7479-7483.

122. Kim, J.-H.; Kang, S. H.; Zhu, K.; Kim, J. Y.; Neale, N. R.; Frank, A. J., *Chem. Commun.* **2011,** *47* (18), 5214-5216.

123. Zhao, H.; Wang, C.; Vellacheri, R.; Zhou, M.; Xu, Y.; Fu, Q.; Wu, M.; Grote, F.; Lei, Y., *Adv. Mater.* **2014,** *26* (45), 7654-7659.

124. Zhao, H.; Liu, L.; Fang, Y.; Vellacheri, R.; Lei, Y., *Front. Chem. Sci. Eng.* **2018,** *12*, 339–345.

125. Masuda, H.; Fukuda, K., *Science* **1995,** *268* (5216), 1466-1468.

126. Ji, J.; Zhang, L. L.; Ji, H.; Li, Y.; Zhao, X.; Bai, X.; Fan, X.; Zhang, F.; Ruoff, R. S., *ACS Nano* **2013,** *7* (7), 6237-6243.

127. He, Y.; Chen, W.; Li, X.; Zhang, Z.; Fu, J.; Zhao, C.; Xie, E., *ACS Nano* **2012,** *7* (1), 174-182.

128. Yu, X.; Lu, B.; Xu, Z., *Adv. Mater.* **2014,** *26* (7), 1044-1051.

129. El-Kady, M. F.; Shao, Y.; Kaner, R. B., *Nat. Rev. Mater.* **2016,** *1*, 16033.

130. Toupin, M.; Brousse, T.; Bélanger, D., *Chem. Mater.* **2004,** *16* (16), 3184-3190.

131. Li, Q.; Wang, Z.-L.; Li, G.-R.; Guo, R.; Ding, L.-X.; Tong, Y.-X., *Nano Lett.* **2012,** *12* (7), 3803-3807.

132. Jia, H. N.; Lin, J. H.; Liu, Y. L.; Chen, S. L.; Cai, Y. F.; Qi, J. L.; Feng, J. C.; Fei, W.-D., *J. Mater. Chem. A* **2017,** *5* (21), 10678-10686.

133. Zheng, S.; Wu, Z.-S.; Wang, S.; Xiao, H.; Zhou, F.; Sun, C.; Bao, X.; Cheng, H.-M., *Energy Storage Mater.* **2017,** *6*, 70-97.

134. Bo, Z.; Zhu, W.; Ma, W.; Wen, Z.; Shuai, X.; Chen, J.; Yan, J.; Wang, Z.; Cen, K.; Feng, X., *Adv. Mater.* **2013,** *25* (40), 5799-5806.

135. Gao, L.; Song, J.; Surjadi, J. U.; Cao, K.; Han, Y.; Sun, D.; Tao, X.; Lu, Y., *ACS Appl. Mater. Interfaces* **2018,** *10* (34), 28597-28607.

136. Chen, C.; Zhang, Y.; Li, Y.; Dai, J.; Song, J.; Yao, Y.; Gong, Y.; Kierzewski, I.; Xie, J.; Hu, L., *Energy Environ. Sci.* **2017,** *10* (2), 538-545.

137. Huang, J.; Wei, J.; Xiao, Y.; Xu, Y.; Xiao, Y.; Wang, Y.; Tan, L.; Yuan, K.; Chen, Y., *ACS Nano* **2018,** *12* (3), 3030-3041.

138. Li, Y.; Xu, J.; Feng, T.; Yao, Q.; Xie, J.; Xia, H., *Adv. Funct. Mater.* **2017,** *27* (14), 1606728.

139. Tang, Z.; Zhang, G.; Zhang, H.; Wang, L.; Shi, H.; Wei, D.; Duan, H., *Energy Storage Mater.* **2018,** *10*, 75-84.

140. Chen, G. F.; Li, X. X.; Zhang, L. Y.; Li, N.; Ma, T. Y.; Liu, Z. Q., *Adv. Mater.* **2016,** *28* (35), 7680-7687.

141. Liu, Y.; Fu, N.; Zhang, G.; Xu, M.; Lu, W.; Zhou, L.; Huang, H., *Adv. Funct. Mater.* **2017,** *27* (8), 1605307.

142. Mohajernia, S.; Hejazi, S.; Mazare, A.; Nguyen, N. T.; Hwang, I.; Kment, S.; Zoppellaro, G.; Tomanec, O.; Zboril, R.; Schmuki, P., *Mater. Today Energy* **2017,** *6*, 46-52.

143. Li, C.; Wang, Z.; Li, S.; Cheng, J.; Zhang, Y.; Zhou, J.; Yang, D.; Tong, D.-G.; Wang, B., *ACS Appl. Mater. Interfaces* **2018,** *10* (21), 18390-18399.

144. Xu, C.; Li, Z.; Yang, C.; Zou, P.; Xie, B.; Lin, Z.; Zhang, Z.; Li, B.; Kang, F.; Wong, C. P., *Adv. Mater.* **2016,** *28* (21), 4105-4110.

145. Dinh, T. M.; Achour, A.; Vizireanu, S.; Dinescu, G.; Nistor, L.; Armstrong, K.; Guay, D.; Pech, D., *Nano Energy* **2014,** *10*, 288-294.

146. Liao, Q.; Li, N.; Jin, S.; Yang, G.; Wang, C., *ACS Nano* **2015,** *9* (5), 5310-5317.

147. Kim, G.; Ryu, I.; Yim, S., *Sci. Rep.* **2017,** *7* (1), 8260.

148. Gao, Y.; Lin, Y.; Chen, J.; Lin, Q.; Wu, Y.; Su, W.; Wang, W.; Fan, Z., *Nanoscale* **2016,** *8* (27), 13280-13287.

149. Xia, X.; Chao, D.; Fan, Z.; Guan, C.; Cao, X.; Zhang, H.; Fan, H. J., *Nano Lett.* **2014,** *14* (3), 1651-1658.

150. Liu, J.; Zhang, L.; Wu, H. B.; Lin, J.; Shen, Z.; Lou, X. W. D., *Energy Environ. Sci.* **2014,** *7* (11), 3709-3719.

151. Lv, Q.; Chi, K.; Zhang, Y.; Xiao, F.; Xiao, J.; Wang, S.; Loh, K. P., *J. Mater. Chem. A* **2017,** *5* (6), 2759-2767.

152. Wu, Z.-S.; Sun, Y.; Tan, Y.-Z.; Yang, S.; Feng, X.; Müllen, K., *J. Am. Chem. Soc.* **2012,** *134* (48), 19532-19535.

153. Yang, H.; Qiu, H.; Wang, J.-Q.; Huo, J.; Wang, X.; Li, R.-W.; Wang, J., *J. Alloys Compd.* **2017,** *703*, 461-465.

154. Liu, P.; Qin, K.; Wen, S.; Wang, L.; He, F.; Liu, E.; He, C.; Shi, C.; Li, J.; Li, Q., *Electrochim. Acta* **2018,** *283* (1), 970-978.

155. Wan, C.; Jiao, Y.; Li, J., *J. Mater. Chem. A* **2017,** *5* (33), 17267-17278.

156. Miao, P.; He, J.; Sang, Z.; Zhang, F.; Guo, J.; Su, D.; Yan, X.; Li, X.; Ji, H., *J. Alloys Compd.* **2018,** *732*, 613-623.

157. El-Kady, M. F.; Ihns, M.; Li, M.; Hwang, J. Y.; Mousavi, M. F.; Chaney, L.; Lech, A. T.; Kaner, R. B., *Proc. Natl. Acad. Sci. U.S.A.* **2015,** *112* (14), 4233-4238.

158. Liu, T.; Zhou, Z.; Guo, Y.; Guo, D.; Liu, G., *Nat. Commun.* **2019,** *10* (1), 675.

159. Xu, Y.; Zhou, M.; Wen, L.; Wang, C.; Zhao, H.; Mi, Y.; Liang, L.; Fu, Q.; Wu, M.; Lei, Y., *Chem. Mater.* **2015,** *27* (12), 4274-4280.

160. Xu, Y.; Zhou, M.; Zhang, C.; Wang, C.; Liang, L.; Fang, Y.; Wu, M.; Cheng, L.; Le, Y., *Nano Energy* **2017,** *38*, 304-312.

161. Holm, R., *Electric contacts: theory and application*. Springer Berlin, Germany, 2000.

162. Kötz, R.; Hahn, M.; Gallay, R., *J. Power Sources* **2006,** *154* (2), 550-555.

163. Buller, S.; Thele, M.; De Doncker, R. W.; Karden, E., *IEEE Trans. Ind. Appl.* **2005,** *41*, 742.

164. Buller, S.; Karden, E.; Kok, D.; De Doncker, R., *IEEE Trans. Ind. Appl.* **2002,** *38*, 1622.

165. Kötz, R.; Carlen, M., *Electrochim. Acta* **2000,** *45* (15), 2483-2498.

166. Kajdos, A.; Kvit, A.; Jones, F.; Jagiello, J.; Yushin, G., *J. Am. Chem. Soc.* **2010,** *132* (10), 3252-3253.

167. Lin, J.; Zhang, C.; Yan, Z.; Zhu, Y.; Peng, Z.; Hauge, R. H.; Natelson, D.; Tour, J. M., *Nano Lett.* **2012,** *13* (1), 72-78.

168. Shao, R.; Niu, J.; Liang, J.; Liu, M.; Zhang, Z.; Dou, M.; Huang, Y.; Wang, F., *ACS Appl. Mater. Interfaces* **2017,** *9* (49), 42797–42805.

169. Zhou, Q.; Zhang, M.; Chen, J.; Hong, J.-D.; Shi, G., *ACS Appl. Mater. Interfaces* **2016,** *8* (32), 20741-20747.

170. Banerjee, P.; Perez, I.; Henn-Lecordier, L.; Lee, S. B.; Rubloff, G. W., *Nat. Nanotechnol.* **2009,** *4* (5), 292-296.

171. Han, F.; Meng, G.; Zhou, F.; Song, L.; Li, X.; Hu, X.; Zhu, X.; Wu, B.; Wei, B., *Sci. Adv.* **2015,** *1* (9), e1500605.

172. Liu, C.; Gillette, E. I.; Chen, X.; Pearse, A. J.; Kozen, A. C.; Schroeder, M. A.; Gregorczyk, K. E.; Lee, S. B.; Rubloff, G. W., *Nat. Nanotechnol.* **2014,** *9* (12), 1031-1039.

173. Xue, Y.; Ding, Y.; Niu, J.; Xia, Z.; Roy, A.; Chen, H.; Qu, J.; Wang, Z. L.; Dai, L., *Sci. Adv.* **2015,** *1* (8), e1400198.

174. Liu, L.; Zhao, H.; Lei, Y., *Small Methods* **2019,** *3*, 1800341.

175. Thompson, G.; Wood, G., *Nature* **1981,** *290* (5803), 230.

176. Eftekhari, A., *J. Mater. Chem. A* **2018,** *6*, 2866-2876.

177. Huang, P.; Lethien, C.; Pinaud, S.; Brousse, K.; Laloo, R.; Turq, V.; Respaud, M.; Demortiere, A.; Daffos, B.; Taberna, P.-L., *Science* **2016,** *351* (6274), 691-695.

178. Pech, D.; Brunet, M.; Durou, H.; Huang, P.; Mochalin, V.; Gogotsi, Y.; Taberna, P.-L.; Simon, P., *Nat. Nanotechnol.* **2010,** *5* (9), 651-654.

179. El-Kady, M. F.; Kaner, R. B., *Nat. Commun.* **2013,** *4*, 1475.

180. Gao, W.; Singh, N.; Song, L.; Liu, Z.; Reddy, A. L. M.; Ci, L.; Vajtai, R.; Zhang, Q.; Wei, B.; Ajayan, P. M., *Nat. Nanotechnol.* **2011,** *6* (8), 496–500.

181. Niu, Z.; Zhang, L.; Liu, L.; Zhu, B.; Dong, H.; Chen, X., *Adv. Mater.* **2013,** *25* (29), 4035-4042.

182. Xiao, H.; Wu, Z.-S.; Chen, L.; Zhou, F.; Zheng, S.; Ren, W.; Cheng, H.-M.; Bao, X., *ACS Nano* **2017,** *11* (7), 7284-7292.

183. Wu, Z.-S.; Tan, Y.-Z.; Zheng, S.; Wang, S.; Parvez, K.; Qin, J.; Shi, X.; Sun, C.; Bao, X.; Feng, X., *J. Am. Chem. Soc.* **2017,** *139* (12), 4506-4512.

184. Wu, Z. S.; Parvez, K.; Feng, X.; Müllen, K., *Nat. Commun.* **2013,** *4*, 2487.

185. Shen, K.; Ding, J.; Yang, S., *Adv. Energy Mater.* **2018,** *8*, 1800408.

186. Pu, X.; Liu, M.; Li, L.; Han, S.; Li, X.; Jiang, C.; Du, C.; Luo, J.; Hu, W.; Wang, Z. L., *Adv. Energy Mater.* **2016,** *6* (24), 1601254.

187. Pikul, J. H.; Zhang, H. G.; Cho, J.; Braun, P. V.; King, W. P., *Nat. Commun.* **2013,** *4*, 1732.

188. Ning, H.; Pikul, J. H.; Zhang, R.; Li, X.; Xu, S.; Wang, J.; Rogers, J. A.; King, W. P.; Braun, P. V., *Proc. Natl. Acad. Sci. U.S.A.* **2015,** *112* (21), 6573-6578.

189. Zeng, Z.; Xu, R.; Zhao, H.; Zhang, H.; Xu, S.; Lei, Y., *Mater. Today Nano* **2018,** *3*, 54-68.

190. Lei, Z.; Liu, L.; Zhao, H.; Liang, F.; Chang, S.; Li, L.; Zhang, Y.; Lin, Z.; Kröger, J.; Lei, Y., *Nat. Commun.* **2020,** *11*, 299.

191. Liu, L.; Zhao, H.; Lei, Y., *InfoMat* **2019,** *1* (1), 74-84.

192. Chen, G.; Soper, S. A.; McCarley, R. L., *Langmuir* **2007,** *23* (23), 11777-11781.

193. Liang, Y.; Zhen, C.; Zou, D.; Xu, D., *J. Am. Chem. Soc.* **2004,** *126* (50), 16338-16339.

194. Togonal, A.; He, L.; Roca i Cabarrocas, P., *Langmuir* **2014,** *30* (34), 10290-10298.

195. Hill, J. J.; Haller, K.; Gelfand, B.; Ziegler, K. J., *ACS Appl. Mater. Interfaces* **2010,** *2* (7), 1992-1998.

196. Liang, L.; Xu, Y.; Wen, L.; Li, Y.; Zhou, M.; Wang, C.; Zhao, H.; Kaiser, U.; Lei, Y., *Nano Res.* **2017,** *10* (9), 3189-3201.

197. Tanaka, T.; Morigami, M.; Atoda, N., *Jpn. J. Appl. Phys.* **1993,** *32* (12S), 6059.

198. Fu, X.; Wang, Y.; Tuba, J.; Scudiero, L.; Zhong, W.-H., *Small Methods* **2018,** *2* (8), 1800066.

199. Liu, L.; Li, D.; Zhao, H.; Dimitrova, A.; Li, L.; Fang, Y.; Krischok, S.; Shi, W.; Lei, Y., *Appl. Catal., B* **2019,** *244* (5), 87-95.

200. Liu, L.; Yang, X.; Lv, C.; Zhu, A.; Zhu, X.; Guo, S.; Chen, C.; Yang, D., *ACS Appl. Mater. Interfaces* **2016,** *8* (11), 7047-7053.

201. Chen, Z.; Ye, S.; Evans, S. D.; Ge, Y.; Zhu, Z.; Tu, Y.; Yang, X., *Small* **2018,** *14* (19), 1704015.

202. Yan, L.; Li, D.; Yan, T.; Chen, G.; Shi, L.; An, Z.; Zhang, D., *ACS Appl. Mater. Interfaces* **2018,** *10* (49), 42494-42502.

203. Wang, Y.; Fu, X.; Zheng, M.; Zhong, W. H.; Cao, G., *Adv. Mater.* **2019,** *31* (6), 1804204.

204. Godino, N.; Borrise, X.; Munoz, F. X.; Del Campo, F. J.; Compton, R. G., *J. Phys. Chem. C* **2009,** *113* (25), 11119-11125.

205. Zhang, J.; Zhao, H.; Li, J.; Jin, H.; Yu, X.; Lei, Y.; Wang, S., *Adv. Energy Mater.* **2019,** *9* (4), 1803221.

206. Liu, L.; Yang, X.; Ma, N.; Liu, H.; Xia, Y.; Chen, C.; Yang, D.; Yao, X., *Small* **2015,** *12* (10), 1295–1301.

207. Zhang, P.; Li, Y.; Wang, G.; Wang, F.; Yang, S.; Zhu, F.; Zhuang, X.; Schmidt, O. G.; Feng, X., *Adv. Mater.* **2018,** *31* (3), 1806005.

208. Gao, J.; Shao, C.; Shao, S.; Bai, C.; Khalil, U. R.; Zhao, Y.; Jiang, L.; Qu, L., *ACS Nano* **2019,** *13* (7), 7463-7470.

209. Zheng, S.; Zhang, C. J.; Zhou, F.; Dong, Y.; Shi, X.; Nicolosi, V.; Wu, Z.-S.; Bao, X., *J. Mater. Chem. A* **2019,** *7* (16), 9478-9485.

210. He, Y.; Zhang, P.; Wang, M.; Wang, F.; Tan, D.; Li, Y.; Zhuang, X.; Zhang, F.; Feng, X., *Mater. Horiz.* **2019,** *6*, 1041-1049.

211. Robert, K.; Douard, C.; Demortière, A.; Blanchard, F.; Roussel, P.; Brousse, T.; Lethien, C., *Adv. Mater. Technol.* **2018,** *3* (7), 1800036.

212. Zhang, C.; Kremer, M. P.; Seral-Ascaso, A.; Park, S. H.; McEvoy, N.; Anasori, B.; Gogotsi, Y.; Nicolosi, V., *Adv. Funct. Mater.* **2018,** *28* (9), 1705506.

213. Zhang, C. J.; McKeon, L.; Kremer, M. P.; Park, S.-H.; Ronan, O.; Seral-Ascaso, A.; Barwich, S.; Coileáin, C. Ó.; McEvoy, N.; Nerl, H. C., *Nat. Commun.* **2019,** *10* (1), 1795.

Extended works

During the period of my Ph.D., besides the works presented in this dissertation, I also make my way into other fields of energy storage conversion and storage as well as environmental conservation. I have published four more papers as the first author. The abstracts and the table of content of the respective papers are illustrated in this section to highlight the achieved results beyond the scope of this dissertation.

1. A transparent CdS@TiO_2 nanotextile photoanode with boosted photoelectrocatalytic efficiency and stability (*Liu et. al., Nanoscale*, **2017**, *9*, 15650)

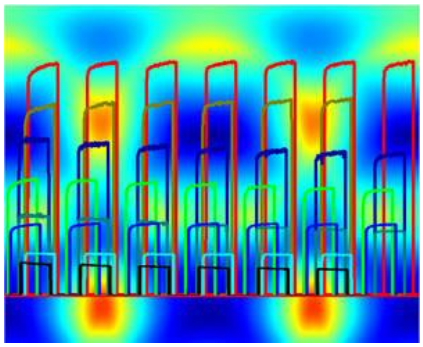

In the present work, we report the exploration of transparent CdS@TiO_2 nanotextile photoanode with boosted photoelectrocatalytic (PEC) efficiency and stability, by controllable coating of amorphous TiO_2 ultrathin layer via atomic layer deposition technique. The optimal CdS@TiO_2 nanotextile photoanode with 3.5 nm TiO_2 ultrathin layer exhibit a photocurrent density of 1.8 mA/cm^2 at 0 V *vs.* RHE, which is 11 times higher than that of pristine CdS counterpart. The photocatalytic H_2 evolution rate of CdS@TiO_2 is up to 47.5 mmol/g/h, which is superior to those of ever reported works based on one-dimensional CdS-based counterparts. Moreover, the photocurrent of CdS@TiO_2 nanotextile photoanodes shows only 9% decaying after 9 h, suggesting its profoundly enhanced PEC stability, in comparison to that of pristine CdS photoanodes (almost down to zero after 3 hours). It is verified that the introduced TiO_2 nanoshells could limit the charge recombination, facilitate the charge separation, reduce the charge transfer resistance, and enhance the wettability of electrode, resulting in their significantly enhanced PEC performance.

2. Micro-nanostructured δ-Bi_2O_3 with surface oxygen vacancies as superior adsorbents for SeO_x^{2-} ions (*Liu et. al., J. Hazard. Mater.*, **2018**, *360*, 279-287)

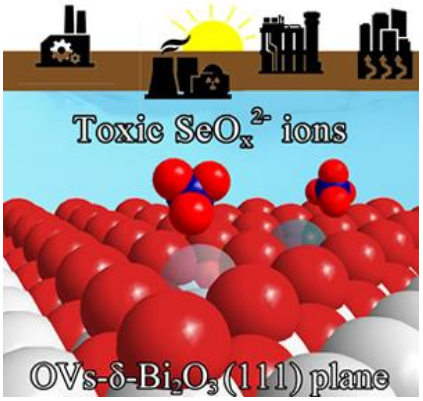

Removal of the toxic selenium compounds, selenite (SeO_3^{2-}) and selenate (SeO_4^{2-}), from contaminated water is imperative for environmental protection in both developing and industrialized countries. Providing high selectivity adsorbents to the target ions is a big challenge. Here we report that micro sphere-like δ-Bi_2O_3 (MS-δ-Bi_2O_3) with surface oxygen vacancy defects can capture hypertoxic SeO_x^{2-} anions from aqueous solutions with superior capacity and fast uptake rate. High capture selectivity to SeO_3^{2-} anions is observed, since the O atoms of SeO_3^{2-} anions fill the oxygen vacancies on the (111) facet of δ-Bi_2O_3 forming a stable complex structure. This mechanism is distinctly different from other known mechanisms for anion removal, and implies that we may utilize surface defects as highly efficient and selective sites to capture specific toxic species. Thus, we present a new route here to design superior adsorbents for toxic ions.

3. Optimizing hydrogen Evolution Activity of Nanoporous Electrodes by Dual-Step Surface Engineering (*Liu et. al., Appl. Catal., B*, **2019**, *244*, 87-95)

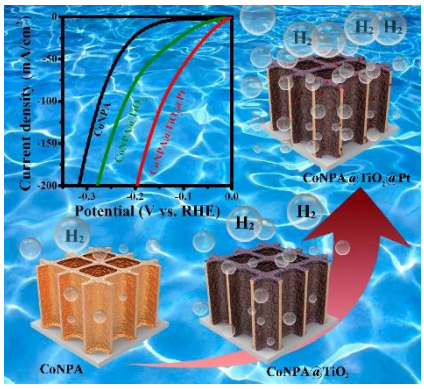

The hydrogen evolution reaction (HER) from electrocatalytic water splitting represents an important approach for efficient hydrogen production, in which the HER feasibility relies on electrocatalysts as well as the art of electrode design. Herein, a considerate surface engineering strategy is developed for promoting HER process taking place on nanoporous HER electrodes. Cobalt nanopore arrays (CoNPA) are fabricated as the representative nanoporous HER electrode. Then an ultrathin titanium dioxide (TiO_2) with optimized thickness is conformally coated onto CoNPA for improving the wettability in order to expose more active sites, followed by a well-dispersed platinum (Pt) nanoparticles with an ultralow mass loading

(ca. 54 μg cm^{-2}) anchored on TiO_2 layer for enhancing the HER activity. The advanced features of nanoporous architecture in combination with the synergistic contribution from ultrathin TiO_2 layer and well-dispersed Pt nanoparticles enable CoNPA@TiO_2@Pt electrode exhibit outstanding HER performance in alkaline conditions, *i.e.*, only 29 mV overpotential needed to exert the catalytic current density of 10 mA cm^{-2} and long-termed performance as well as structure stability. Not limited to the HER electrodes, the similar strategy is also expected to be further applied to the rational design and nanoengineering of electrodes for other electrochemical energy conversion and storage devices.

4. Advances on Three-Dimensional Electrodes for Micro-Supercapacitors: A Mini-Review (*Liu et. al., InfoMat*, **2019**, *1*, 74-84**)**

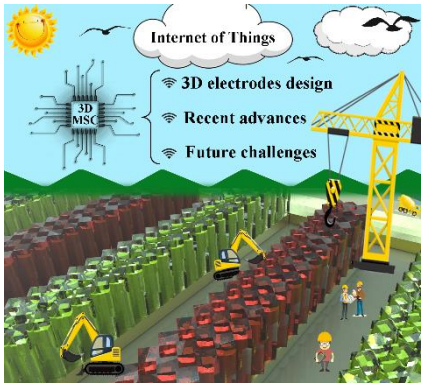

Owing to the high power density, long cycle life and maintain-free, micro-supercapacitors (MSCs) stand out as preferred miniaturized energy source for the miscellaneous autonomous electronic components. However, the shortage of energy density is the main stumbling block for their practical applications. To solve this energy issue, constructing a three-dimensional (3D) electrode within the limited footprint area is proposed as a new solution for improving the energy storage capacity of MSCs. In the last few years, extensive efforts have been devoted to developing 3D electrodes for MSCs, and significant progress and breakthrough have been achieved. While, there is still lack of systematic summary on the 3D electrode design strategies. To this end, it is imperative to outline the basic design conception, summarize the current states and discuss the future research about 3D electrodes in MSCs based on the latest development.

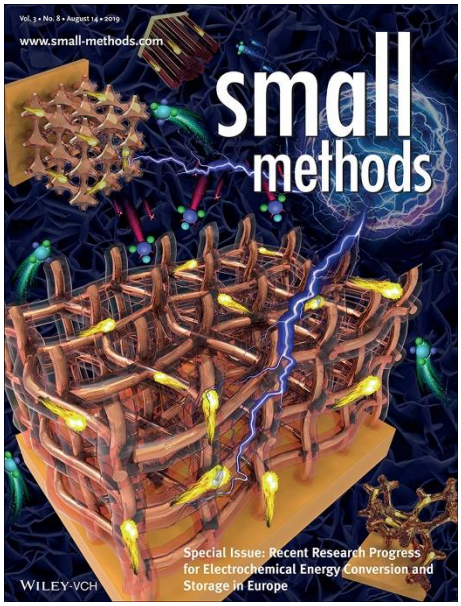

Cover story

The paper 'Review on Nanoarchitectured Current Collectors for Pseudocapacitors' by L. Liu , H. Zhao and Y. Lei was selected as front cover in Small Methods in the Volume 3, Issue 8. (Designed and drawn by L. Liu)

Scientific contributions

In total, I have published and jointly published 16 papers in SCI-indexed international scientific journals during the period of my Ph.D., among them, 7 papers are first-authored ones including 3 papers with impact factor higher than 10 (*Nature Communications*, *Advanced Functional Materials*, *Applied Catalysis B: Environmental*). Three more first-authored papers are under preparation for publishing in SCI-indexed international scientific journals. Besides, I have given 16 contributions to conferences, including 9 talks, and 7 posters.

Publications in SCI-indexed scientific journals

1. Lei Z.D.[†], **Liu L.**[†], ([†]Contributed equally) Zhao H.P.[*], Feng L.[*], Chang S.L., Li L., Zhang Y., Lin Z., Kröger J., Lei Y.[*], 'Nanoelectrode design from microminiaturized honeycomb monolith with ultrathin and stiff nanoscaffold for high-energy micro-supercapacitors', ***Nature Communications***, 2020, 11, 299 (IF 11.878).

(This work has recently been highlighted at *MDR.DE*, *PRESSEBOX*, *smarterworld.de*, *and DESIGN&ELEKTRONIK*)

https://www.mdr.de/wissen/faszination-technik/vorbild-bienenwabe-ilmenauer-wissenschaftler-bauen-super-energiespeicher-fuer-chips-100.html

https://www.pressebox.de/pressemitteilung/technische-universitaet-ilmenau/Nature-Communications-berichtet-ueber-Forschung-der-TU-Ilmenau-zu-Mikro-Superkondensatoren/boxid/989696

https://www.smarterworld.de/smart-power/sonstige/artikel/172938/

https://www.elektroniknet.de/design-elektronik/power/miniaturisierte-super-energiespeicher-172971.html?xing_share=news

2. **Liu L.**, Li D., Zhao H.P.[*], Dimitrova A., Li L.H., Fang Y.G., Krischoka S., Shi W.D.[*], Lei Y.[*], 'Optimizing hydrogen evolution activity of nanoporous electrodes by dual-step surface engineering', ***Applied Catalysis B: Environmental***, 2019, 244, 87-95 (IF 14.229).

3. **Liu L.**, Zhao H.P.*, Wang Y., Fang Y.G., Xie J.L., Lei Y.*, 'Evaluating the role of nanostructured current collectors in energy storage capability of supercapacitor electrodes with thick electroactive materials layer', ***Advanced Functional Materials***, 2018, 28, 1705107 (IF 15.621).

4. **Liu L.**, Zhao H.P.*, Lei Y.*, 'Review on nanoarchitectured current collectors for pseudocapacitors', ***Small Methods***, 2018, 2, 1800341. (**Front cover paper**)

5. **Liu L.**, Chen N., Lei Y., Xue X.Y., Li L., Wang J.C., Komarneni S., Zhu H.Y.*, Yang D.J.*, 'Micro-nanostructured δ-Bi_2O_3 with surface oxygen vacancies as superior adsorbents for SeO_x^{2-} ions', ***Journal of Hazardous Materials***, 2018, 360, 279-287 (IF 7.650).

6. **Liu L.**, Hou H.L., Wang L., Xu R., Lei Y., Shen S.H., Yang D.J.*, Yang W.Y.*, 'Transparent CdS@TiO_2 nanotextile photoanode with boosted photoelectrocatalytic efficiency and stability', ***Nanoscale***, 2017, 9, 15650-15657 (IF 6.970).

7. **Liu L.**, Zhao H.P., Lei Y.*, 'Advances on Three-Dimensional Electrodes for Micro-Supercapacitors: A Mini-Review', ***InfoMat***, 2019, 1, 74-84.

(This work has recently been highlighted at MaterialsViewsChina; The paper is within download top 10 in 2019)

http://www.materialsviewschina.com/2019/05/36535/

https://www.materialsviewschina.com/2020/01/42292/

8. Zhao H.P., **Liu L.**, Vellacheri R., Lei Y.*, 'Recent advances in designing and fabricating self-supported nanoelectrodes for supercapacitors', ***Advanced Science***, 2017, 4, 1700188 (IF 15.804).

9. Zhao H.P., **Liu L.**, Fang Y.G., Vellacheri R., Lei Y.*, 'Nickel nanopore arrays as promising current collectors for constructing solid-state supercapacitors with ultrahigh rate performance', ***Frontiers of Chemical Science and Engineering***, 2018, 12, 481–493 (IF 2.809).

10. Zhao H.P., **Liu L.**, Lei Y.*, 'A mini review: Functional nanostructuring based on perfectly-ordered PAM template for energy conversion and storage', ***Frontiers of Chemical Science and Engineering***, 2018, 12, 339–345 (IF 2.809).

11. Sha M., **Liu L.**, Zhao, H.P., Lei Y.*, 'Review on recent advances of cathode materials for potassium-ion batteries', ***Energy & Environmental Materials***, 2020, 3, 56-66.

12. Sha M., **Liu L.**, Zhao H.P., Zeng Z.Q., Lei Y.*, 'Review on recent development of anode materials for potassium-ion batteries', ***Carbon Energy***, 2020 (accepted and in press).

13. Dong H.S., Xu Y*, Zhang C.L., Wu Y.H., Zhou M., **Liu L.**, Li W., Dong Y.L., Fu Q., Wu M.H., Lei Y.*, 'MoS_2 nanosheets with expanded interlayer spacing for enhanced sodium storage', ***Inorganic Chemistry Frontiers***, 2018, 5, 3099-3105 (IF 5.934).

14. Zeng Z.Q., Xu R., Zhao H.P., Zhang H.M., **Liu L.**, Xu S.P., Lei Y.*, 'Exploration of nanowire- and nanotube-based electrocatalysts for oxygen reduction and oxygen evolution reaction', ***Materials Today Nano***, 2018, 3, 54-68.

15. Bahmani F., Kazemi S. H.*, Wu Y., **Liu L.**, Xu Y.*, Lei Y.*, '$CuMnO_2$-reduced graphene oxide nanocomposite as a free-standing electrode for high-performance supercapacitors', ***Chemical Engineering Journal***, 2019, 375, 121966 (IF 8.355).

16. Yan C., Zhao H., Li J., Jin H., **Liu L.**, Wu W., Lei Y.*, Wang S.* 'Mild-temperature solution-assisted encapsulation of phosphorus into ZIF-8 derived porous carbon as lithium-ion battery anode', ***Small***, 2020, 16, 1907141 (IF 10.856).

Manuscript under preparation

1. **Liu L.**, Zhao H.P.*, Yan C., Lei Y.*, 'Building non-aggregative and robust one-dimensional nanoelectrode arrays for micro-supercapacitors: Beyond aspect ratio restriction' (To be submitted).

2. **Liu L.**, Zhao H.P.*, Lei Y.*, 'An ultrafast charge/discharge micro-supercapacitors based on nanoporous alumina membranes' (To be submitted).

3. He K.M.[†], **Liu L.**[†], ([†]Contributed equally) Zhao H.P., Fu Q., Wu M.H.[*], Lei Y.[*], 'Toward an insight into the effect of post-annealing on core-shell Sb_2S_3@C as potassium-ion battery anode' (To be submitted).

Conference contributions

1. **Liu L.**, Zhao H.P., Xu R., Zhang H.M., Wang Y., Yang D.J., Lei Y., 'Iron-based nitrogen doped graphene aerogels derived from seaweed waste as electrocatalysts for efficient electrochemical energy conversion and storage', the Annual Conference of the Deutsche Physikalische Gesellschaft (DPG), Mar. 19-24, 2017, Dresden, Germany. **(Talk)**

2. **Liu L.**, Zhao H.P., Lei Y., 'Reevaluating the role of nanostructured current collectors in supercapacitors: beyond ultrathin conformal coating', the 29th GCCCD® Annual Conference, Oct. 13-15, 2017, Hamburg, Germany. **(Poster)**

3. Zhao H.P., **Liu L.**, Fang Y.G., Lei Y., 'Nanoporous alumina membranes as promising platforms for rationally designing supercapacitor electrodes', the Annual Conference of the DPG, Mar. 11-16, 2018, Berlin, Germany. **(Talk)**

4. Zhao H.P., Xu R., Mi Y., **Liu L.**, Fang Y.G., Lei Y., 'Template-based nanoengineering strategies for photoelectrodes design toward enhancing photoelectrochemical water splitting' the Annual Conference of the DPG, Mar. 11-16, 2018, Berlin, Germany. **(Talk)**

5. Zhao H.P., Xu Y., Mi Y., Xu R., **Liu L.**, Fang Y.G., Zhou M., Lei Y., 'Functional nanostructuring with nanoporous alumina membranes as templates for advanced energy conversion and storage' the Annual Conference of the DPG, Mar. 11-16, 2018, Berlin, Germany. **(Poster)**

6. **Liu L.**, Zhao H.P., Xu Y., Xu S.P., Zhang C.L., Zeng Z.Q., Lei Y., 'Evaluate the Role of Nanostructure Current Collector in Supercapacitor Electrode when the Elctroactive Material is in the Form of Thick Layer', the Annual Conference of the DPG, Mar. 11-16, 2018, Berlin, Germany. **(Talk)**

7. **Liu L.**, Zhao H.P., Xu R., Xu S.P., Zhang C.L., Lei Y., 'Transparent CdS@TiO_2 Nanotextile Photoanode with Boosted Photoelectrocatalytic Efficiency and Stability', the Annual Conference of the DPG, Mar. 11-16, 2018, Berlin, Germany. **(Poster)**

8. Xu S.P., Zhao H.P., Xu Y., Xu R., Zhang H.M., **Liu L.**, Lei Y., 'Template-Assisted Fabrications of Regular Arrays of Nanostructures for Sensitive Gas-Sensing', the Annual Conference of the DPG, Mar. 11-16, 2018, Berlin, Germany. **(Talk)**

9. Xu S.P., Zhao H.P., Xu Y., Xu R., Zhang H.M., **Liu L.**, Lei Y., 'Template-Assisted Fabrications of Nanostructure-Array-Based Gas-Sensors', the Annual Conference of the DPG, Mar. 11-16, 2018, Berlin, Germany. **(Poster)**

10. Zhang C.L., Xu Y., Zhou M., **Liu L.**, Lei Y., 'Low-cost $K_{0.220}Fe[Fe(CN)_6]_{0.805}$ as Cathode Material for Potassium-ion Batteries' the Annual Conference of the DPG, Mar. 11-16, 2018, Berlin, Germany. **(Talk)**

11. Zhang C.L., Xu Y., **Liu L.**, Lei Y., 'A low cost potassium Prussian blue cathode for potassium ion batteries' the Annual Conference of the DPG, 31 Mar.-5 Apr., 2019, Regensburg, Germany. **(Poster)**

12. Zhang C.L., Xu Y., **Liu L.**, Lei Y., 'Highly nitrogen doped carbon nanofibers with superior rate capability and cyclability for potassium ion batteries' the Annual Conference of the DPG, 31 Mar.-5 Apr., 2019, Regensburg, Germany. **(Talk)**

13. Zhao H.P., **Liu L.**, Fang Y.G., Lei Y., 'Template-Realized Functional Nanostructure Arrays for Electrical Energy Conversion and Storage' the Annual Conference of the DPG, 31 Mar.-5 Apr., 2019, Regensburg, Germany. **(Poster)**

14. **Liu L.**, Zhao H.P., Xu Y., Zhang C.L., Fang Y.G., Lei Y., 'Rational surface engineering toward optimizing hydrogen evolution activity of nanoporous electrodes' the Annual Conference of the DPG, 31 Mar.-5 Apr., 2019, Regensburg, Germany. **(Talk)**

15. **Liu L.**, Zhao H.P., Zhang C.L., Xu Y., Yang D.J., Lei Y., 'Mechanism of SeO_x^{2-} immobilization by δ-Bi_2O_3 microsphere with surface oxygen vacancies' the Annual Conference of the DPG, 31 Mar.-5 Apr., 2019, Regensburg, Germany. **(Poster)**

16. **Liu L.**, Lei Y., 'Surface engineering strategy of nanoporous electrode for efficient alkaline hydrogen evolution performance' Gemeinsames Kolloquium der Physik und der Chemie, 28 May, 2019, Ilmenau, Germany. **(Talk)**

Declaration

I hereby declare that this Ph.D. dissertation entitled “Constructing Pseudocapacitive Electrodes for Supercapacitors based on Rationally Designed Nanoarchitectured Current Collectors” was carried out by me for the degree of Doctor of Philosophy under the supervision of Prof. Dr. Yong Lei. All dates or information in this dissertation that have been directly or indirectly consulted or used from other sources are clearly stated. This dissertation has not been submitted, in part or in whole, for any other degree or examination in any other University. I have acknowledged all main sources of help, and I have made clear exactly what was done by others and what I have contributed when the work was done jointly with others. Some of the results may have been published in scientific journals or elsewhere. I am aware that the falsity of this declaration will be regarded as an attempt of deception and will cause the derogation of the doctoral procedure.

Ilmenau, June 12th, 2020

Long Liu